Magnetron Sputtered Zn_2SiO_4 and Y_2O_3-SiO_2 Thin Film Phosphors for Cathodoluminescent and Electroluminescent Displays

By

XU OUYANG, B.Engin. M.Engin.

A Thesis

Submitted to the School of Graduate Studies

in Partial Fulfillment of the Requirements

for the Degree

Doctor of Philosophy

McMaster University

DOCTOR OF PHILOSOPHY (1995) McMASTER UNIVERSITY
(Materials Engineering) Hamilton, Ontario

TITLE: Magnetron Sputtered Zn_2SiO_4 and Y_2O_3-SiO_2 Thin Film Phosphors for Cathodoluminescent and Electroluminescent Displays

AUTHOR: Xu Ouyang, B.Engin., M.Engin. (Chengdu Institute of Radio Engineering)

SUPERVISOR: Dr. A.H. Kitai

NUMBER OF PAGES: xvi, 124

To my wife Yuxia Jing and my daughter Jing Ouyang

ABSTRACT

The cathodoluminescence of various thin films deposited on (111)Si substrates was systematically studied for the first time. The best dopants for red, green and blue (RGB) phosphor films are Eu, Tb and Ce, respectively. A program was developed for the calculation of chromaticity coordinates from the luminescent spectra. High luminescence can only be achieved by post-annealing thin films above 900°C for yttrium silicates or above 850°C for zinc silicates. The band-gaps of the thin films were measured by UV absorption spectroscopy.

Rare earth (Ce^{3+}, Pr^{3+}, Nd^{3+}, Sm^{3+}, Eu^{3+}, Gd^{3+}, Tb^{3+}, Er^{3+}) doped Y_2SiO_5, $Y_2Si_2O_7$, $Y_{4.67}(SiO_4)_3O$ and Mn^{2+} doped Zn_2SiO_4 thin films were prepared by magnetron sputtering. Their compositions were studied by Rutherford backscattering and X-ray diffraction. Sputtering parameters such as magnetic field, pressure, target-substrate distance and substrate temperature were studied. The chromaticity coordinates and brightness of thin film phosphors were compared with their powder counterparts. These films show potential for practical applications.

Electroluminescence was found only in $Zn_2SiO_4:Mn^{2+}$ and $Y_2SiO_5:Ce^{3+}$ thin film phosphors. The devices of ITO/$Zn_2SiO_4:Mn^{2+}$ (or $Y_2SiO_5:Ce^{3+}$)/$BaTiO_3$/Al and multi-insulated phosphor thin films were prepared and their electroluminescent (EL) response under different voltages, frequencies and pulse widths, and their decay curves and transferred charges were studied. With the same chromaticity coordinates as Sylvania powder CL

samples, $Zn_2SiO_4:Mn^{2+}$ (2% mole) thin films are shown to have very good EL performance with a brightness as high as 80 foot lambents (fL) excited by 400 Hz a.c. pulses, with a short decay time of 0.6 ms and with an efficiency of 0.78 lumin/watt.

ACKNOWLEDGMENTS

I would like to express my thanks to the following people:

Dr. A.H. Kitai, who supervised me in the Ph.D program and gave me guidance and held many helpful discussions about the preparation of my Ph.D. thesis.

Engineering and Senior Science Machine Shop staff who did a lot of machining for me and gave me access to the equipment. Without their help, the setting up of the sputtering system could not have been accomplished.

Mrs. C. Barry, who helped me hot-press $BaTiO_3$ substrates.

Mr. C. Butcher, who gave me access to the substrate cutter and polishing machine.

Mr. Wenhe Gong, who performed X-ray analysis for the thin film structures.

Dr. R. Siegele, who performed Rutherford backscattering measurements for the thin film composition analysis.

My supervisory committee, Dr. G. Weatherly and Dr. P. Nicholson, for their helpful suggestions.

The help of these people is gratefully acknowledged and appreciated.

TABLE OF CONTENTS

TABLE OF CONTENTS (continued)

TABLE OF CONTENTS (continued)

TABLE OF CONTENTS (continued)

LIST OF ILLUSTRATIONS

LIST OF ILLUSTRATIONS (continued)

LIST OF ILLUSTRATIONS (continued)

LIST OF ILLUSTRATIONS (continued)

LIST OF ILLUSTRATIONS (continued)

LIST OF TABLES

LIST OF TABLES (continued)

CHAPTER 1

INTRODUCTION

1.1 BACKGROUND

The display of information plays a very important part in everyday life. The future of the display is high definition (HD) TV and large scale flat panel displays, for which major candidates are liquid crystals (LC), cathodoluminescence (CL), electroluminescence (EL), gas plasma, vacuum fluorescence (VF) and light emitting diodes (LED). Each has advantages and disadvantages. The mechanisms of CL, EL, VF and plasma displays are based on the luminescence of phosphors.

Phosphors are solid materials that emit visible light (luminescence) when excited by the absorption of visible light (photoluminescence-PL), ultraviolet radiation, X- rays, and gamma rays, by collision with charged particles such as electrons in vacuum (cathodo-luminescence), by excitation with electrical field (electroluminescence-EL), by chemical reactions (chemoluminescence), and by any other means. Luminescent emission arises from atoms and molecules that have been energized in some manner without appreciably heating the bulk material, and that releases the excess energy in the form of light. Phosphors are used in the form of powders as well as thin films. Powder phosphors are used mainly in conventional CRTs, X-ray storage screens, mercury lamps, plasma displays and EL lamps while thin film phosphors are used mainly in EL and VF flat panel displays. The general require-

ments for phosphors are high photon emitting efficiency, high brightness, and pure red, green, blue (RGB) and white colors. Material stability in critical applications or harsh environments is also important. Different decay times are required for different applications. All present phosphors (sulfides, selenides, silicates, tungstates, and oxides of zinc, yttrium, cadmium, and magnesium) are wide-band-gap (E_g >3 eV) materials, making them transparent to internally generated light [Kazan, 1980].

Oxides are very attractive among the phosphors listed due to their optical transparency, chemical stability, stability under the impingement of high energy electron beams (>10 kV), and long luminescent life. However, most of the present work is limited to the powder form for CRT applications; very little has been reported on thin films.

Pseudo-binary compounds in the ZnO-SiO_2 and Y_2O_3-SiO_2 systems are the best candidates for preparing thin film phosphors for the following reasons:

(a) Most of the compounds within the system are commercial phosphors, e.g. ZnO, Zn_2SiO_4, Y_2O_3, Y_2SiO_5, $Y_2Si_2O_7$.

(b) Large quantities of rare earth (RE^{3+}) luminescent centers can be substituted into silicates for Y^{3+} without introducing a second phase or luminescent quenching.

(c) The thin film deposition temperature can be decreased by choosing a suitable Y_2O_3-SiO_2 ratio.

The important issues in the field of oxide EL devices are as follows:

- How does one prepare these oxide thin film phosphors?

- What is the best quantity of dopants for each of these phosphors?
- What are the best host lattice and best dopants for red (R), green (G), and blue (B) full-color displays?
- Which compounds in the system are suitable for electroluminescence?
- What is the mechanism of electroluminescence in oxide thin films? What are the electron processes in oxide EL devices?
- How does one make the best device structure for EL displays?

1.2 PREVIOUS WORK

1.2.1 $Zn_2SiO_4:Mn^{2+}$

The structure of willemite (Zn_2SiO_4) was first proposed in 1930 [Bragg, 1930] and was refined by Simonov (1977). It is similar to phenacite (Be_2SiO_4). Zn_2SiO_4 is a photoluminescent material as well as a green commercial CRT phosphor.

Most of the research on the luminescence of $Zn_2SiO_4:Mn^{2+}$ (JEDEC P-1 phosphor used for projection tubes) was done in the 1980's. In 1981, IBM reported the luminescence mechanism of the material was the thermal release of trapped electrons [Avouris, 1981]. The intensities of both CL and PL were found to be proportional to 1/(decay time)^n. Electron traps with excitation energy 0.2, 0.25, 0.3, 0.8 and 1.9 eV were observed in the host lattice of anti-flicker P39 (Zn_2SiO_4:Mn co-doped with As) samples. Three or more decay times in P39 were reported in the same year [Yang, 1981]. The shortest was 10-20 ms, believed due to the Mn^{2+} radiative transition rate.

High resolution, low temperature (4K), selectively excited photoluminescence spectra of Mn^{2+} doped Zn_2SiO_4 single crystals were used to reveal the two inequivalent $Mn_{Zn^{2+}}$ sites, Mn_A and Mn_B [Robbins, 1984]. This was the first time luminescence from the two inequivalent centers was clearly separated. Photons with wavelengths of 473 nm (or 458 nm) and 514 nm were used to excite Mn_A and Mn_B respectively. It was observed that high Mn^{2+} concentrations (>1 % mole) will render Mn_A and Mn_B characteristic peaks (514.5 nm and 501.7 nm respectively) less resolved.

The preparation of Zn_2SiO_4 thin films by Sol-Gel method was reported in 1989 [Khrupunkov, 1989]. Sol-Gel is suitable for mass production of thin films but its shortcoming is the difficulty in controlling the thickness of films.

The effective electroluminescent oxide was never reported until 1992 when the Japanese produced an EL device of ZnO:Al/Zn_2SiO_4:Mn/$BaTiO_3$/Al which has a brightness as high as 3400 cd/m2 [Minami, 1992].

1.2.2 Y_2O_3-SiO_2

The pseudo-binary Y_2O_3-SiO_2 system is a very complicated one. The structure of yttrium silicates was initially studied as minerals. The only mineral of yttrium silicate, Yttrialite, metamict yttrium silicate, $Y_2Si_2O_7$, was first found at Llano, Texas [Hidden, 1889]. The compound Y_2SiO_5, which has not been found in nature, was prepared by Toropov and Bondar [Toropov, 1961]. The polymorphic α, β, γ, δ structures of $Y_2Si_2O_7$ were reported in 1968 [ITO, 1968]. In the same year, garnet $Y_4Si_3O_{12}$ or $Y_{4.67}(SiO_4)_3O$ was synthesized

[Buisson, 1968]. Detailed X-ray diffraction data for all yttrium silicate compounds were reported in 1986 [Liddell, 1986].

Soon after the accomplishment of the synthesis of the above compounds, Philips Research Lab. [Gomes, 1969] reported the cathodoluminescence of Ce^{3+}-activated Y_2O_3 and $Y_2Si_2O_7$ as blue cathode ray tube (CRT) phosphors. The energy conversion efficiencies η, etc., of yttrium silicates were reported as 4-8%.

In 1985, the Royal Signal and Radar Establishment in UK studied the cathodo-luminescence of Tb^{3+}-doped Y_2SiO_5, $Y_2Si_2O_7$ and $ZnY_2Si_2O_7$ [Born, 1985]. As much as 15% of Tb^{3+} was doped into ZnY_2SiO_7 without inducing luminescent quenching. They hoped that zinc would be a good luminescent sensitizer and $ZnY_2Si_2O_7$ and $Zn_2Si_2O_8$ could be compounds but this assumption was never confirmed.

The application of Y_2SiO_5:Tb^{3+} thin films for miniature CRTs in helmet-mounted displays was reported by AT&T in 1989 [Shmulovish, 1989]. Y_2SiO_5 was prepared by Sol-Gel and dc-sputtering. The achieved efficiencies (internal conversion efficiency relative to that of a similar material in single crystal form) of thin films deposited by both methods were 50%.

Photo-stimulated luminescence (PSL) and thermally stimulated luminescence (TSL) of Y_2SiO_5:Ce^{3+} and Sm^{3+} were reported by the University of Utrecht, Netherlands [Meijerink, 1991]. Their PSL and TSL results showed that these compounds are X-ray storage phosphors with a short response and decay time (35±10 ns). In the Ce^{3+} and Sm^{3+} co-doped Y_2SiO_5, Sm^{3+} acts as an electron trap and becomes Sm^{2+}. Optical stimulation

results in Ce^{3+} emission and thermal stimulation in Sm^{3+} emission. Oxygen acts as electron traps in the compound without Sm^{3+}. The holes are trapped on Ce^{3+} giving Ce^{4+}.

In 1992, UV and gamma-ray excited luminescence of cerium-doped $Y_2Si_2O_7$ was studied for scintillator application [Suzuki, 1992]. Two luminescent centers, Ce1 and Ce2, were reported.

The electroluminescence of r.f. magnetron sputtered blue $Y_2SiO_5:Ce^{3+}$, $Zn_2SiO_4:Ti^{2+}$ and $Sr_2P_2O_7:Eu^{3+}$ thin films was reported in 1993 [Minami, 1993]. Thin films were post annealed to 1000-1035°C for 5 hours, giving luminescence of 8.5, 15.8 and 13.4 cd/m^2, respectively.

1.3 OUR CONTRIBUTIONS

We started work in 1990 to look for the best oxide, RGB-color, thin-film phosphors for CL and EL displays. The work undertaken addressed the following questions:

(1) What are the most effective powder RGB color phosphors? (The best host lattice, the best dopants and the best doping quantity). What are their luminescent properties?

(2) How can one translate these powder phosphors into thin films?

(3) Are the luminescent properties of these thin films the same as that of their powder counterparts?

(4) What substrate is suitable for EL devices? What is the best structure for oxide thin film phosphor EL devices? What is the mechanism of EL?

To solve question (1), RE^{3+} (Ce^{3+}, Pr^{3+}, Nd^{3+}, Sm^{3+}, Eu^{3+}, Gd^{3+}, Tb^{3+}, Er^{3+}) were doped into Y_2O_3, Y_2SiO_5, $Y_2Si_2O_7$, and Ti, Eu^{2+}, Mn^{2+} into Zn_2SiO_4. The CL results showed that Ce^{3+}(1-3% mole), Tb^{3+}(3-7% mole) and Eu^{3+}(3-7% mole) are the best dopants for blue, green and red, respectively. The change of host lattice from Y_2SiO_5 to $Y_2Si_2O_7$ gave no significant brightness increase. RE^{3+}-doped Y_2O_3 has a brightness more than twice that of yttrium silicates but is hard to prepare as crystallized thin films due to the high melting point of Y_2O_3.

Magnetron sputtering was used to deposit oxide thin films. The composition relationship between target and thin films was determined via X-ray diffraction and Rutherford backscattering. A powder target was used because it eliminates the target composition migration usually found in a multi-component ceramic target. Thin films with ratios of 1:1 and 1:2 were deposited using targets with Y_2O_3:SiO_2 ratios of 1:2 and 1:3.3. Garnet structure $Y_{4.67}(SiO_4)O$ thin film was prepared for the first time. The Zn_2SiO_4:Mn^{2+} target has the same composition as the thin films deposited as the atomic weights of Zn, Si, Mn are almost the same.

The cathodoluminescence brightness of the thin films was compared with their powder counterparts. It was observed that thin film phosphors with thickness of about 1 μm on a (111)Si substrate are usually 10-30% as bright as their powder form. Most of the light (~70%) was trapped within the film by the waveguiding effect.

CL spectra show that Tb^{3+} is less influenced by the host lattice whereas Eu^{3+} and Ce^{3+} are sensitive to the lattice environment. Color coordinates, dominant wavelength and excitation purity were calculated using the gathered spectra.

The bandgaps of Zn_2SiO_4 and Y_2SiO_5 were 5.82 eV and >6 eV, respectively as measured by ultraviolet absorption spectra.

$BaTiO_3$ was used as a substrate for the EL device to solve question (3) because it has a high dielectric constant (ε_r = 3000-5000) and resistance to temperature as high as 1200°C without deformation or introduction of contaminants into thin film phosphors.

EL devices were prepared with the structure (transparent electrode: ZnO:Al or ITO)/(phosphor thin films: $Zn_2SiO_4:Mn^{2+}$ or $Y_2SiO_5:Ce^{3+}$)/(Substrate: $BaTiO_3$)/(Electrode: Al) and their transferred charge, efficiency, EL-response and time-resolved-spectra were studied. It was also discovered that only electrons stored in the insulator/phosphor interface give effective EL excitation. The EL device threshold voltage and brightness can be improved via a multilayer structure.

CHAPTER 2

THE MATERIAL PROPERTIES OF SILICATES

2.1 Y_2O_3-SiO_2

The phase diagram of Y_2O_3-SiO_2 is shown in Fig. 2.1-1 [Born, 1985].

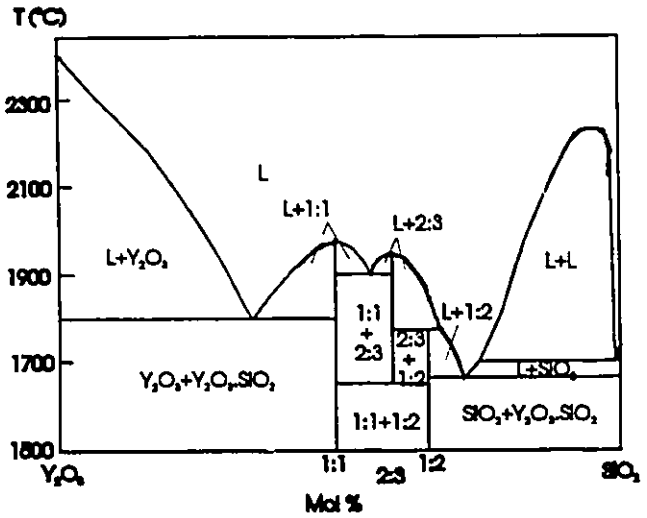

Fig. 2.1-1 The phase diagram of Y_2O_3-SiO_2

Three phases exist in the Y_2O_3-SiO_2 system with Y_2O_3:SiO_2 ratios of 1:1, 1:2 and 2:3. $Y_2Si_2O_7$ undergoes polymorphic changes from Y phase (100°C to 1200°C) to **Z** phase (below 1030°C), to α phase (1030°C to 1225°C), to β phase (1225°C to 1445°C), to γ phase (1445°C-1535°C) and to δ phase (>1535°C). All the phases in the system are efficient

phosphors in spite of the existence of mixed phases and the polymorphism of groups $Y_2Si_2O_7$. The relevant physical properties of Y_2O_3-SiO_2 are summarized in Table 2.1-1.

Table 2.1-1. Physical properties of Y_2O_3-SiO_2 system.

Material	PM	Cryst. structure	SG	Atomic Coord. of Y Atoms	D_{cal}	T_c (°C)	ASM card #
$Y_2O_3 \bullet SiO_2$	A	Monoclin.	$P2_1/c$	7-9 fold	4.55	1190	21-1461
($Y_2[SiO_4]O$)	B	Monoclin.	B2/b	6 & 7 fold			21-1458
$2Y_2O_3 \bullet 3SiO_2$		Hexagonal	$P6_3/m$	6 & 9 fold	4.616		30-1457
($Y_{4.67}(SiO_4)_3O$)							
	Y	Monoclin.	$P2_1/m$	distorted octohedra		1000	
	Z				4.1	1030	
$Y_2O_3 \bullet 2SiO_2$	α	Triclinic	$P\bar{1}$	8-fold distorted cube		1220	38-223
($Y_2Si_2O_7$)	β	Monoclin.	C2/m	regular octohedra	4.01	1225	38-440
	γ	Monoclin.	$P2_1/n$	8-fold distorted cube	4.1	1445	32-1448
	δ	Orthorhom.	Pna2	7-fold polyhedra	4.12	1535	21-1460

Note: D_{cal} = the density calculated, PM = polymorphism, SG = space group.

Y^{3+} ions and the doped substitution RE^{3+} ions have six- to nine-fold oxygen coordination in these structures. The RE cations are strongly electropositive and highly polarized due to the poor screening of the nuclear charge by the f electrons. These strong positive fields produce greater bonding strength than the cations of the same group of elements having only s, p and d electrons. The normal valence of the rare-earth ions is 3+. However, isoelectronic or close isoelectronic groups of ions which possess charges other than 3+ are known in solid-state chemistry, as a result of the distinct $4f^0$, $4f^7$ and $4f^{14}$ stability, i.e.: $Ce^{4+}(4f^0)$, Pr^{4+}; $Sm^{2+}(4^{f6})$, Eu^{2+} and $Tb^{4+}(4f^7)$;$Yb^{2+}(4f^{14})$.

The polymorphism of Y_2O_3:$2SiO_2$ is similar to that of all $Re_2O_3 \cdot 2SiO_2$ which have structures containing isolated Si_2O_7 or Si_3O_{10}+SiO_4 groups. Almost all the research done up to now for this system is on powder phosphors doped by RE^{3+}. ITO (1968) and Liddell (1986) reported the phase transformations of $Y_2Si_2O_7$ as:

$$\alpha \overset{1225^\circ C}{\Leftrightarrow} \beta \overset{1445^\circ C}{\Leftrightarrow} \gamma \overset{1535^\circ C}{\Leftrightarrow} \delta$$

The lattice constants of these phases are listed in Table 2.1-2:

Table 2.1-2 Lattice constants of $Y_2Si_2O_7$.

	a (Å)	b (Å)	c (Å)	α (degrees)	β (degrees)	γ (degrees)	Specific volume ($Å^3$)
γ	7.50	8.06	5.02		112.0		140.7
β	6.88	8.97	4.72		101.7		142.5
γ	5.58	10.86	4.70		96.0		142.2
δ	13.66	5.02	8.15				139.8
α	6.59	6.64	12.25	94.0	89.2	93.1	133.6

The configuration of the Si_2O_7 group is determined by the bonding and polarizing force of the associated cations.

Triclinic α-$Y_2Si_2O_7$ has chain-like groups (Y_2O_7) parallel to $[\bar{1}\ 0\ 1]$ plus additional (SiO_4) tetrahedra (Fig. 2.1-1). The Si ions reside in interstices between the eight-fold Y-O_8 polyhedra. The latter are also parallel to $[\bar{1}\ 0\ 1]$ and form infinite chains by edge sharing. These Y-O_8 chains are connected to each other by corner sharing at every second polyhedron of each chain.

The mineral thortveitite, β-$Y_2Si_2O_7$, has a close packed hexagonal structure. It contains RE^{3+} cations in octahedral holes and silicon in tetrahedral holes in alternating parallel (001) layers. The (SiO_4) tetrahedra show a large degree of distortion as compared to other disilicate configurations. The crystal structures of α- and β-$Y_2Si_2O_7$ are shown in Figs. 2.1-2 and 2.1-3 respectively.

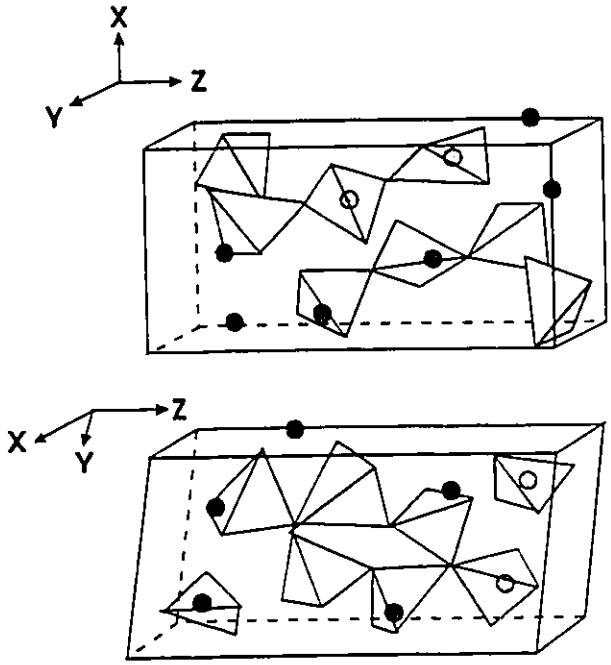

Fig. 2.1-2 Crystal structure of α-$Y_2Si_2O_7$.

The (Si_2O_7) groups are mutually directed along [011] and [1 $\bar{1}$ $\bar{1}$] in γ-$Y_2Si_2O_7$. The coordination of Y atoms does not result in a network, as in structure type β, but rather a ribbon-like arrangement along the c axis.

Two forms of crystal structure with a transformation temperature of 1190°C have been found in Y_2SiO_5 [ITO, 1968] [Liddell, 1985]. One is monoclinic P2/C, the other monoclinic $I2_1/C$ [Felsche, 1973]. P2/C-Y_2SiO_5 has the structure of Ce_2SiO_5, a sheet-like packing

with Y^{3+} ions surrounded by seven or eight oxygen ions. There is an appreciable covalent component in the Y-O bonding. $I2_1/C$-Y_2SiO_5 is isostructural with Sc_2SiO_5 which is composed of chains of (O-Y_4) tetrahedra and of (O_2-Y_6) double tetrahedra in the a_o direction. The infinite chains of (O-Y_4) tetrahedra are connected to the (O_2-Y_6) groups by isolated (SiO_4) tetrahedra. Y^{3+} ions are surrounded by either six or seven oxygen ions.

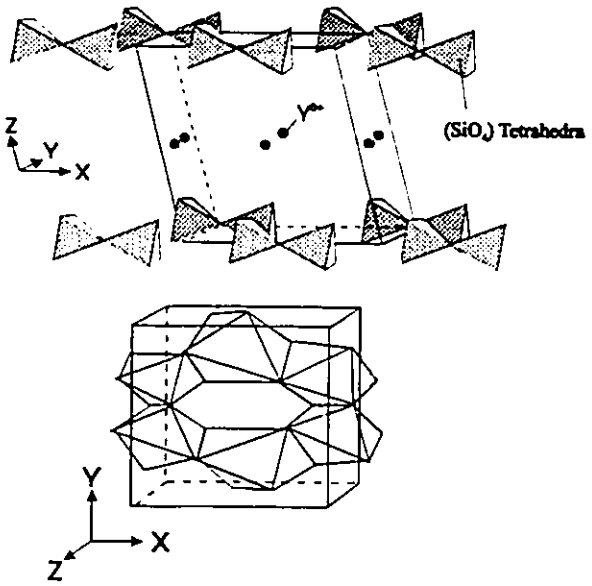

Fig. 2.1-3 Crystal structure of β-$Y_2Si_2O_7$.

A compound was found at the ratio of Y_2O_3:SiO_2 = 2:3. It was $Y_{4.67}(SiO_4)_3O$, 0.67 Y rich with oxygen vacancies [Felsche, 1973]. Data for a yttrium silicate of composition $Y_4Si_3O_{12}$ is reported in the JCPDS index (card: 21-1462). It was obtained from single crystals with a garnet type structure. This 2:3 phase is difficult to synthesize because it gives a mixture of Y_2SiO_5 and $Y_2Si_2O_7$. Polycrystalline thin films were obtained by using

$Y_5(SiO_4)_3N$ as the starting material [ITO, 1968] and by magnetron sputtering [Ouyang, 1994]. These are the only successful growth reported.

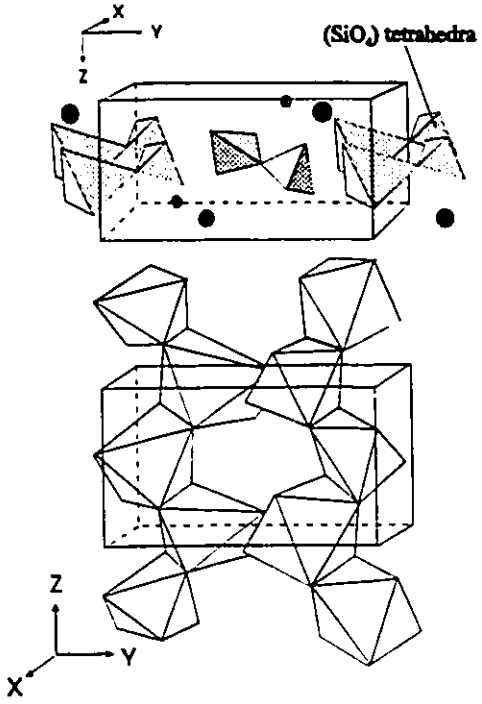

Fig. 2.1-4 Crystal structure of γ-$Y_2Si_2O_7$.

All phases in RE^{3+}-doped Y_2O_3-SiO_2 are good phosphors because the distorted 7-9 fold Y^{3+} sites supply the strong crystal fields which are necessary for the splitting of the inner 4f electron energy levels when RE^{3+} ions substitute for Y^{3+} ions.

2.2 ZnO-SiO_2

The phase diagram of ZnO-SiO_2 is shown in Fig. 2.2-1 [Bunting, 1930]. Willemite, Zn_2SiO_4, is the only effective phosphor phase in this system. Zn_2SiO_4 is known to have three polymorphic phases, α, β and γ [Ingerson, 1948]. But α-Zn_2SiO_4 (Willemite) is the only

stable phase in the binary ZnO-SiO_2 system [Bunting, 1930]. The β and γ phases have been observed as precursors in the formation of Willemite [Williamson, 1964]. Manganese-doped α, β and γ-Y_2SiO_4 luminesce in green, yellow, and red respectively, on UV excitation [Takamori, 1983]. Green α-Y_2SiO_4 is the most important phosphor.

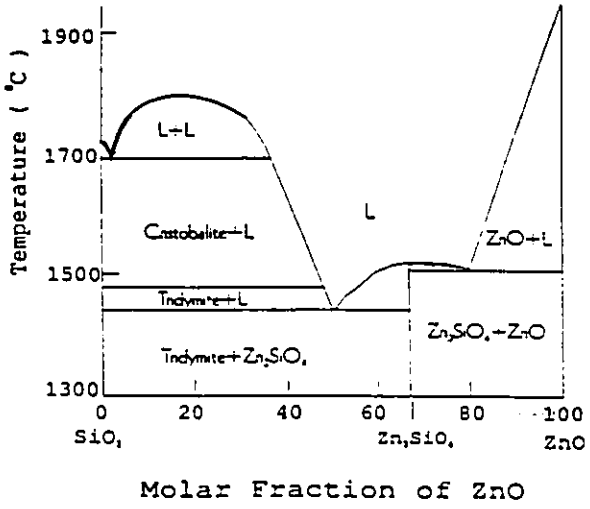

Fig. 2.2-1 Phase diagram of ZnO-SiO_2.

Zn_2SiO_4:Mn, a JEDEC type P-1 phosphor, is used for data display and projection CRTs. Its physical properties are summarized in Table 2.2-1.

The atoms are arranged in layers at six equally separated levels along the c axis in the Willemite structure. This results in crystal cleavage along (0001). Willemite has two inequivalent Zn sites [Klaska, 1978], both with four nearest-neighbor oxygen ions in a slightly distorted, tetrahedral (T_d) configuration. Two inequivalent Zn tetrahedra and one Si tetrahedron alternate in chains parallel to the c-axis.

Table 2.2-1 Physical properties of Willemite:

Crystal structure [Donnary, 1973]	Trigonal, $R\bar{3}$, a = 13.94±1, c = 9.34±1, $\alpha = 108°52'$ Z = 18 (number of formula units per cell)
Symmetry of Zn^{2+} site	T_d (cation tetrahedra)
Cleavage plane	(0001)
Density: $D_{measured}$ D_{cal}	4.0 4.226
Melting point: T_m (°C)	1512
Electron polarizability (λ = 5893Å)	$\chi_{Zn^{2+}}$ (Pauling) = 5.4, $\alpha_{O^{2-}}$ = 21.8
Refractive index: n_g n_p	1.719-1.723 [Chin' Hang, 1970] 1.691-1.694
Hardness (Mohs)	5-6 [Chin' Hang, 1970]

The luminescence of Mn^{2+}-doped Zn_2SiO_4 is assigned to transitions between the spin-orbit components of the $^4T_1$ excitation state and the $^6A_1$ ground state of the Mn^{2+} in T_d coordination. Sharp zero-phonon-lines (ZPL's) were reported at 2.455 eV (504.6 nm) for the Mn_A centers and 2.404 eV (515.3 nm) for the Mn_B centers [Robbins, 1984].

CHAPTER 3

THEORY

Under excitation from external energy, phosphors will generate photons due to the radiative electron transitions from a certain high energy state $E_{initial}$ to a low energy state E_{final}. The conservation of energy indicates:

$$h\nu = hc/\lambda = E_{final} - E_{initial} \tag{3-1}$$

where h is the Planck's constant, ν is the frequency of the photon emitted and λ is the wavelength of photons. The electron transition from $E_{initial}$ to E_{final} is complicated depending on the mechanisms in the materials [Yacobi, 1990]. Below we only discuss the cathodoluminescence and electroluminescence of RE and transition metal (TM)-doped oxide phosphors.

3.1 THEORY OF RARE EARTH AND TRANSITION METAL DOPED PHOSPHORS

The energy levels of RE and TM were measured and found to be located in the forbidden gap of the host lattice by techniques of optically detected magnetic resonance (ODMR) [Godlewski, 1991], thermally stimulated current (TSC) and optical transition current spectroscopy (OTCS) [Clerjaud, 1986]. Three major types of possible electronic transitions are shown in Fig. 3.1-1. The first is 4f-4f and 4f-5d or 3d-3d localized transitions

of RE and TM impurities (Fig. 3.1-1(a)). The second is the so-called charge transfer absorption band where holes are created as impurities ionize (Fig. 3.1-1(b)). The third is electron donation to the conduction band such as $RE^{2+} \rightarrow RE^{3+} + e^-$ (Fig. 3.1.1(c)) [Anderson, 1964]. For wide band-gap silicates ($E_g > 5$ eV), the inner shell energy levels of RE and TM ions are little or less perturbed by the host lattice and the radiative electron transitions are characteristic of RE or TM ions.

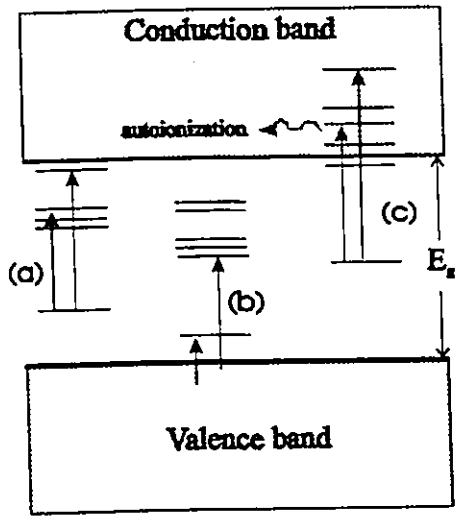

Fig. 3.1-1 Energy diagram of impurity ions imbedded in a crystal and possible electronic transitions.

For luminescence to occur, two conditions must be met. One is that host materials must be well crystallized or polycrystallized, and the second is that active centers (dopants) must be located on the non-symmetric lattice sites which apply strong ligand fields to the

luminescent centers and induce an energy level splitting of the internal shell on the centers. When excited by the external energy, the electron transition within the internal energy level will give out visible light (luminescence). Transition metals such as Mn and Ti have electron structure of $3d^n4s^2$. Therefore, it is not strange why the best candidates for luminescent centers are rare earth (RE) and transition metals (TM).

The characteristic properties of the RE ions are attributable to the presence in the ion of a deep-lying 4f shell which is not entirely filled. The electrons of this shell are often screened by the outer electron shells. The presence of the crystal lattice may or may not affect the positions of these levels. The transitions 4f-4f (more screened) and 4f-5d (less screened) give rise to luminescence. Table 3.1-1 shows the electron configuration of RE atoms and the number of 4f and 5d electrons of RE^{3+} ions in their respective ground state [Blasse, 1979].

Table 3.1-1 Electron configuration of RE atoms and ions in ground state.

Atom	*Electron Config.*	*Ion*	*$4f^n$*	*Ground State Level*
La	$[Xe]5d^16S^2$	La^{3+}	0	$^1S_0$
Ce	$[Xe]4f^15d^16S^2$	Ce^{3+}	1	$^2F_{5/2}$
		Ce^{4+}	0	
Pr	$[Xe]4f^36S^2$	Pr^{3+}	2	$^3H_4$
Nd	$[Xe]4f^46S^2$	Nd^{3+}	3	$^4I_{9/2}$
Pm	$[Xe]4f^56S^2$	Pm^{3+}	4	$^5I_4$
Sm	$[Xe]4f^66S^2$	Sm^{2+}	6	
		Sm^{3+}	5	$^6H_{5/2}$
Eu	$[Xe]4f^76S^2$	Eu^{2+}	7	$^8S_{7/2}$
		Eu^{3+}	6	$^7F_0$
Gd	$[Xe]4f^75d^16S^2$	Gd^{3+}	7	$^8S_{7/2}$
Tb	$[Xe]4f^96S^2$	Tb^{3+}	8	$^7F_6$
		Tb^{4+}	7	
Dy	$[Xe]4f^{10}6S^2$	Dy^{3+}	9	$^6H_{15/2}$
Ho	$[Xe]4f^{11}6S^2$	Ho^{3+}	10	$^5I_8$
Er	$[Xe]4f^{12}6S^2$	Er^{3+}	11	$^4I_{15/2}$
Tm	$[Xe]4f^{13}6S^2$	Tm^{3+}	12	$^3H_6$
Yb	$[Xe]4f^{14}6S^2$	Yb^{2+}	14	
		Yb^{3+}	13	$^2F_{7/2}$
Lu	$[Xe]4f^{14}5d^16^2$	Lu^{3+}	14	

Note: [Xe] is the electron structure of Xe.

The details of energy diagrams and atomic spectra of RE and TM are well studied [Hufner, 1978] [Dieke, 1968]. From the major peaks and optical terms $^{25+1}L_J$ reported, we

can estimate the possible colour of a specific active centre where S, L and J are quantum numbers of spin, orbit and total angular momentum, respectively.

Fig. 3.1-2 is the energy diagram of some RE ions [Blasse, 1979]. The hatched broad bands indicate charge-transfer Er^{3+} or $4f^n$ - 5d stages (Ce^{3+}, Eu^{2+}, Tb^{3+}). Levels labelled with black half-circles are levels from which luminescence is observed. The energy levels of these bands depend to a great extent on the lattice.

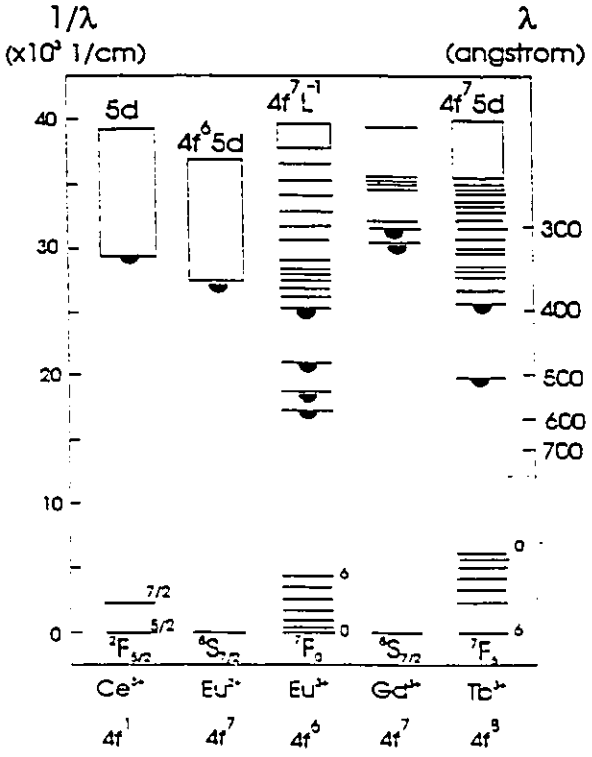

Fig. 3.1-2 Energy diagram of some ions of rare earth metals in oxide host lattices.

The bands in Fig.3.1-2 fall into two groups. In the first group one of the 4f electrons is raised to the higher 5d level: $4f^n$ - $4f^{n-1}5d$. This 5d level can be strongly influenced by the

lattice. Examples are Ce^{3+}, Tb^{3+}, and Eu^{2+} ion. For Eu^{2+}, the $4f^65d$ level lies so low that the $4f^7$ levels present (except for the ground level) are completely overlapped. In the second group, one of the electrons in the surrounding anions is promoted to the 4f orbit of the central R ion (***charge transfer state-CTS***), $4f^n \rightarrow 4f^{n+1}L^{-1}$ (where L indicates a ligand), such as Eu^{3+}. Therefore, the position of this energy band depends on the nature of the surrounding ions.

Whether a RE ion prefers either $4f^{n-1}5d$ state or charge transfer state, $4f^{n+1}L^{-1}$ depends on which state has lower energy. It is known from Hund's rule that a state with a completely or half-filled electron shell is the most stable. In the case of Tb^{3+} ($4f^8$, half-filled plus one), the 4f shell releases an electron, and the transition $4f^8 \rightarrow 4f^75d$ takes place at relatively low energy, while in the case of Eu^{3+} ($4f^6$, half-filled less one) the 4f shell readily accepts an electron and thus the charge-transfer state, $4f^7L^{-1}$ has lower energy.

3.2 PRINCIPLE OF CATHODOLUMINESCENCE

Cathodoluminescence is widely used in CRTs where powder phosphors are impinged upon by electrons accelerated under the voltage of 1-50 kV and luminescence is generated.

Unlike photoluminescence which selectively excites particularly active centers depending on the excitation energy hv, electron beam excitation in general leads to emission by all the luminescence mechanisms present in the material. Excitation-de-excitation can be excited, for example, by direct collision or resonant energy transfer from an electron-hole recombination. On the other hand, electron excitation may produce orders-of-magnitude greater carrier generation rates than typical optical excitation. This is especially an advantage

for wide-band-gap oxides where electron energy up to 10 kV can be used without inducing atomic displacement damage.

Defects and material properties can be investigated by the number of peaks, peak positions, peak broadening, peak intensities and the relative peak intensities from a CL spectrum taken.

We studied the cathodoluminescence of both powder and thin film phosphors. The purpose is to find the best RE dopants for RGB color display and to find the best composition for the sputtering target materials. The phosphors we studied are: RE^{3+} (Ce^{3+}, Pr^{3+}, Nd^{3+}, Sm^{3+}, Eu^{3+}, Gd^{3+}, Tb^{3+}, Er^{3+})-doped Y_2O_3, Y_2SiO_5, $Y_{4.67}(SiO_4)_3O$, $Y_2Si_2O_7$ and Mn^{2+}-doped Zn_2SiO_4. Y_2O_3 was found unsuitable for preparing the crystallized thin film due to its high melting point (2410°C) and the deposition condition for $Y_{4.67}(SiO_4)_3O$ being too critical. The work is concentrated on Y_2SiO_5, $Y_2Si_2O_7$ and Zn_2SiO_4. For certain materials, the cathodoluminescent spectrum is compared with the electroluminescent spectrum.

3.3 PRINCIPLE OF ELECTROLUMINESCENCE

When an electric field above 10^6 V/cm is applied to a phosphor layer, electrons with enough kinetic energy in the layer will excite the active centers and give luminescence. The electrons injected into the phosphor must be 'loss free' to accumulate enough energy before meeting an active centers. For example, in order to generate a photon with an energy of 2.2 eV (wavelength 560 nm, green), some of the electrons injected must have a kinetic energy greater than 2.2 eV.

Mn^{2+}-doped ZnS is known to be the best EL phosphor discovered, having 'hot electrons' distributed between 5-13 eV [Müller, 1993]. According to the tunneling model, at high fields above 1 MV/cm, electrons injected from the interface state will gain 1 eV per 10 nm traveled. Therefore, an electron with a energy of 7 eV will have a mean free path λ_{mfp} of 70 nm. This is incredibly high as compared to the λ_{mfp} of electrons in metal which is about 1-10 Å [Ashcroft, 1976].

Under such high field near the breakdown voltage, the multiplication, or avalanching, of electrons may make the device break down. Therefore, high strength dielectric layers are needed to protect the device. Fig. 3.3-1 is the model of a TFEL device with a double insulated structure [Müller, 1984] which is necessary to protect the device from breakdown. The insulators chosen are Y_2O_3, Al_2O_3, Ta_2O_5, SiO_2, Si_3N_4, SiAlON, MgO, $BaTiO_3$, etc., the electrical properties of which are listed in Table 3.3-1 [TiKu, 1984].

Table 3.3-1 Material properties of some insulator films.

Material	ε_r	E_B (M V/cm)	Capacity ($\mu C/cm^2$)	Resistivity ($\Omega \cdot cm$)	Remarks
Y_2O_3	12-14	1-3	1.2-3.2	10^{11}-10^{13}	moisture sensitive
Al_2O_3	10-11	1-3	0.95-2.7	10^{12}	reaction with ITO
Si_3N_4	7	5	3.1	10^{12}	poor adhesion
Ta_2O_5	25	2-3	4.4-6.5	10^{12}	reaction with ITO
SiAlON	8	8	5.6-6.4	10^{13}	good barrier, less stress
$BaTiO_3$	200	1		10^{11}	must be amorphous

Note: The above parameters may change depending on the preparation method and condition

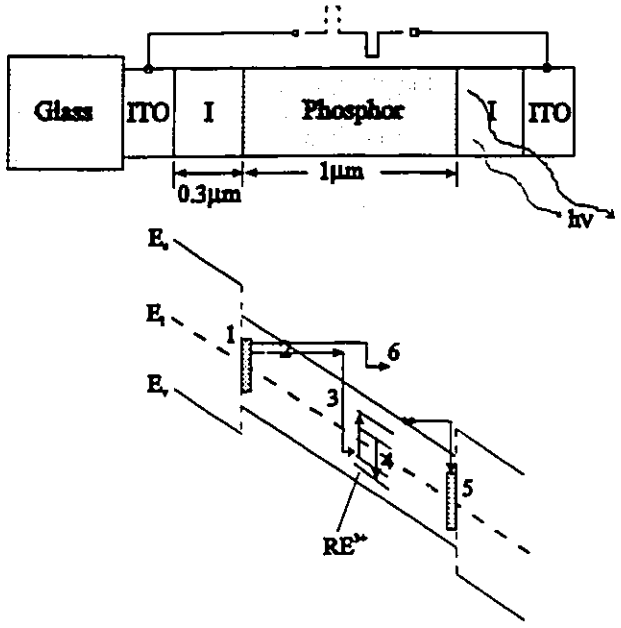

Fig. 3.3-1 Simple model of a TFEL device, showing basic processes indicated and numbered under applied voltage.

The basic processes are:

(1) tunneling emission of electrons from the interface states of the left (cathode) interface.

(2) "loss-free" acceleration of electrons in phosphor layer.

(3) impact excitation of RE^{3+} ions by the high kinetic energy electrons.

(4) radiative (or non-radiative) de-excitation of RE^{3+} luminescent centers.

(5) carrier captured by interface state at the right (anode) interface.

(6) carrier multiplication by valence electron impact ionization leading to an accumulation of positive space charge in the bulk.

The trapped charge boundary conditions are necessary in a display application to get a high internal field. When the external voltage is reversed with the trapped charge, the internal field is doubled. The steepness of the E(x) curve shown in Fig. 3.3-1 is greatly influenced by impact ionization and space charge.

For the wide band gap oxide phosphors such as Zn_2SiO_4, will the above model still work? The answer is yes, because the electrons injected into the oxide phosphor films also come from the insulator-phosphor interface according to the time-resolved spectra we measured. The details will be discussed in Chapter 6.

3.4 EL STRUCTURES AND EL PROPERTIES

One of the most useful thin film electroluminescent device structures is the MISIM/substrate as shown in Fig 3.4-1 where M is metal (Al, Au) or transparent electrode (ZnO:Al, ITO), I is insulator (Al_2O_3, Ta_2O_3, $BaTiO_3$, SiO_2, Y_2O_3, etc.) and S is the phosphor layer [Mach, 1982]. However, this structure is unsuitable for oxide thin film phosphors which need to be annealed up to 900°C - no electrode can withstand this temperature. We prepared our EL device using the modified MISIM structure.

Because $BaTiO_3$ has a high dielectric constant ε of about 3000-5000 depending on the substrate preparation and the electrical field applied, the voltage ratio applied on the phosphor layer is r:

$$r = V_s/V_i = C_i/C_s \qquad (3.4\text{-}1)$$

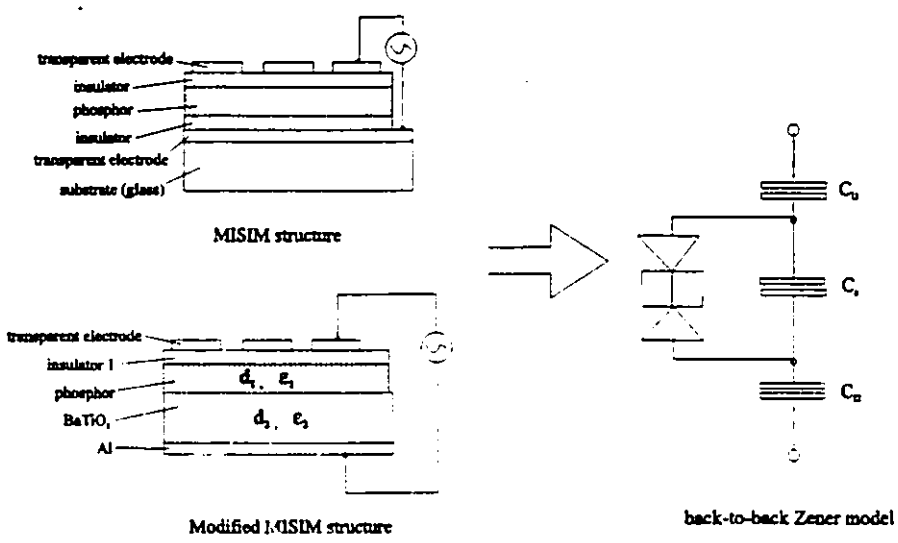

Fig. 3.4-1 TFEL device structures.

where $1/C_i = 1/C_{i1}+1/C_{i2}$. For the modified structure without a dielectric layer, $r = \varepsilon_2 d_1/\varepsilon_1 d_2$. A typical Zn_2SiO_4 thin film device has the following parameters: $\varepsilon_1 = 10$, $d_1 = 1$ μm, $\varepsilon_2 = 4000$, $d_2 = 0.8$ mm, giving $k = 0.5$. That is to say, half of the voltage on the device is applied on Zn_2SiO_4 thin film. Another advantage of $BaTiO_3$ substrate is its high temperature stability up to 1200°C without serious deterioration of the active film due to the inter-diffusion mechanism.

One of the important parameters of a phosphor thin film is its decay time τ which is the time required for an excited photon pulse to decrease to $1/e = 0.368$ of its peak. Different applications need phosphors of different τ. τ is also a measure of the probability

of an excited center to decay radiatively defined as η_{lum} where $\eta_{lum} \propto 1/\tau$ [Muller, 1992]. τ can be measured directly from the time resolved luminescent spectrum. From the decay curves measured, we can also understand the mechanism of the device.

Another device property is the transferred charge which is also a measure of device efficiency. When electron avalanching takes place in the active layer (phosphor), the active layer changes its electrical property from a 'loss-free' insulator to a 'leak' capacitor and the voltage will be redistributed on each of the multilayers of the device. The 'leaky' current or transferred charge can be measured by using a Sawyer-Tower circuit as shown in Fig. 3.4-2 where the Q-V loop area is used to measure luminous efficiency of an EL panel.

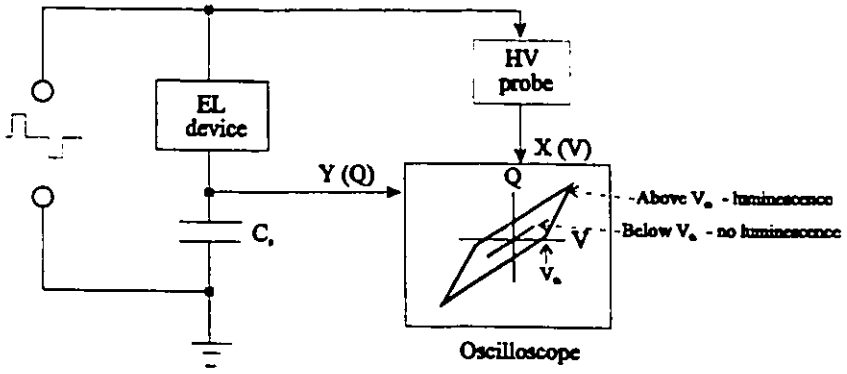

Fig. 3.4-2 The Sawyer-Tower circuit for measuring the charge flow in a.c. TFEL. The sense capacitor C_s is very large and does not affect device operation.

3.5 COLOR COORDINATES

Color displays use the electronic RGB 'color space', in which a color is defined by the relative proportions of red, green and blue display primitives (or RGB phosphors in a display)

required to produce it. This makes it is easy to produce full color pictures by addressing individual phosphor pixels. The reason for using color space is due to the nature of human eyes.

The photoreceptors of human eyes consist of rods and cones. Rods are all identical and can only identify the number of quanta absorbed instead of the wavelength of these quanta while cones are wavelength sensitive and can be classified into three kinds because they contain different light sensitive pigments. The tristimulus, $r(\lambda)$, $g(\lambda)$, $b(\lambda)$ of colors are based on the three classes of cones of human eyes. These three classes have broad and overlapping spectral sensitivities and can be loosely referred to as long wavelength sensitive (L), medium wavelength sensitive (M) and short-wave sensitive (S). To extract chromatic information from these signals, the outputs of different classes of cones must be compared.

These three classes of cones are neither equally numerous nor equally distributed over the retina. It is estimated that there are 6.8 million cones and about 115 million rods. The ratios of three cones are L : M : S ≈ 6 : 3 : 1 approximately [Travis, 1991].

Psychophysics is the investigation of the complete system by the study of psychological responses to physical stimuli. The physics refers to the measurement of the stimulus; the psychology refers to the measurement of the sensation. The spectral range of colours can be approximately classified in Table 3.5-1 [MacAdam, 1985]:

Table 3.5-1 Spectral range of colors

Color	Wavelength (nm)
violet	400-450
blue	450-490
green	490-560
yellow	560-590
orange	590-630
red	630-700

In 1931, the International Commission of Illumination (CIE) recommended an international agreement on colors in terms of ***equivalent stimuli***, that any color can be expressed by tristimulus values, x, y, and z (Appendix B). The value x represents the amount of reddish primary that has higher saturation than any obtainable red. The value y represents the amount of green primary that is approximately the same hue as the spectrum color whose wavelength is 520 nm. The value of z represents the amount of a blue primary that is considerably more saturated than, but of the same hue, as the spectrum color whose wavelength is 477 nm. In this way, for example, one Watt of monochromatic light with a wavelength 500 nm can be expressed by tristimulus values X = 0.0049, Y = 0.3230 and Z = 0.2720. For two beams of lights with the same color but different brightness (different luminescent factor) , their x, y, and z are different but the ratios of x:y:z are the same. For convenience, normalized chromaticity coordinates are used to evaluate colors.

The CIE system is a means by which visible colors can be specified, measured, and reproduced. The new chromaticity coordinates are defined as:

$$x = X/(X+Y+Z) \tag{3.5-1}$$

$$y = Y/(X+Y+Z) \tag{3.5-2}$$

$$z = Z/(X+Y+Z) \tag{3.5-3}$$

and

$$x+y+z = 1 \tag{3.5-4}$$

Therefore, only two of these quantities are independent. The graphical representation of chromaticity is shown in Fig. 3.5-1. This chromaticity diagram has the following characteristics:

(a) The solid line is the locus of all spectrum colors (monochromatic); any real color must be located within the locus.

(b) The natural white light c has coordinates of x=0.3101 and y=0.3163.

(c) The color B has an excitation purity of CB/CA and a dominant wavelength of 560 nm.

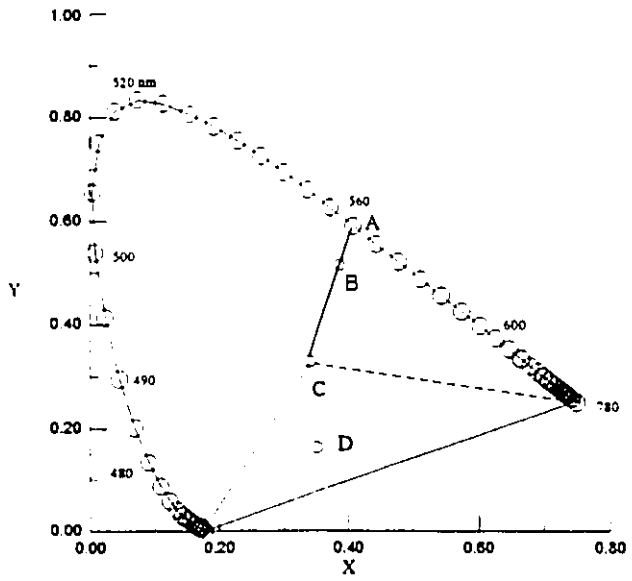

Fig. 3.5-1 CIE chromaticity diagram.

(d) The NTSC set of primaries are defined as:

Table 3.5-2 NTSC primaries

Primary	CIE x	CIE y
Red	0.67	0.33
Green	0.21	0.71
Blue	0.14	0.08

(e) Any real light that lies within the solid line but above the dashed line in Fig. 3.2-1 can be considered a mixture of illuminant C and the spectrum of a certain wavelength, and B is located on the line between A and C according to the additive properties of color. This is the basis of the monochromatic-plus white method of colorimetry.

(f) Colors that lie below the dashed lines are purples or magentas which cannot be expressed by the addition of C and A; however, they can be expressed as the addition of two spectrum wavelengths, one on the left arc and the other on the right arc. The concept of purity is inapplicable to a purple because no spectrum wavelength appears on the bottom line.

There are two ways to measure color coordinates (tristimulus values). One is using photometers with three RGB filters and the other, more accurate way, is to calculate the spectrum measured by using tristimulus values [Appendix B]. In our samples, the characteristic luminescent peaks of RE^{3+} are usually very sharp with a half peak width around

a few nm. Calculation according to the spectrum is the only way to get accurate tristimulus values.

A program (Appendix C) was designed to calculate tristimulus values using the algorithm shown in Fig. 3.5-2, where CIE.XYZ is the tristimulus of the 1931 or 1963 CIE color standard with either 2° or 10° field size; CIE.Rθ is the CIE.XY data (normalized CIE.XYZ data) in polar coordinates with illuminant C (average noon daylight in USA) as the origin; H_λ is the phosphor spectrum measured; and h_λ is the photo-multiplier response as a function of wavelength.

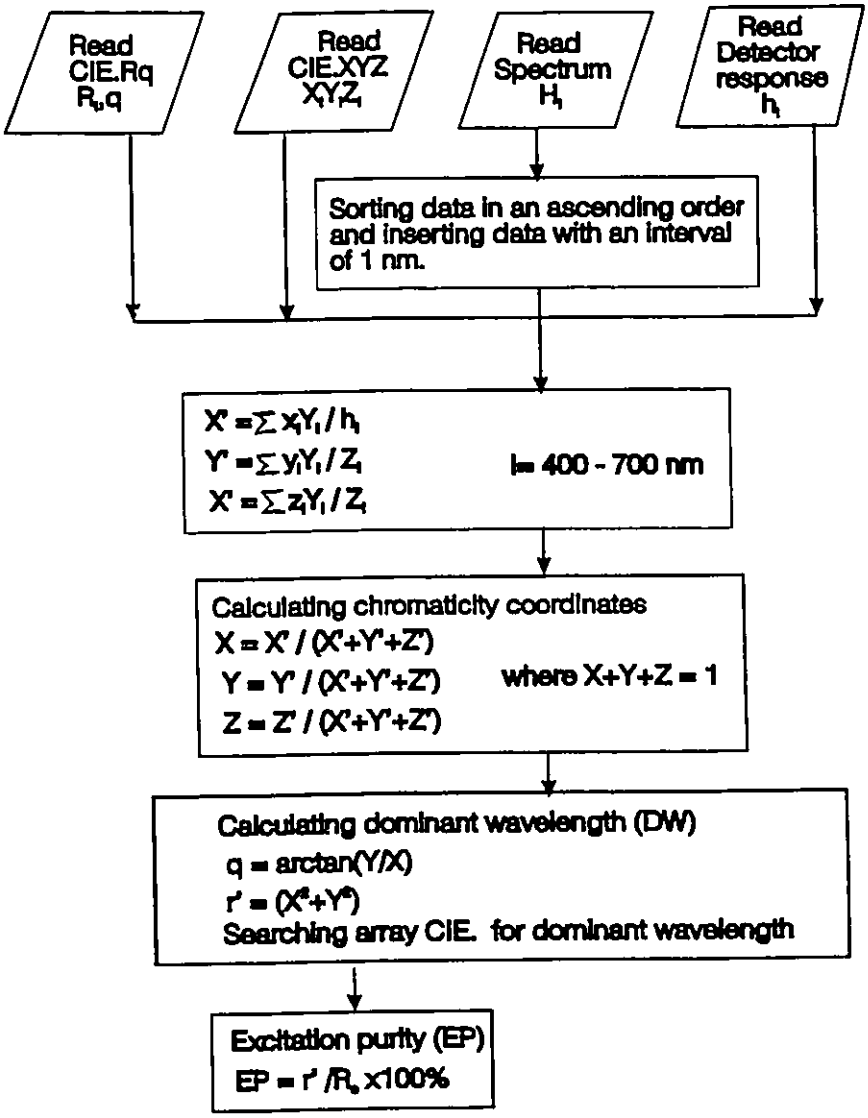

Fig. 3.5-2 Flow chart for chromatic coordinates calculation:

CHAPTER 4

EXPERIMENTAL PROCEDURE

4.1 POWDER PHOSPHOR PREPARATION

Powder phosphors were prepared using solid reactions by mixing well, using mortar and pestle, suitable quantities of high purity (>99.99%) Y_2O_3, SiO_2, ZnO powders and small quantities of RE_2O_3 (1~10% mol.) and MnO (1~2% mol.) dopants, dry pressing by using a small quantity of acetone to assist better molding, and then sintering to 1200°C for more than 20 hours. The well sintered phosphor has uniform luminescent properties (spectra and intensity) examined by CL measurement on the fresh surfaces of phosphors.

4.2 THIN FILM DEPOSITION BY MAGNETRON SPUTTERING

We built up a magnetron sputtering system as shown in Fig. 4.2-1 where the sputtering gas is controlled by a MSK-1250A flow controller which has a working range of 1 mtorr to 10 torr. A US GUN II with a maximum working power of 500W is used as the sputtering gun on which the target material is placed. The target is water-cooled for releasing the heat generated by the impingement of sputtering gas atoms. Substrates can be heated up to 600°C. Oxide and nitride compounds can be deposited by reactive sputtering using a suitable active gas. The theory of sputtering is referred to in appendix D.

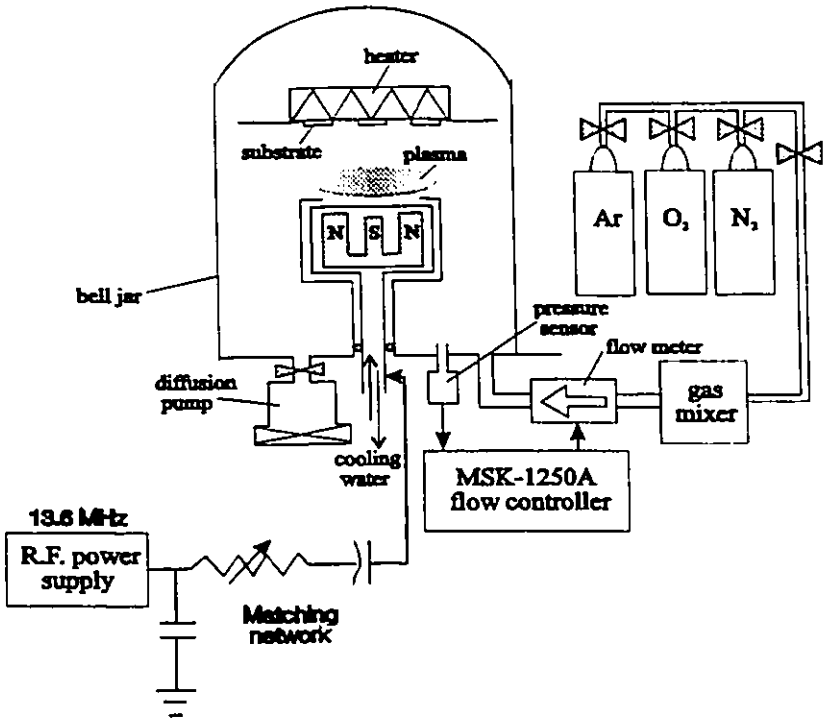

Fig. 4.2-1 Set-up of magnetron sputtering

The major sputtering parameters that influence the chemical, structural and mechanical properties of thin films are target material, substrate temperature, substrate-target (S-T) distance, sputtering power, sputtering gas and pressure. These parameters will be discussed later. For thin film phosphors in this thesis, the best parameters discovered are shown in Table 4.2-1.

Table 4.2-1 Parameters in depositing thin film oxide phosphors:

target diameter	50 mm
target-substrate distance	30-40 mm
vacuum chamber background pressure	$<2\times10^{-6}$ Torr
substrate temperature during growth	300-450°C
sputtering gas	Ar
sputtering pressure	5-20 m Torr
film thickness	9000Å±10%

4.3 THIN FILM COMPOSITION ANALYSIS

The composition of the sputtered thin film phosphor is evaluated by Rutherford Back-scattering (RBS). RBS is suitable for multi-component thin films with a great difference in atomic weight of their components. RBS relies on the use of very high energy (MeV) beams of low mass ions which have the property of penetrating thousands of angstroms or even microns deep into films or film-substrate combinations. Interestingly, such beams cause negligible sputtering of surface atoms.

The geometry of RBS is shown in Fig. 4.3-1 where ^{15}N is used as an incident beam with a mass M_o (=15) and energy E_o. An elastic collision between the ion projectile and the surface atoms of mass M (Y, Si or O) occurs such that afterwards the ion energy is E_1. The collision is insensitive to the electronic configuration or chemical bonding of target atoms, but depends solely on the masses and energies involved. As a consequence of conserving energy and momentum, it is shown that [Ohring, 1992]:

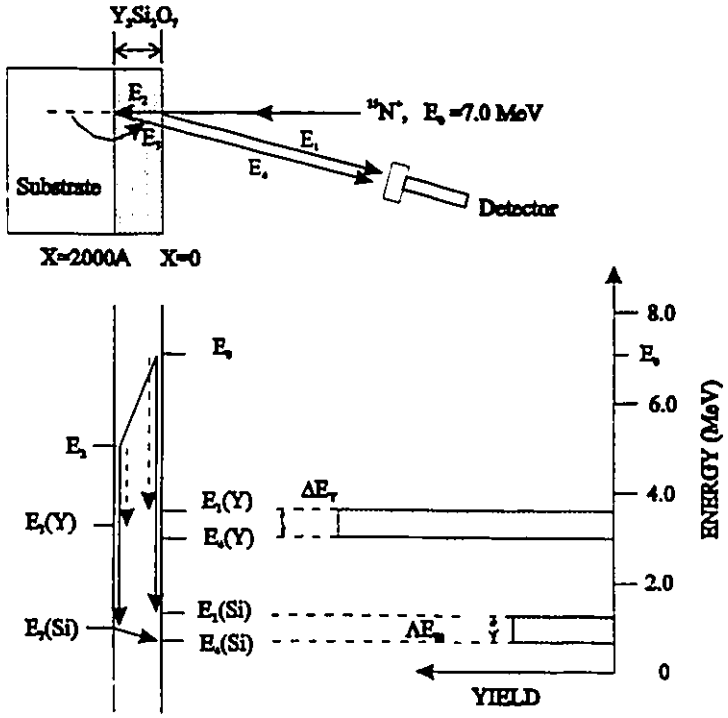

Fig. 4.3-1 Geometry of scattering and notation of energies at the front and back surfaces of a 2000Å thick $Y_2Si_2O_7$ film. A schematic RBS spectrum rotated by angle 90° is also shown.

$$E_1 = \left\{ \frac{(M^2 - M_o^2 \sin\theta)^{1/2} + M_o \cos\theta}{M_o + M} \right\}^2 E_o \qquad (4.3\text{-}1)$$

where θ is the scattering angle. For a particular combination of M_o, M, and θ, the simple formula

$$E_1 = K_M E_o \qquad (4.3\text{-}2)$$

relates the energy of emergent ions to that of the incident ions. K_M is the kinematic factor and can be deduced from (4.3-1).

As an example, let's consider an incident beam of ^{15}N (M_o=15) at E_o=7 MeV, and angular position θ=165°. Then, K_Y=0.5117 and K_{si} =0.096. This means that if a 7 MeV ^{15}N ion collides with Y atoms located on the surface of a yttrium silicate thin film, it will scatter into the detector with an energy of 3.58 MeV, while scatter by a Si will have a backscattering energy of 0.672 MeV.

4.4 BAND GAP AND ULTRAVIOLET ABSORBANCE MEASUREMENT

The band gap of the material can be measured by observing the absorption edge of the ultraviolet spectra. Zn_2SiO_4 and $Y_2Si_2O_7$ thin films with a thickness of about 1 μm were prepared on the fused quartz substrate. A HP 8451A diode array spectrophotometer was used to take the UV absorbance spectra. The set-up is shown in Fig.4.4-1 where the mono-chromized light source can change the wavelength from 190 nm to 800 nm. The absorbance of thin film was taken by deducting the absorbance of the substrate. The measured curve of absorption A vs wavelength is not so sharp for determining the band-gap E_g, therefore, the curve is redrawn according to the equation [Pankove 1971]:

$$(Ah\nu)^2 = C'(h\nu - E_g) \qquad (4.4\text{-}1)$$

where A is the absorbance of the film, C' is the constant, ν is the frequency of the light and E_g is the band-gap of the film.

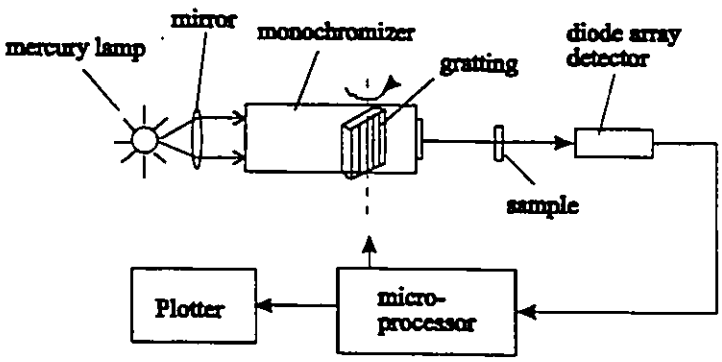

Fig. 4.4-1 Set-up for absorbance measurement.

4.5 CATHODOLUMINESCENT MEASUREMENT

When an electron beam is accelerated under a dc voltage of 10 kV, it can penetrate about 600 nm into Si substrate. Since the range of accelerated voltage of our system is 0-5 keV, the thickness of phosphor thin films should be greater than 300 nm. (111)Si wafer is used as substrate for CL intensity and spectra measurements.

4.5.1 CL Intensity

The photometric intensity of phosphors was measured using a Minolta LS-100 luminance meter. The measurement range of the meter is 0.001 to 49990 cd/m^2 (0.001 to 14590 fL) and the spectral response of the photocell is filtered to match the CIE (Commission Internationale de l'Eclairage) relative photopic luminosity response. The diagram of the measuring system is shown in Fig. 4.5.1-1.

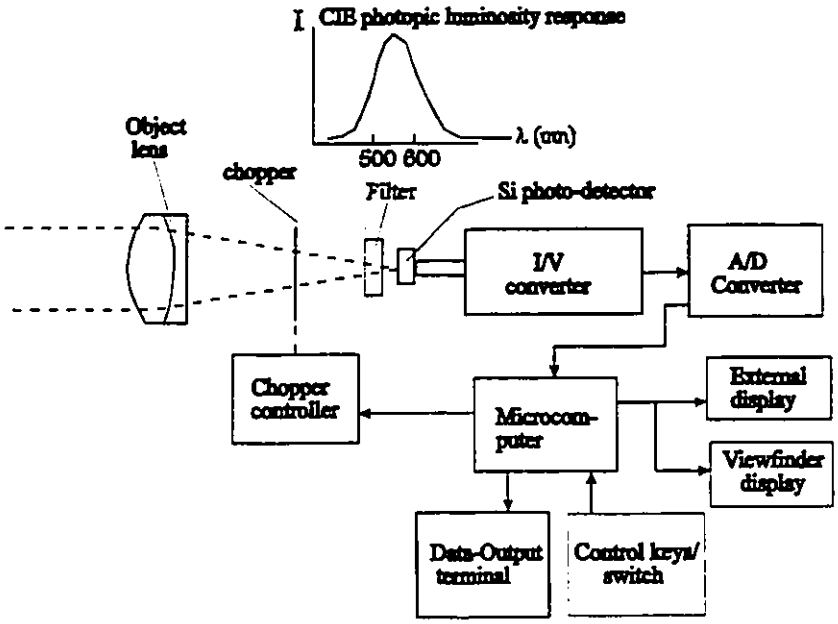

Fig. 4.5.1-1 Set up for photopic luminosity intensity measurement.

4.5.2 CL Spectra

The set-up for measuring CL spectra is shown in Fig. 4.5.2-1 where the phosphor sample is impinged upon by electrons accelerated at the voltages of 0-5 kV and the luminescence generated by the electrons are recorded by the system.

In order to protect the filament from oxidation, samples and electron source must be put in high vacuum of about 10^{-8} Torr. Electrons accelerated under 5 kV can penetrate sample surface by 1000-2000Å. Luminescencent photons emitted from the glass window are guided by mirrors to a monochromator which is composed of a grating and two slits. Photons are detected using a photo-multiplier which has a gain of about 10^6-10^7 electrons/photon

[Skoog, 1985] and a response speed of 10^{-9} s [Pohl, 1993]. Noise in the signal is rejected by a lock-in amplifier. By turning the grating angle, calibrating (using a 6328Å laser and a mercury lamp), luminescence intensity vs. wavelength can be measured. Due to the slit width and calibration error, the measurement error of the wavelength can be less than 0.5 nm. In consideration of the photo-multiplier response with regard to wavelength as shown in appendix A, detected spectra are corrected.

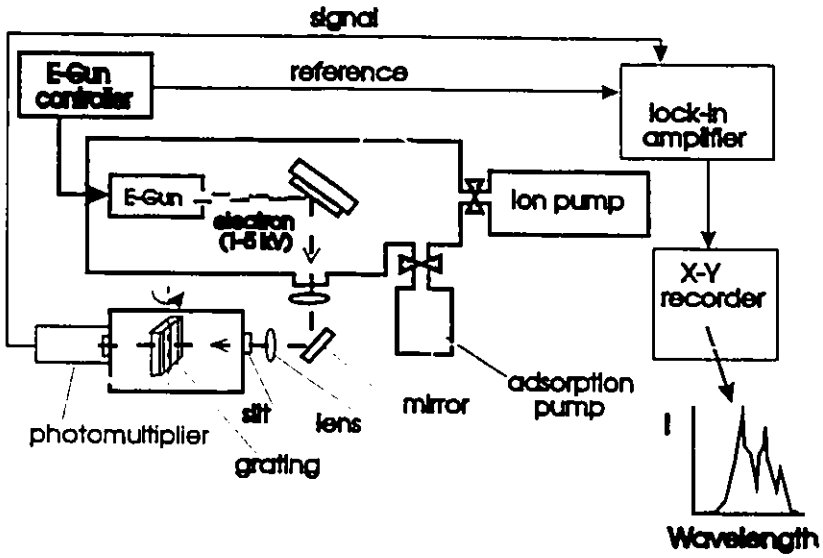

Fig. 4.5.2-1 Diagram of photo-spectroscopy

4.6 ELECTROLUMINESCENT MEASUREMENT

4.6-1 Device Preparation

We prepared the ITO (or ZnO:Al)/phosphor/$BaTiO_3$/Al devices with either single phosphor layer, alternating different-phosphor layers or alternating insulator-phosphor layers.

Zn_2SiO_4:Mn and Y_2SiO_5:Ce thin films were prepared on $BaTiO_3$ substrates by magnetron sputtering using powder phosphors as the targets and were post-annealed at 950°C for 3 hours. Mn and Ce concentrations were measured to be 2% mole and 3% mole by Rutherford backscattering.

$BaTiO_3$ substrates were prepared by hot pressuring high purity $BaTiO_3$ powder (Aldrich Chem. 99.99%) with an average powder diameter of about 1-2 μm at 1350°C and then cut into pieces with a thickness of 0.8±0.05 mm. Post-annealing to 800-900°C is necessary to oxidize black oxygen-deficient ceramic chips. The last step is to polish the surface with 6 μm and then 1 μm diamond pastes alternately. After cleaning by detergent and ultrasonic cleaner in acetone liquid, the substrates are ready for use.

The dielectric constants ε of $BaTiO_3$ substrates were calculated from the capacitance measurement of Al/$BaTiO_3$/Al capacitor. The ε of $BaTiO_3$ is within the range of 500-5800 at the frequency of 400 Hz at room temperature.

Indium Tin oxide (ITO) was used as a top transparent electrode. ITO thin films were deposited by magnetron sputtering at an Ar atmosphere of about 20 Torr. Post annealing at 200-300°C for 10 minutes will decrease its sheet resistance almost an order from $R_{\square}$ = 100-300 $\Omega/_{\square}$ to 10-20 $\Omega/_{\square}$.

4.6.2 EL Spectra

In Chapter 3, we discussed the importance of a luminescent spectrum from which we can discover not only the mechanism of the luminescence, but the ligand field effects and also

the color coordinates of the phosphor. When an ac field is applied on the device, electro-luminescence is observed and the EL spectrum is taken by the equipment as shown in Fig. 4.6.2-1. For the decay time measurement, a photo-multiplier is suitable for very fast dynamic response and extremely weak light intensities.

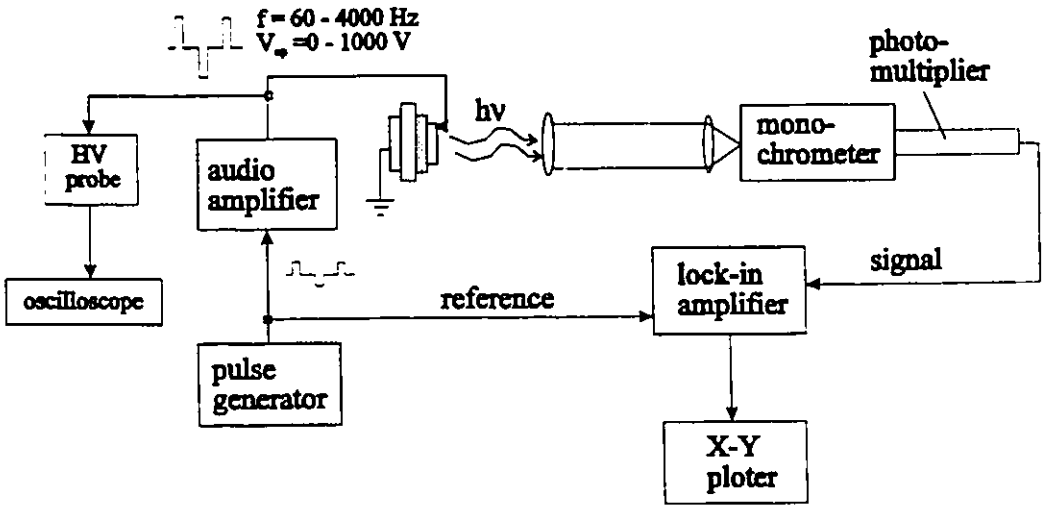

Fig. 4.6.2-1 Set-up for EL spectra measurement.

A digital HP memory oscilloscope is used to average the signal, eliminating noise coming from background light.

4.6.3 Decay Time Measurement

Fig. 4.6.3-1 is the diagram of measuring the decay time of the phosphor. A HP memory oscilloscope is used to filter the background noise from photomultiplier. The decay characteristic of the phosphor was studied by change the excitation pulse width.

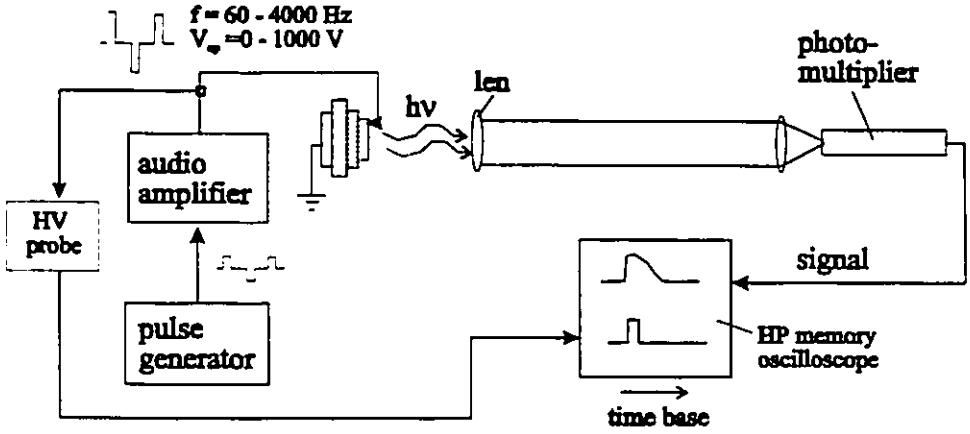

Fig. 4.6.3-1 Set-up for the measurement of EL decay time.

CHAPTER 5

RESULTS AND DISCUSSION - THIN FILM DEPOSITION AND CHARACTERIZATION

5.1 TARGET VS THIN FILM COMPOSITION

Using Rutherford backscattering and X-ray diffraction, we found the relationship between the powder target and the thin film composition deposited by using the sputtering conditions in Table 4.2-1. The results are shown in Table 5.1-1.

Table 5.1-1 Thin film composition with regard to that of powder target

Composition of powder target	*Composition of thin films*
$Y_2O_3 : SiO_2 = 1 : 1.5$	$Y_2O_3 : SiO_2 = 1 : 1$
$Y_2O_3 : SiO_2 = 1 : 3.3$	$Y_2O_3 : SiO_2 = 1 : 2$
$Y_2O_3 : SiO_2 = 1 : 2.5$	$Y_2O_3 : SiO_2 = 2 : 3$
$ZnO : SiO_2 = 3 : 1$	$ZnO : SiO_2 = 2 : 1$

Sputtering target material is the most important factor in controlling thin film composition. Although silicon has a higher sputtering yield than that of yttrium, its sticking coefficient on the substrate is much smaller than yttrium [Somekh, 1989]. On the other hand, the sputtered Si ions may have a less sharp angular distribution at the normal central direction to the target than that of Y ions as reported in data for the preferred ejection of heavier

components [Belz, 1983] because Si atoms have less atomic weight and are easily scattered by the gas atoms. The composition of the thin film is controlled by suitable RE-doped powder target material with a Y_2O_3:SiO_2 ratio between 1:2 and 1:3.3 in consideration of the higher sticking coefficient of Y during sputtering. The deviation of target compositions from that of thin films is explained in appendix D.

5.2 SPUTTERING PARAMETERS

5.2-1 Substrate Temperature and Deposition Rate

Fig. 5.2.1-1 is the X-ray diffraction pattern of Zn_2SiO_4 thin films post-annealed at 900°C and 1000°C respectively. The relative CL brightness ratios of the above films post-annealed at 810°C to those at 900°C and 1000°C are 1:3.4 and 1:3.6, respectively. Since the luminescence is strongly dependent on the local ligand field and the structure arrangement of the nearby atoms, the CL intensity of a phosphor is more sensitive to the crystallization of the material than the X-ray diffraction and it can be used as a means of determining the start of crystallization. In this way, the crystallization starting temperature of Zn_2SiO_4 thin films is determined as 900°C. Using the same method we determined that a post-annealing temperature of 1000°C is needed for Y_2SiO_5 and $Y_2Si_2O_7$.

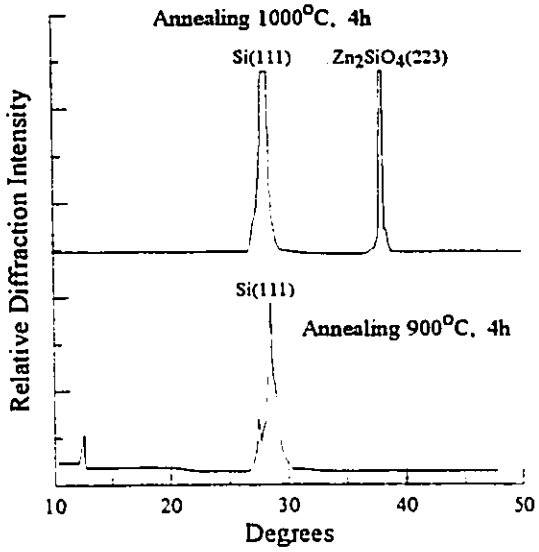

Fig. 5.2.1-1 The X-ray diffraction pattern of Zn_2SiO_4 thin films annealed at 900°C and 1000°C. The latter shows a (223) preferred orientation of the wellemite structure.

The deposition rate of the thin film depends mainly on the r.f. power, the target-substrate (T-S) distance, and the target material. As described in Appendix 4, the US' GUN we used has a positive space charge (PSC) sputtering mode and the deposition rate proportional to the r.f. power. The deposition rates for some of the materials were measured and shown in Fig. 5.2.1-2.

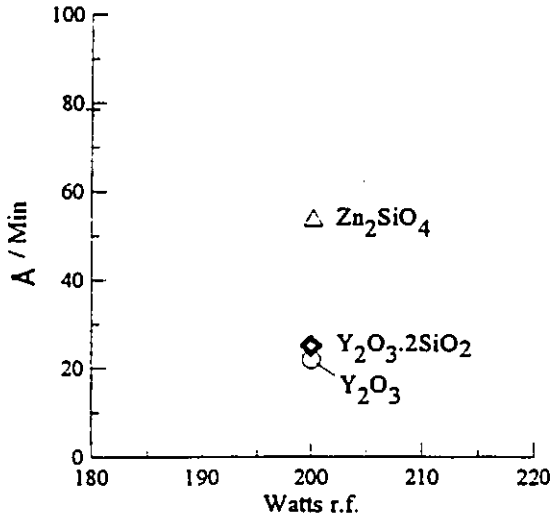

Fig. 5.2.1-2 Deposition rates of thin films deposited at 2×10^{-3} Torr of Ar at a target-substrate distance of 30 mm. The composition listed are target materials.

5.2.2 Target-Substrate Distances $D_{T\text{-}S}$ and Pressure P_s

$D_{T\text{-}S}$ determines both thin film thickness distribution and deposition speed. The thin film thickness distribution and the target etching are closely related to the distribution of $B_{//}$. From the measured data in Fig. 5.2.2-1, it is observed that the less variation of $B_{//}$ along the radius direction, the more uniform the film thickness and the longer the target life. $B_{//}$ were measured by a Gauss meter. Two $B_{//}$ distribution curves are plotted for $B_{//}$ above the gun at 1 mm and 4 mm, respectively. The thickness distribution of Zn_2SiO_4 thin film for target-substrate (T-S) distance is also measured. As shown in Fig. 5.2.2-2, $B_{//}$ attenuates quickly above the gun surface. Therefore, the thicker the target, the lower the thin film deposition speed at a given power.

The decrease of $D_{T\text{-}S} \cdot P_s$ causes a decrease of thickness uniformity. The larger the $D_{T\text{-}S}$, the more uniform and the thinner the films. An approximate relation between the pressure P and mean free path λ_{mfp} of ambient air is given by λ_{mfp} (cm) = 5×10^{-3}/P (Torr) [Milton, 1992]. For ordinary sputtering pressure of 1×10^{-2} Torr, the λ_{mfp} of a toms sputtered out of the target is about ≈50 cm while under the pressure of 1×10^{-3} Torr, λ_{mfp} ≈ 5 cm. If the $D_{T\text{-}S}$ is 50 mm, particles sputtered out will experience 50 scattering events before reaching substrates under the sputtering pressure of 1×10^{-2} Torr. This is the explanation of the increase of uniformity of thin films by increasing pressure.

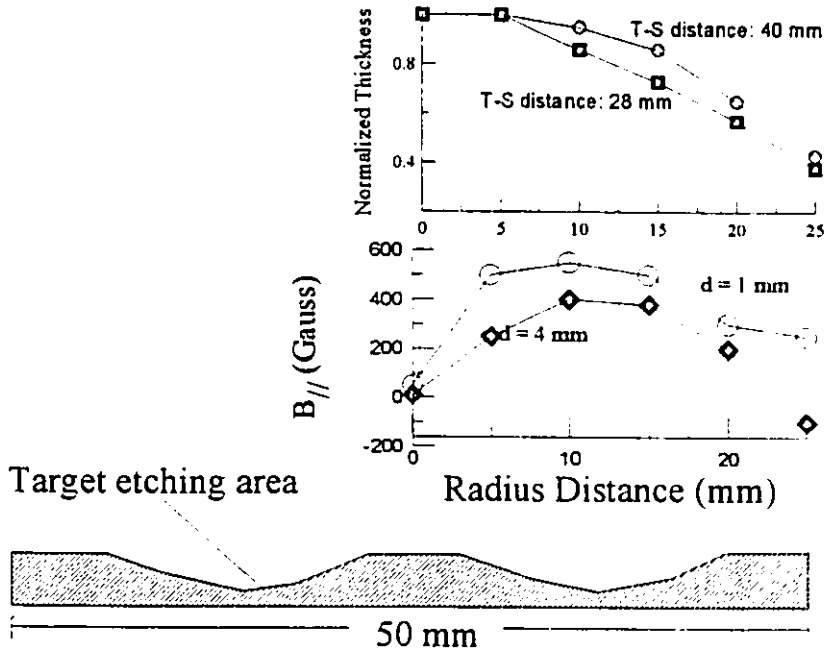

Fig. 5.2.2-1 The target etching and thin film thickness distribution dependence on the parallel component of the magnetic field $B_{//}$ of the US-GUN.

The manual of US' GUN II reported that the deposition rate of thin films is approximately proportional to the inverse of the square of the distance as in the case of evaporation. However, for ITO transparent conductive thin films, the fitting curve of Fig. 5.2.2-3 shows a relation of a inverse power of 3.7167. For other materials, the distance dependence of deposition rate should be different due to the different sputtering angular distributions.

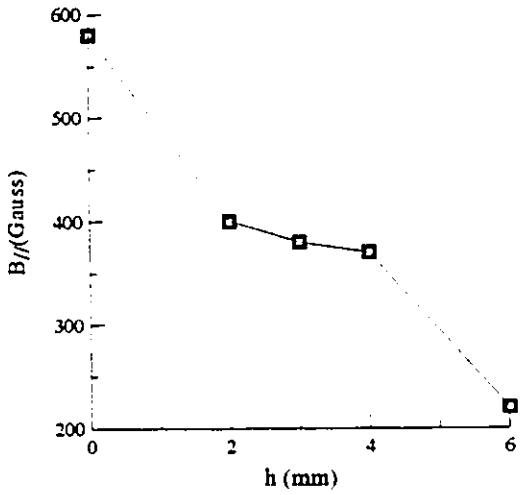

Fig. 5.2.2-2 Attenuation of $B_{//}$ above the US-GUN. $B_{//}$ was measured at the radius r = 15 mm.

The powder target we used has a surface area (assuming spherical grain) exposed under the plasma more than 1.5 times ($4r^2/\pi r^2$) larger than the flat surface. Any deviation from a flat target surface must give rise to changes in yield and angular distribution of sputtered particles, irrespective of structure type and orientation. The yield Y increases due oblique incidence [Behrisch, 1991].

$$Y(\theta_i) = Y(0) \cos^{-V_i}(\theta_i), \qquad \text{for } 0 \le \theta_i \le 70°, \quad 1/2 \le V_i \le 3 \qquad (5.2.2\text{-}1)$$

where V_i is a distribution parameter. $V_i < 1$ is the "under cosin" distribution which results from the shallow cascades due to low-energy (≤ 1 keV) projectiles and $V_i > 1$ is the "over-cosin" distribution due to atoms sputtered by backscattered projectiles.

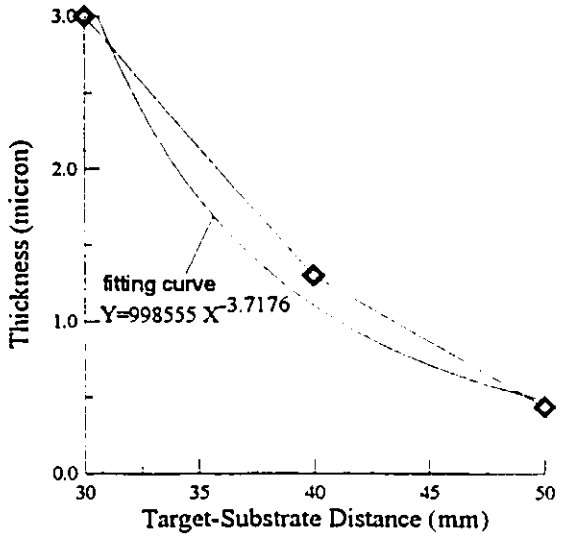

Fig. 5.2.2-3 ITO thin film thickness vs target-substrate distance, thin films were deposited in Ar (20 mTorr), at a r.f. power of 150 W for 30 minutes.

5.3 COMPOSITION AND STRUCTURE OF THIN FILMS

5.3.1 Rutherford Backscattering

Fig. 5.3.1-1 shows a typical RBS-spectrum of a sample taken with a 7.03 MeV ^{15}N beam. In order to get a good mass resolution between Y and Ce, ^{15}N was chosen as the projectile. The sample is a thin layer (~2000Å) of 3% mole doped $Y_2O_3(SiO_2)_2$ deposited on the graphite. Graphite is used because its mass is lower than N and therefore there is less interference from backscattering of the substrate. The backscattering spectrum taken under

a 165° scattering geometry allows the determination of Si:Y ratio. The spectrum shows three peaks due to Si, Y and Ce, while the O peak is not visible because of the electronic noise in the detector system. After subtracting the background, the ratio of Si:Y is calculated from the peak integrals to be 1:0.88. This is equivalent to a (Y_2O_3):(SiO_2) ratio of 1:2.2, which is close to $Y_2O_3(SiO_2)_2$. The Ce dopant quantity was measured to be 2% molar fraction.

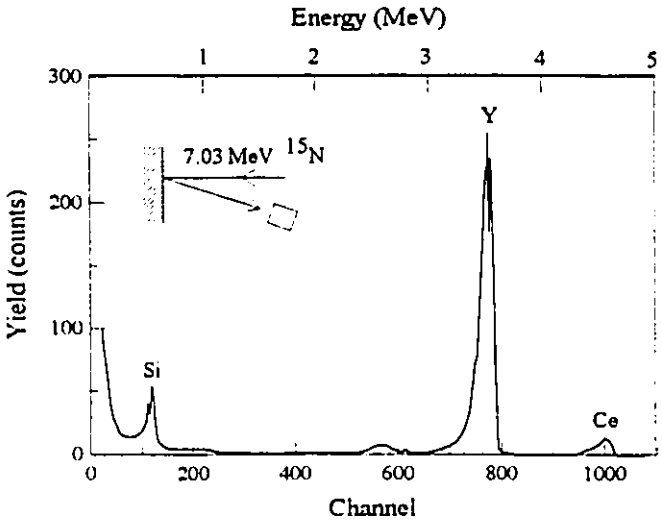

Fig. 5.3.1-1 RBS-spectrum of 3% mol. Ce^{3+}-doped $Y_2O_3(SiO_2)_2$ taken with a 7.03 MeV ^{15}N beam. The spectrum shows the peaks due to Si, Y and Ce.

Using RBS, we measured the relationship between the target and the thin film deposited. The results are shown in Table 5.3.1-1. All thin films for RBS measurement were deposited on graphite substrates.

Table 5.3.1-1 Compositions of thin films vs powder targets:

Composition of powder target	*Composition of thin films*
$Y_2O_3 : SiO_2 = 1 : 2$	$Y_2O_3 : SiO_2 = 1 : 1.3$
$Y_2O_3 : SiO_2 = 1 : 3$; 5% Ce	$Y_2O_3 : SiO_2 = 1 : 1.8$; 2% Ce**
$Y_2O_3 : SiO_2 = 1 : 2.5$	$Y_2O_3 : SiO_2$ 2 : 3*
$ZnO : SiO_2 = 2 : 1$; 3% Ce	$ZnO : SiO_2 = 1.3 : 1$; 2% Ce**

* Measured by X-ray diffraction, ** In molar fraction, measurement error: ± 20%.

5.3.2 Crystal Structure of Thin Films

The phase of thin films was measured using X-ray diffraction. All yttrium silicates and zinc silicates deposited at substrate temperatures below 400°C were found to be amorphous. Crystallization does not begin until 900°C for yttrium silicates and 850°C for zinc silicates.

Using a powder target of $Y_2O_3(SiO_2)_2$, Si substrates, and the sputtering conditions in Table 4.2-1, we discovered that the as-deposited thin films are amorphous at substrate temperature T_s = 400°C and show a preferred <122> orientation of Y_2SiO_5 at T_s=450°C. The crystallization at this temperature is assisted by the high kinetic energy of sputtered atoms. After annealing thin films at 1000°C for 2 hours in air, a new phase is observed with a hexagonal $Y_{4.67}(SiO_4)_3O$ structure. The large deviation of the thin film composition from that of the substrate material is due to the high sticking coefficient of the heavier Y atoms on the substrate as compared with that of Si atoms. Fig. 5.3.2-1 is the X-ray diffraction pattern of the above results. The surface morphology by scanning electron microscopy is shown in Fig. 5.3.2-2.

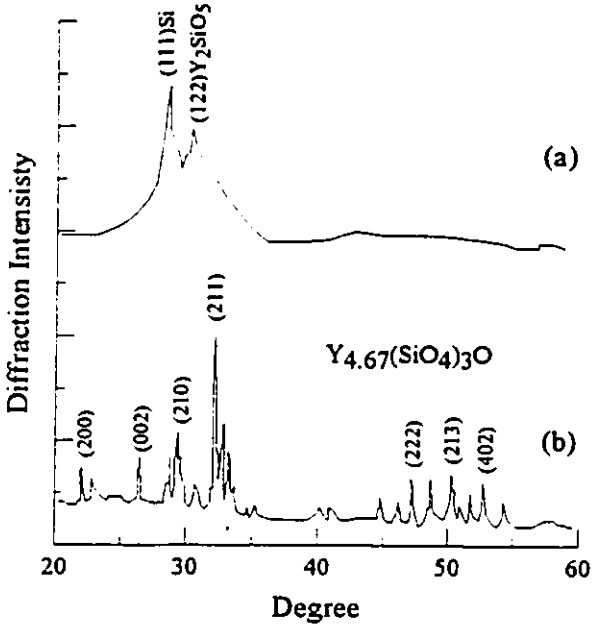

Fig. 5.3.2-1 X-ray diffraction patterns of the as-deposited $Y_{4.67}(SiO_4)_3O$ thin film on Si at the substrate temperature of 450°C (a) and the thin film after post-annealing ot 1000°C for 2 hours (b). Phase transformation took place from partially crystallized Y_2SiO_5 phase to well crystallized $Y_{4.67}(SiO_4)_3O$ after annealing.

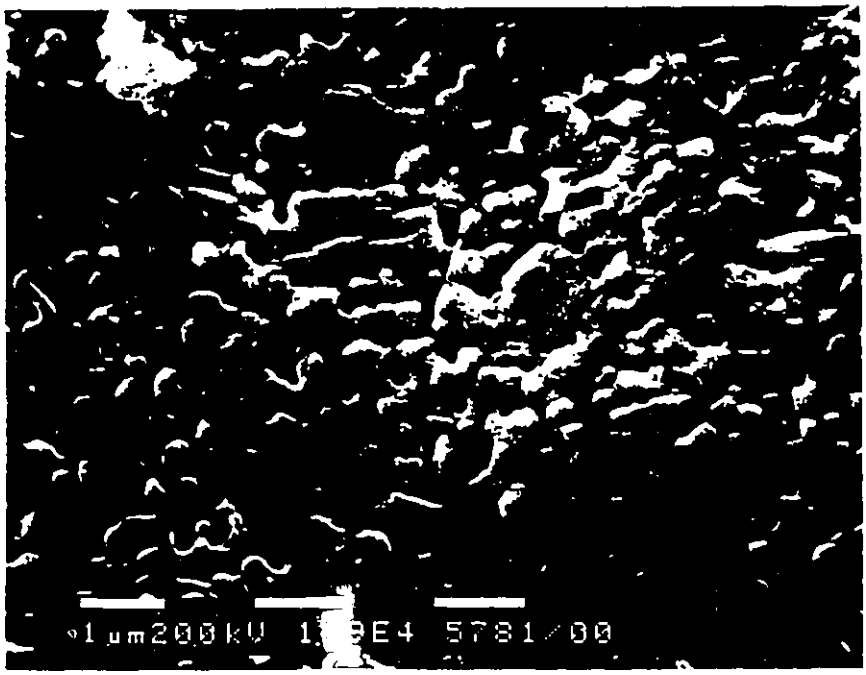

Fig. 5.3.2-2 Surface morphology of the post annealed thin film in Fig. 6.1.2-1 (b).

Thin films with Y_2SiO_5 and $Y_2Si_2O_7$ phase were prepared but repetition of the same phase is difficult even using the same target, sputtering conditions and post-annealing temperature. The reason is that the final phase of the thin film may be dominated by the less uniform composition distribution in different substrate positions and the complicated mechanism of the phase competition during the growth and annealing of thin films. However, our CL experimental results in section 5.2 will show that for RE-doped phosphors, the phase difference is not as important in influencing the brightness and spectra of luminescence.

Another way to investigate the crystallization of phosphors is to measure their photoluminescence since the photoluminescent intensity increases as the crystallization of phosphor improves. Using a semiconductor pulse-annealing equipment, Zn_2SiO_4:Mn thin films on (111)Si samples were annealed at 750°C-900°C for 1-2.5 minutes. Photoluminescence intensities of samples were measured by using a mercury lamp. The luminosity intensity results are summarized in Table 5.3.2-1. The results tell us that 900°C is crystallization of Zn_2SiO_4 thin film. The results agree with that of X-ray diffraction. Table 5.3.2-1 also tells us that the time needed for the phase transformation of Zn_2SiO_4 is a few minutes.

Table 5.3.2-1 Photoluminescence of Zn_2SiO_4:Mn thin films vs. annealing temperature and annealing time.

PL Brightness	Annealing Temp. (°)	Annealing Time (min.)
0	750	3
1.2	800	2
3.2	900	1
3.4	900	2

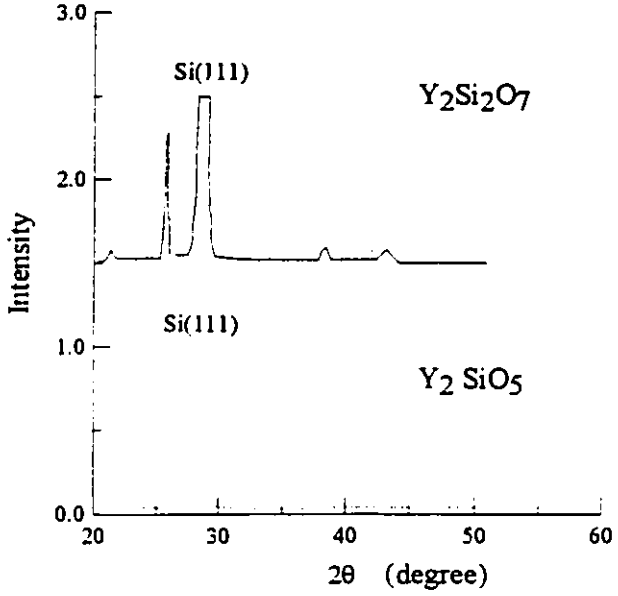

Fig. 5.3.2-3 X-ray diffraction pattern of Y_2SiO_5 and $Y_2Si_2O_7$.

5.3.3 Band Gap and Ultraviolet Absorbance Measurement

The absorbance of Zn_2SiO_4 and Y_2SiO_5 thin films are shown in Fig. 5.3.4-1. It was noticed that the band-gap of Zn_2SiO_4 thin film is 5.78 eV while that of Y_2SiO_5 is greater than 6.47 eV. The measurement is limited by the light source of the mercury lamp below 190 nm (6.47 eV). In this figure, it was noticed that Zn_2SiO_4 has a tail in the forbidden gap extending to 4.8 eV and it may have electrical properties similar to those of semiconductors. This suggests why Zn_2SiO_4 is a better host lattice than Y_2SiO_5. The details will be explained later in section 6.4.5.

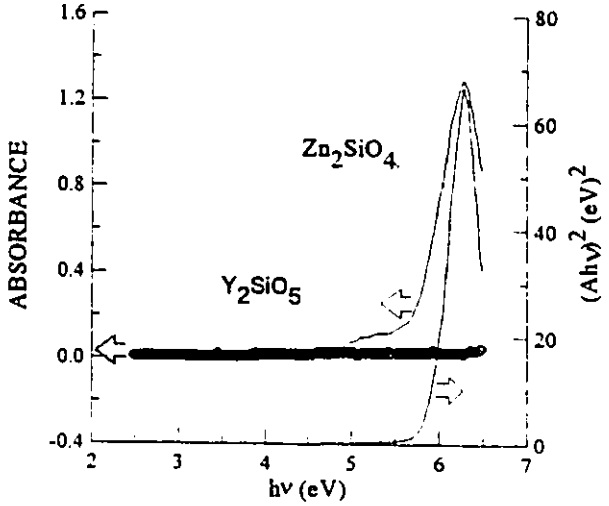

Fig. 5.3.3-1 Absorbance vs wavelength for Y_2SiO_5 thin film (1 μm) and Zn_2SiO_4 thin film (1 μm) which is drawn in terms of both absorbance (A) and $(Ahν)^2$.

5.4 SUMMARY

The chemical composition of sputtered thin films are mainly controlled by target material and deposition conditions such as the kind of sputtering gas, the position of substrate relative to the target and the substrate bias voltage. The composition relationship between target and thin film deposited were studied by RBS. We deposited oxide silicate thin films by using pure argon and floating substrate potential and then post annealing thin films in air at a temperature of 850°C for Zn_2SiO_4:Mn and 900°C for RE-doped yttrium silicates. These thin film phosphors show repeatable physical and electro-optical properties.

Planar magnetron sputtering has a deposition speed 3 to 5 times greater than that of conventional planar sputtering due to the trapping of electrons above the target surface and to the enhancement of plasma density. However, film thickness is less uniform due to the

unevenness of the parallel distribution of the magnetic field. Thin film distribution along the axial direction and the dependence of deposition rate upon rf power and target-substrate distance are studied for US GUN-II.

CHAPTER 6

RESULTS AND DISCUSSION - CATHODOLUMINESCENCE OF THIN FILM PHOSPHORS

In this section, we report the CL properties of both powder and thin film phosphors. The purpose of studying the CL properties of powder phosphors is to find the best composition of the target materials and the quantity of RE dopants suitable for RGB displays. CL intensity, CL spectra and CIE color coordinates are the three major criteria of a good phosphor. Using an electron beam (1-5 kV) as the probe, we studied phosphor spectra, luminescent intensity vs electron energy, CIE color coordinates of different dopants and host lattice, and the photon output efficiency (coupling coefficients of thin film phosphor).

6.1 POWDER PHOSPHORS

6.1-1 CL Intensity

Fig. 6.1.1-1 is the photopic intensity of cathodoluminescence vs accelerating voltage for $Y_2Si_2O_7$ ($Y_2O_32SiO_2$) phosphors doped by various rare earth dopants and sintered in 1200°C for 20 hours. It is noticed that the Eu^{3+} (red), Tb^{3+} (green) are the most efficient dopants. Under the excitation of 4 kV electron, the brightness ratio of Tb^{3+}-doped $Y_2O_32SiO_2$ to Sylvania 523 is 10 : 1. Sintering temperature will influence CL intensity.

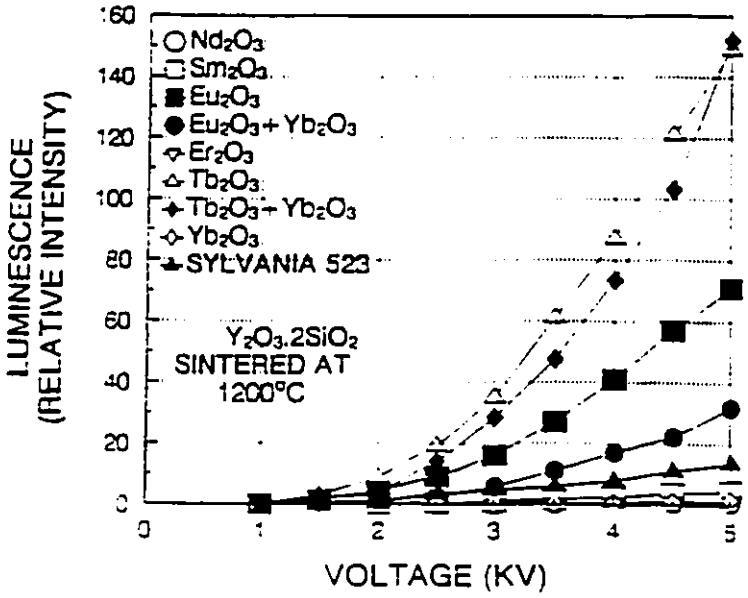

Fig. 6.1.1-1 CL intensity vs. electron beam voltage for RE^{3+}-doped $Y_2O_3 2SiO_2$ powder phosphors sintered at 1200°C for 20 hours. The quantity of dopants indicated are molar fraction.

In Fig. 6.1.1-2, samples were sintered at 800°C for 20 hours, under the excitation of 4 kV electron beam, the brightness ratio of Tb^{3+}-doped $Y_2O_3 2SiO_2$ to Sylvania 523 is decreased to 2.7:1. The intensity decrease is due to the crystallization of phosphors which need strong, unsymmetrical ligand fields for active centers.

CL intensity not only depends on accelerating electron voltage but also on the beam current of electrons and it is difficult to keep the same beam current for every measurement. However, for each measurement, the same current is maintained and up to 20 samples are measured in the chamber. In order to compare the brightness for another measurement, a standard, Sylvania phosphor 523, was used.

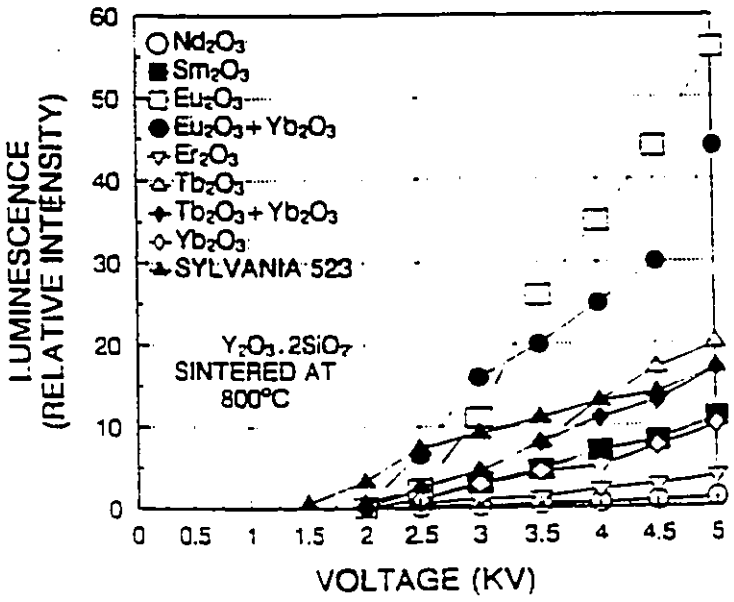

Fig. 6.1.1-2 CL intensity vs. electron beam voltage for RE^{3+}-doped $Y_2O_3{\cdot}2SiO_2$ powder phosphors sintered at 800°C for 20 hours. The quantity of dopants indicated are molar fraction.

RE-doped Y_2O_3 is a better CL phosphor as compared with those of RE-doped yttrium silicates. The CL properties for different dopants are shown in Fig. 6.1.1-3. It is observed that under 4 kV electron beam, the CL brightness ratio of Eu^{3+}-doped Y_2O_3 to Sylvania 523 is 10 : 1 while Tb^{3+}-doped Y_2O_3 is 3:1. In comparison with $Y_2O_3{\cdot}2SiO_2$, the brightness ratio of Eu^{3+}-doped and Tb^{3+}-doped phosphors are 4 : 1 and 10 : 1 respectively.

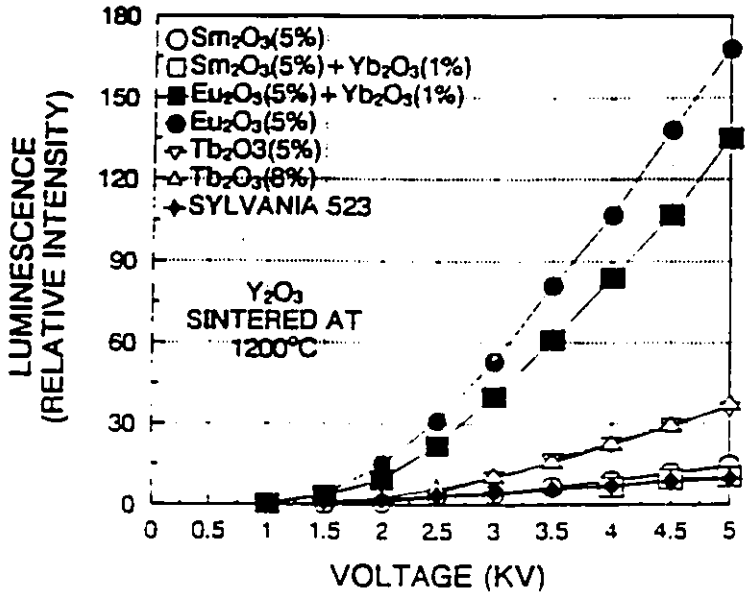

Fig. 6.1.1-3 CL intensity vs. electron beam voltage for RE^{3+}-doped Y_2O_3 powder phosphors sintered at 1200°C for 20 hours. The quantity of dopants indicated are molar fraction.

In $Y_2Si_2O_7$, the CL brightness vs. Tb^{3+} dopant quantity is shown in Fig. 6.1.1-4. In comparison with Fig.6.1.1-5 for Er^{3+}-doped Y_2O_3, it is concluded that up to 10% molar fraction of ER^{3+} can be doped into yttrium silicates without introducing serious luminescent quenching.

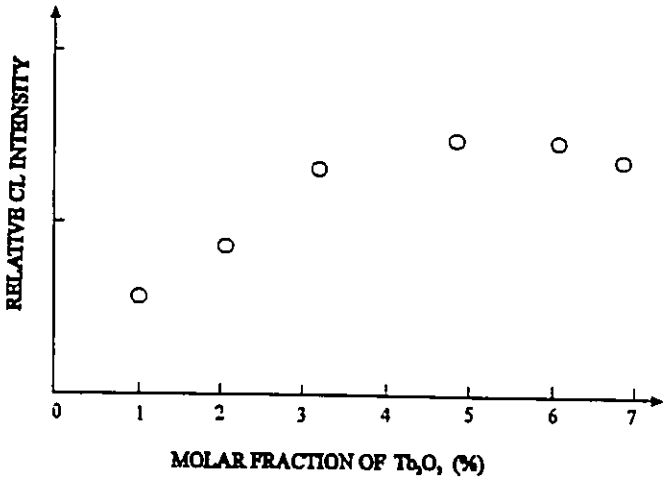

Fig. 6.1.1-4 CL intensity vs dopant quantity for Tb^{3+} activated $Y_2O_3{\cdot}2SiO_2$.

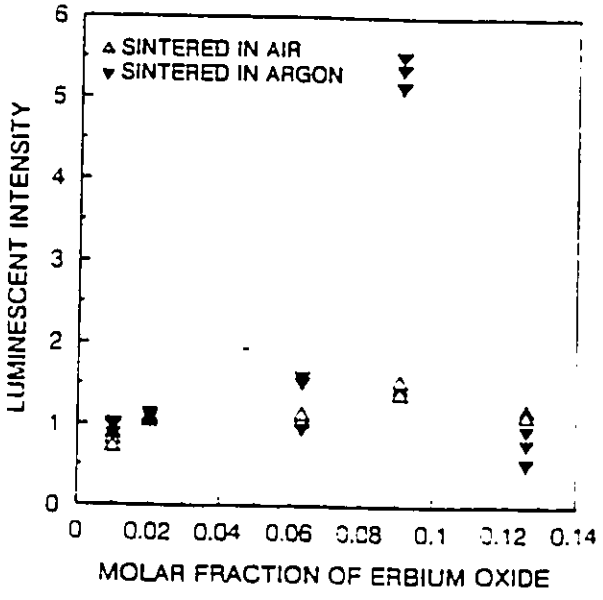

Fig. 6.1.1-5 CL intensity vs dopant quantity for Er^{3+} activated Y_2O_3.

6.1.2 CL Spectra

Cathodoluminescent spectra of RE^{3+}-doped Y_2O_3, $Y_2O_3 \cdot 2SiO_2$ and $ZnO \cdot Y_2O_3 \cdot 2SiO_2$ are shown in Fig. 6.1.2-1. The compound $ZnY_2Si_2O_8$ was suggested [Born, 1985] but never synthesized. X-rays show that two phases of Zn_2SiO_4 and Y_2SiO_5 coexist. RE^{3+} dopants will substitute in the Y position in 8-folded oxygen octahedral vacancies due to their large atomic sizes and same charge state. It is interesting to see that little change of luminescent intensity and major peak position was observed for Tb^{3+} and Eu^{3+}-doped samples as compared with silicates. Therefore ZnO is not a killer to the luminescence.

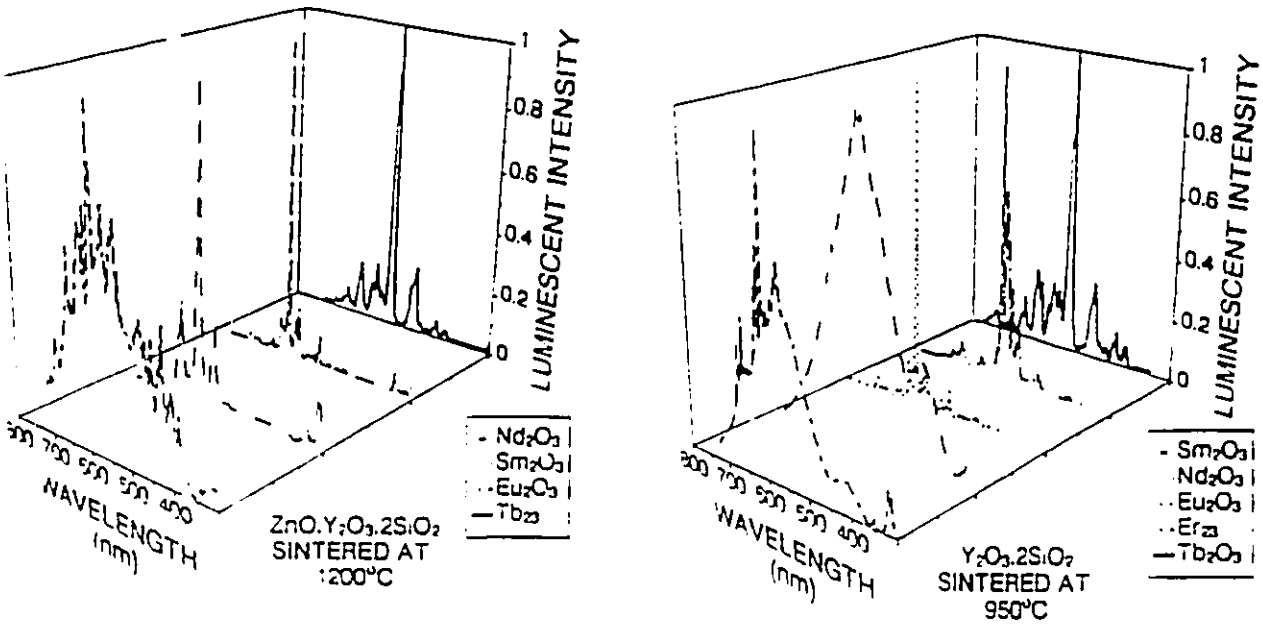

Fig. 6.1.2-1 CL spectra of RE^{3+}-doped Y_2O_3, $Y_2O_3 \cdot 2SiO_2$ and $ZnO \cdot Y_2O_3 \cdot 2SiO_2$

The tristimulus values of some RE^{3+}-doped phosphors are shown in Fig. 6.1.2-2 and Table 6.1.2-1. It can be seen that most RE^{3+}-doped phosphors have high excitation purity.

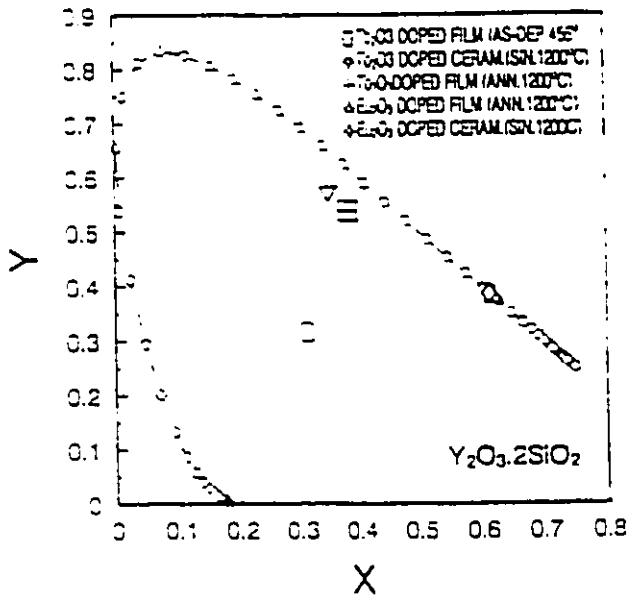

Fig. 6.1.2-2 Color coordinates of RE^{3+}-doped yttrium silicates.

Table 6.1.2-1 Chromaticity coordinates of RE^{3+}-doped $Y_2Si_2O_7$.

Dopants	x	y	DW (nm)	EP (%)
Ce^{3+}	0.2508	0.22.7	462	34
Eu^{3+}	0.6636	0.3362	608	98
Tb^{3+}	0.3813	0.5366	564	79
Er^{3+}	0.3337	0.6564	554	98

Notes: DW: dominant wavelength; EP: excitation purity.

The major luminescent peaks of RE^{3+} activated $Y_2Si_2O_7$ and Y_2O_3 we measured are shown in Table 6.1.2-2. The results are compared with those from other lattices [Ozawa, 1990] It can be observed that when crystal environment changes, some minor peaks become major peaks but the position for each peak shifts very little. Because the luminescence of Pr^{3+}, Dy^{3+} Ho^{3+} and Tm^{3+} activated $Y_2Si_2O_7$ phosphors are too weak to take the spectra, their data are not listed. The above results told us that the characteristic luminescent spectra of RE^{3+}-doped phosphors are very good candidates for color display.

Table 6.1.2-2 Major peaks of RE^{3+} in different hosts.

ER^{3+}	Major Peaks (nm)					Transition(s)
	$Y_2Si_2O_7$	Y_2O_3	Y_2O_2S	La_2O_3	Gd_2O_3	
Tb^{3+}	540	543	417	543	542	$^5D_4 \rightarrow {}^7F_6$
Eu^{3+}	613	611	611	626	611	$^5D_0 \rightarrow {}^7F_2$
Ce^{3+}	420, 622	413, 567				5d→6f
Pr^{3+}		630	606	509	630	$^3P_0 \rightarrow {}^3H_6$, $^3P_0 \rightarrow {}^3F_2$
Sm^{3+}	609	608	603	601, 654	607	$^4G_{5/2} \rightarrow {}^6H_{7/2}$
Er^{3+}	549	563	563	549	563	$^4S_{3/2} \rightarrow {}^4I_{15/2}$
Dy^{3+}		572	572	572	572	$^7F_{9/2} \rightarrow {}^6H_{13/2}$
Ho^{3+}		550	544	544	550	$^7F_4 \rightarrow {}^5I_8$, $^5S_2 \rightarrow {}^7I_8$
Tm^{3+}		453		457	453	$^1D_2 \rightarrow {}^3F_4$

6.2 CATHODOLUMINESCENCE OF THIN FILMS

Using the target materials and the sputtering conditions described in Chapter 4, we deposited Eu^{3+}, Tb^{3+}, and Ce^{3+}-doped $Y_2O_3(SiO_2)_2$ thin films with a ratio of photopic luminosity intensity of 1 : 2.2 : 10 for red, green and blue respectively. Fig. 6.2-1 shows the

spectra of the above films. Curves are normalized. One important thing to mention is that the major emission peaks due to the transition of $^5D_0$ - $^7F_2$ in Eu^{3+} and to the transition of $^5D_4$ - $^7F_6$ in Tb^{3+} are less influenced by the host lattice and the good crystallinity of thin films only increases the luminescent intensity and not the position of the peaks. The electron configurations of Ce^{3+}, Tb^{3+} and Eu^{3+} are $4f^1$, $4f^8$ and $4f^6$, respectively, followed by the outside $5p^6$, 6s and 5d electrons which shield inner f electrons. Therefore, it is not strange that the 4f - 5d electron transition in Ce^{3+} is more sensitive to the host lattice than that of Tb^{3+} and Eu^{3+}. Because the thin films prepared were polycrystalline, luminescent peaks were broadened, and the Stark splitting of the transition is not clear enough to be observed as with single crystal materials.

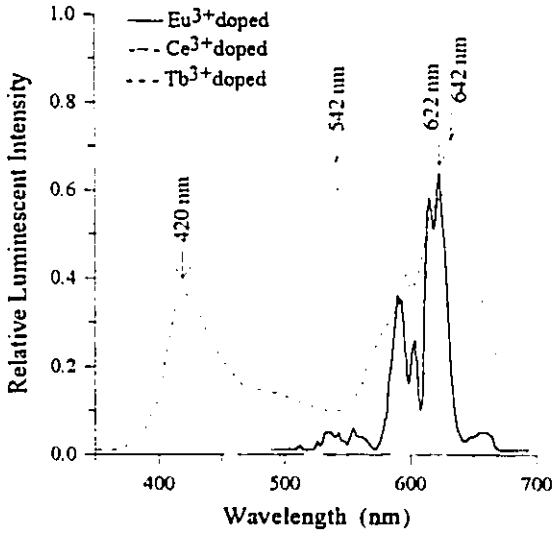

Fig. 6.2-1 Cathodoluminescent spectra of Eu^{3+}, Tb^{3+} and Ce^{3+}-doped $Y_2Si_2O_7$. The Tb^{3+} spectrum is also that of $Y_{4.67}(SiO_4)_3O:Tb^{3+}$.

Tb^{3+}-doped spectra are exactly the same no matter whether the host lattice is Y_2SiO_5, $Y_2Si_2O_7$ or $Y_{4.67}(SiO_4)_3O$. The relative intensities are within ±50% of each other, within the experimental uncertainties of doping densities and individual sample performance. Intensities were calibrated relative to powder material, which was placed in the cathodoluminescent measurement chamber along with thin films. The relative brightness of thin films compared to that of powder is 10-30%. This is explained by waveguiding losses and absorption in the silicon substrate. The cathodoluminescent intensity of a powder target containing Ce^{3+} is 50% of commercial P47 (Sylvania) performance. The CL intensity ratio of Sylvania 523 to P47 is 1:3.

The output coupling efficiency η_{opt} of photons is explained in Fig. 6.2-2 where a simple film/substrate structure is drawn. η_{out} is defined by the following equation:

$$\eta_{out} = \frac{\text{photons emitted through the surface } (cm^{-2})}{\text{photons generated } (cm^{-3})} \qquad (6.2\text{-}1)$$

Three factors must be considered. The first is the absorption loss η_{abs} depending on the thickness and the absorbance of the film. The transparency of yttrium silicates with a thickness about 1 μm is greater than 96% in the wavelength range of 200-800 nm measured by ultraviolet spectra. The absorption loss is negligibly small as compared with the following two factors. The second factor is the Frensnel loss η_{Fr} which occurs when light passes from a media whose index of refraction n_1 (phosphor) to a media whose index of refraction is n_2 (air). The well-known formula for the reflection coefficient is

$$R = [(n_2-n_1)/(n_2+n_1)]^2 \qquad (6.2\text{-}2)$$

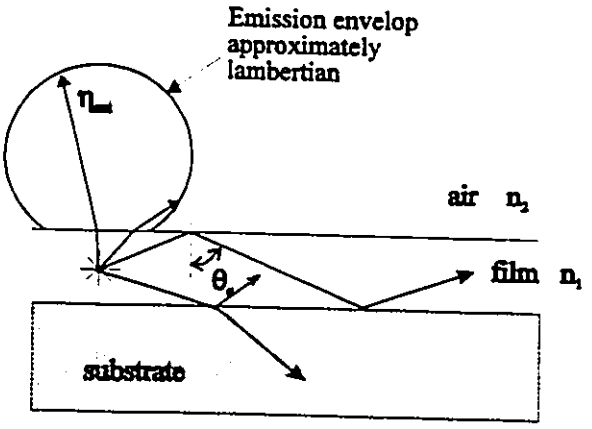

Fig. 6.2-2 Diagram of output coupling.

and the transmission coefficient T is

$$T = 1-R = 4n_1n_2/(n_2^2+2n_1n_2+n_1^2) = 4/(2+n_2/n_1+n_1/n_2) \quad (6.2\text{-}3)$$

Fresnel loss efficiency factor is defined as

$$\eta_{Fr} = 4/(2+n_2/n_1 + n_1/n_2) \quad (6.2\text{-}4)$$

The third and the most important loss is waveguiding loss due to the internal reflection (Snell's law) for those rays whose incident angles are greater than the critical angle θ_c. The related efficiency is determined by

$$\eta_{int} = (n_2/n_1)^2 \quad (6.2\text{-}5)$$

Therefore, the coupling efficiency is

$$\eta_{out} = \eta_{abs}\,\eta_{Fr}\,\eta_{int} \quad (6.2\text{-}6)$$

The coupling efficiency of $Y_2Si_2O_7$ and Zn_2SiO_4 thin films are shown in Table 6.2-1. Because the substrates we used were Si which strongly absorb the incident light, therefore, the measured output coupling coefficients are only half of that obtained by calculation.

Table 6.2-1 Calculated coupling coefficients of silicate thin films:

$Y_2Si_2O_7$	Zn_2SiO_4
n =1.74*	n = 1.72
η_{abs} = 96%	η_{abs} = 84%
η_{Fr} = 93%	η_{Fr} = 93%
η_{int} = 33%	η_{int} = 33.8%
η_{out} = 29.5%	η_{out} = 26.4%

* [Toropov, 1961]

From Fig. 6.2-3, it is noticed Ce^{3+}-doped films have two broad-band peaks. One is located in the blue region at 420 nm (deep blue) and the other in the deep red region (622 nm) due to the ground state splitting ($^2F_{5/2}$, $^2F_{7/2}$), and the transition of 5d → 4f. The 622 nm peak of Ce^{3+} was only discovered in a few host lattices such as in $(Y,Ce)_3Al_5O_{12}$ [Blasse, 1967]. The possible reasons for such an emission are: (a) the crystal field is so strong that the 5d level is split; and (b) the center of the 5d level is at relatively low energy. The increase of annealing temperature from 880°C to 1000°C not only gives a narrower blue emission peak and a lower ratio of blue to red intensity but also causes a shift of peak position from 451 nm to 421 nm. The reason is that the higher annealing temperature of 1000°C gives better thin

film crystallization which increases both the ligand field and the splitting of the 5d - 4f transition.

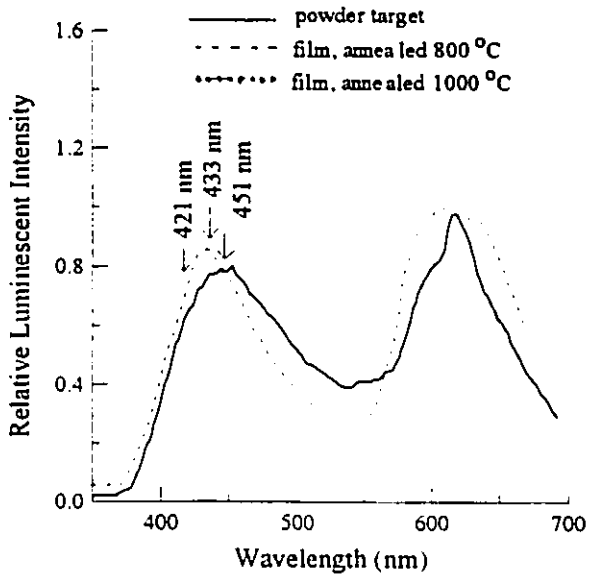

Fig. 6.2-3 Annealing effect of Ce^{3+} activated $Y_2Si_2O_7$.

The chromaticity coordinates in cathodoluminescence are shown in Fig. 6.2-4 where the red peak of the Ce^{3+}-doped thin film phosphor is filtered out. It can be seen that excitation purity of Tb^{3+} and Eu^{3+}-doped films more than 90%. The dominant wavelengths of Tb^{3+} and Eu^{3+}-doped $Y_2Si_2O_7$ are 610 nm and 538 nm respectively.

Fig. 6.2-5 shows the luminescent spectra of Eu^{3+}-doped thin films and the sintered target phosphor. It can be observed that not only are the major peaks due to ^5D_o - $^7F_2$

shifted, but they also split differently for as-deposited thin films. This can be explained by the change of the symmetry of the atomic sites of Eu^{3+}. Annealing increases the ligand field but changes the symmetry from lower ones to tetragonal or trigonal fields which cause splitting into two levels [Blasse, 1979]. The results show that the 4f electron transitions of Eu^{3+} are more easily perturbed by the host environment in agreement with the earlier report of Uitert who changed the lattice by substituting cation impurities to alter valence, atomic radius and the ionization potential of the host [Uitert, 1962].

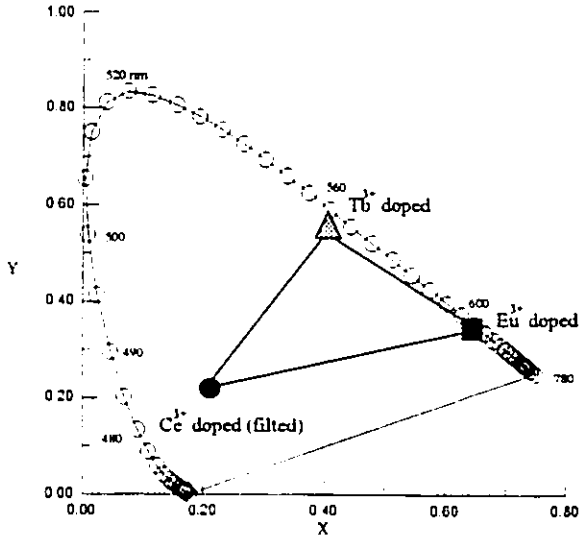

Fig. 6.2-4 Chromaticity coordinates of Eu^{3+}, Tb^{3+} and Ce^{3+}-doped $Y_2Si_2O_7$.

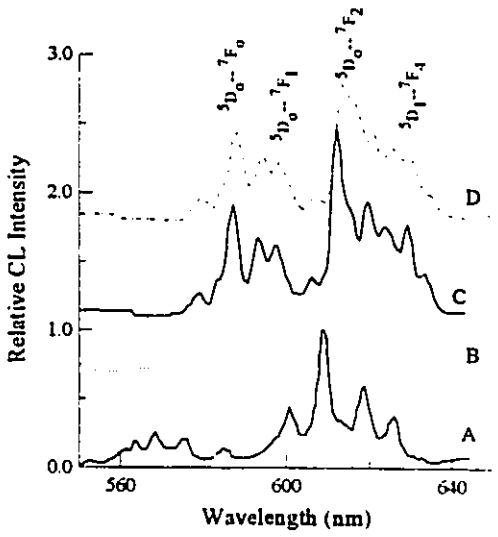

Fig. 6.2-5 Cathodoluminescence of Eu^{3+}-doped $Y_2Si_2O_7$ thin films and the sintered target materials in wide wavelength range (a) and the details between 550 nm and 650 nm (b). A is the as-deposited thin films at T_s = 450°C; B is $Y_2Si_2O_7$ powder phosphors sintered at 1200°C; C is the thin film annealed at 900°C for two hours; and D is the thin film annealed at 1000°C for two hours.

In the Y_2O_3-SiO_2 phase diagram, the region between Y_2O_3 : SiO_2 and $Y_2O_3.(SiO_2)_2$ is a mixed phase. The luminescent intensity shows no significant change when the ratio of Y_2O_3 : SiO_2 is between 1:1 and 1:2. We prepared powder samples of both Y_2SiO_5:Eu and Y_2SiO_7:Eu to test the influence of phase on the luminescence. As shown in Fig.6.2-6, there is a shift in the peaks indicating a modified crystal field. However, the luminescent intensities are not significantly different for the two samples. This is an indication that we can easily prepare good luminescent yttrium silicate thin films without strict stoichiometric control.

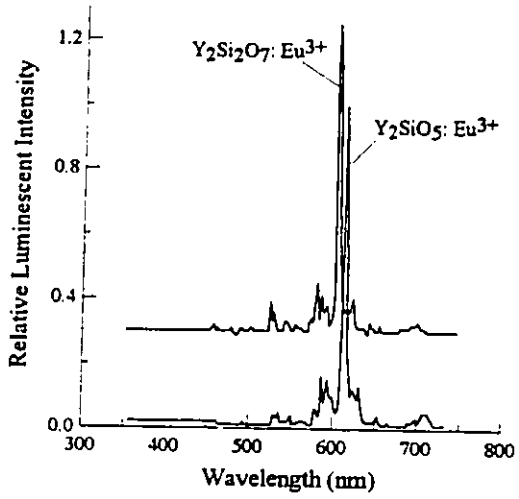

Fig. 6.2-6 Cathodoluminescence of Eu^{3+} activated Y_2SiO_5 and $Y_2Si_2O_7$ powder phosphors. The powers were prepared by sintering suitable Y_2O_3-SiO_2 mixed and pressed powders doped with 5% mole% Eu_2O_3 at 1200°C for 20 hours in air.

Another important phenomenon is that a rare earth activator is only influenced by the ligand field of the nearest neighbors. Fig. 6.2-7 is the CL spectra of Tb^{3+} activated $Y_2Si_2O_7$. The post-annealed thin films have the same spectrum as that of as-deposited amorphous thin film at a substrate temperature of 300°C. This result tells us that even the short-range-ordered ligand field is strong enough to split the 4f electron orbits. This is guidance for theoretical calculation of RE transitions. Only the nearest and the next nearest neighbors need to be considered.

Fig. 6.2-8 is the CL spectra of Mn activated Zn_2SiO_4 thin films annealed at different temperatures. High temperature annealing gives not only better crystallization but also stronger CL intensities and the spectra peak shift to the lower wavelength side.

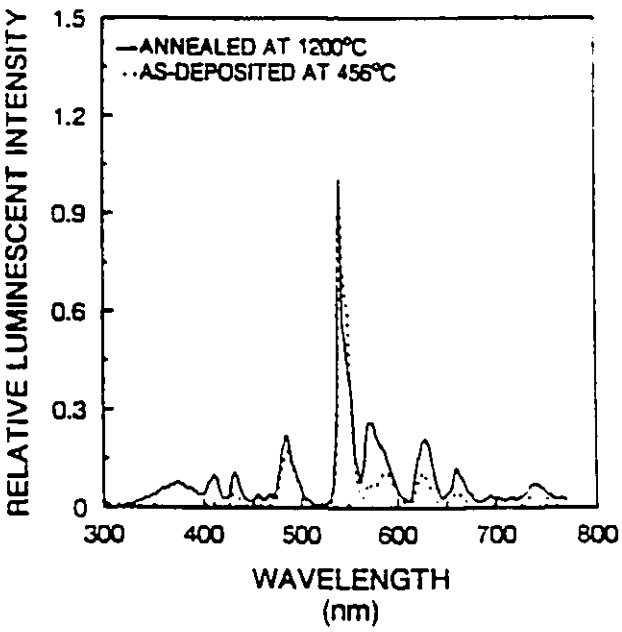

Fig. 6.2-7 Ligand field effect of the Tb^{3+} activated $Y_2Si_2O_7$ spectra.

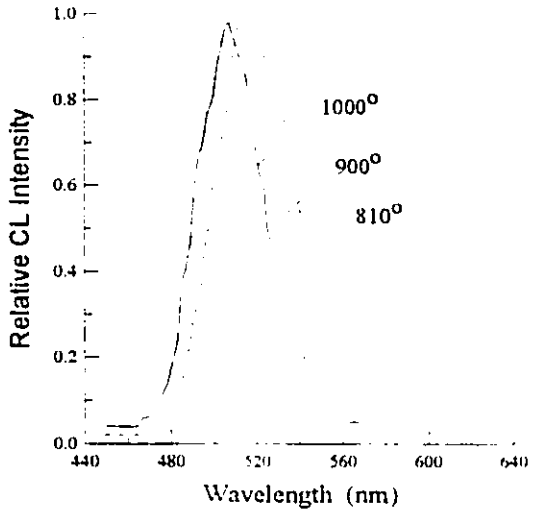

Fig. 6.2-8 Annealing effect of Mn activated Zn_2SiO_4 thin films.

6.3 SUMMARY

In conclusion, good RE^{3+}-doped silicates thin films are needed to be post-annealed to above 900°C for good CL performance compatible with their powder counterparts. Eu^{3+}, Tb^{3+} and Ce^{3+} are the best dopants for RGB luminescence; Eu^{3+} and Tb^{3+} are less sensitive to the host lattice than Ce^{3+}. Only the nearest or next nearest neighbors of the active center supply the required ligand field for transitions.

The chromaticity coordinates and brightness of some RE^{3+}-doped $Y_2Si_2O_7$ thin film phosphors are compared with their powder counterparts as shown in Table 6.3-1. These films have high brightness and close chromaticities of red and green required by NTSC standards (Table 3.5-2) and are practical phosphors ready for use. However, the blue colour is still not satisfactory. The brightness ratio is uncertain due to the wave-guiding effect of thin films as described in section 6.2, depending on the annealing time and temperature, film surface roughness, substrate material and surface smoothness. A rough surface will scatter guided light and increase the brightness.

Table 6.3-1 Comparison of brightness and chromaticity coordinates (CIE 1931) of RE^{3+}-doped $Y_2Si_2O_7$ thin film and powder phosphors

Dopants	**Chromaticity coordinates**				**B_{film}/B_{powder}**
	x		**y**		
	Powder	***Thin film***	***Powder***	***Thin film***	
Ce^{3+}	0.25	0.26	0.237	0.24	0.07-0.23
Eu^{3+}	0.66	0.64	0.36	0.31	0.15-0.46
Tb^{3+}	0.38	0.38	0.54	0.54	0.18-0.37

Note: B_{film}/B_{powder} is the CL intensity ratio of thin film and powder phosphors measured using a 4 kV accelerated electron beam.

CHAPTER 7

ELECTROLUMINESCENCE OF $Zn_2SiO_4:Mn^{2+}$ AND $Y_2SiO_5:Ce^{3+}$ THIN FILM PHOSPHORS

7.1 INTRODUCTION

We studied the EL spectra and EL brightness excited under different drive frequencies and pulse widths, device lifetime, time resolved spectra and the transferred charge where the latter two reveal the electron processes in the devices. Using the above results, the efficiencies of devices were calculated. From our experimental results, we know that both Zn_2SiO_4 and Y_2SiO_5 are very good host materials for cathodoluminescence but only the former is better for electroluminescence. Since both of them are wide band insulators, why do they have such different properties? What is the mechanism of electroluminescence in oxide phosphors? How do EL properties of oxide phosphors differ from ZnS? We tried to answer such questions using the following experimental results.

The device structures we studied are:

Structure A: ITO/Zn_2SiO_4:Mn^{2+}(0.7 μm)/$BaTiO_3$(0.8 mm)/Al

Structure B: ITO/Zn_2SiO_4:Mn (1500Å)/Y_2SiO_5:Ce(500Å)/..../Zn_2SiO_4:Mn/$BaTiO_3$/Al

Structure C: ITO/ZnS(2000Å)/Zn_2SiO_4:Mn/ Y_2SiO_5:Ce(500Å)/....

/Zn_2SiO_4:Mn/$BaTiO_3$/Al.

Structure D: ITO/Zn_2SiO_4/ Y_2SiO_5:Ce(500Å)/..../Zn_2SiO_4/$BaTiO_3$/Al

Structure E: ITO/Y_2SiO_5:Mn^{2+}(2%)+Sm^{2+}(1%)/$BaTiO_3$/Al

where devices B and C are deposited on the same substrate and each of them has four layers of Zn_2SiO_4:Mn(2000Å) and three layers of Y_2SiO_5:Ce(500Å). The structure D has six layers of Y_2SiO_5:Ce(800Å) and 7 layers of Zn_2SiO_4. The phosphor layers were post-annealed at 950°C for 3 hours.

Why study the structure B, C, D and E? Our first hope is to increase the efficiency by injecting more hot electrons into the phosphor. The second aim is to find out if electrons inducing avalanche come from the insulator-phosphor interface.

As we know, one of the major requirements for a good phosphor in electro-luminescent application is that there should be less interaction between 'free carriers' and phonons so the electrons can be accelerated 'loss-free' or will have long mean-free-path. Müller calls such electrons 'hot electrons' since an electron at room temperature with an energy of 2.5 eV will have a thermal energy of 25,000K [Müller, 1993] and could excite the transitions of active centers to emit photons with wavelengths greater than 492 nm. If ZnS is a better loss-free host than Zn_2SiO_4, the threshold voltage will be decreased in devices C and D. We hope to use the alternating multi-layer structure to increase the EL efficiency of Y_2SiO_5:Ce^{3+} by the increase of 'hot electrons' from Zn_2SiO_4. Finally, Sm^{2+} was known as a co-activator of Ce^{3+} to increase the photoluminescent intensity [Meijerink, 1991] investigated in structure E.

7.2 EL SPECTRA

The EL spectra of Mn^{2+} activated Zn_2SiO_4 (green) and Ce^{3+} activated Y_2SiO_5 (blue) thin film EL devices are shown in Figs. 7.2-1 and 7.2-2, respectively. The EL spectra are compared with CL results in the same samples. It can be seen that for Zn_2SiO_4:Mn^{2+} and Y_2SiO_5:Ce^{3+}, EL and CL have the same results, while for Ce^{3+} and Sm^{3+} co-doped thin films, the results are different.

In Zn_2SiO_4: Mn^{2+} phosphor, luminescence is assigned to transitions between the spin-orbit components of $^4T_1$ excited state and $^6A_1$ ground state of Mn^{2+} in T_d coordination [Clogston, 1958], while in Y_2SiO_5:Ce^{3+}, the transition is due to 4f ground states to 5d band.

Rutherford backscattering shows a deviation in thin film composition ($ZnO:SiO_2$ = 1.3:1) from the target (Sylvania power phosphor: $ZnO:SiO_2$ = 2 : 1). X-ray diffraction shows that the crystallized phase is willemite Zn_2SiO_4, so the extra SiO_2 appears to exist as an amorphous phase.

From Fig. 7.2-2 (b), an energy transfer from Sm^{3+} to Ce^{3+} is observed in the CL spectrum but not in the EL spectrum. In Y_2SiO_5 : Ce, Ce^{3+} ions were observed as hole traps and Sm^{3+} ions as electron traps [Meijerink, 1991]. It is known that energy transfer happens only when two active centers come close. The difference between EL and CL may be explained as an electric field effect which may polarize 'molecules' and make the transfer between Ce^{3+} and Sm^{3+} difficult.

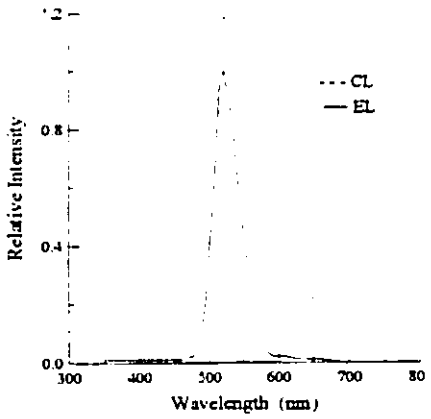

Fig. 7.2-1 EL and CL spectra of Zn_2SiO_4.

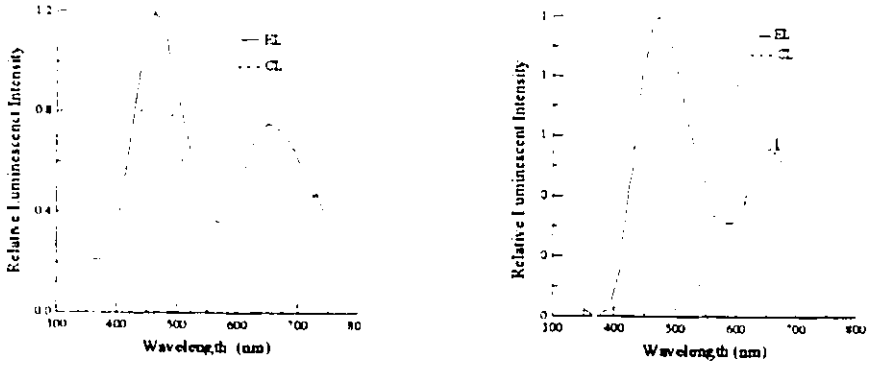

(a) (b)

Fig. 7.2-2 EL and CL spectra of $Y_2SiO_5:Ce^{3+}$ in device D (a) and $Y_2SiO_5:Ce^{3+}+Sm^{3+}$ in device E (b).

7.3 EL BRIGHTNESS AND AGING

Fig. 7.3-1 is the EL brightness vs applied voltage (peak to zero) at a frequency of 400 Hz and a pulse width to pulse period of 1/10. Device A has a threshold voltage of 200V (or a threshold field of 1 MV/cm) and excellent EL performance. Unlike the EL performance of $ZnS:Mn^{2+}$ which has an abrupt increase above the threshold voltage, the brightness of the $Zn_2SiO_4:Mn^{2+}$ device changes slowly until above 2 MV/cm. The slow increase indicates the limited avalanche electron process which is quite different from the abrupt avalanche in ZnS and in semiconductors. A linear increase of brightness was observed between 1.5 MV/cm and 3 MV/cm.

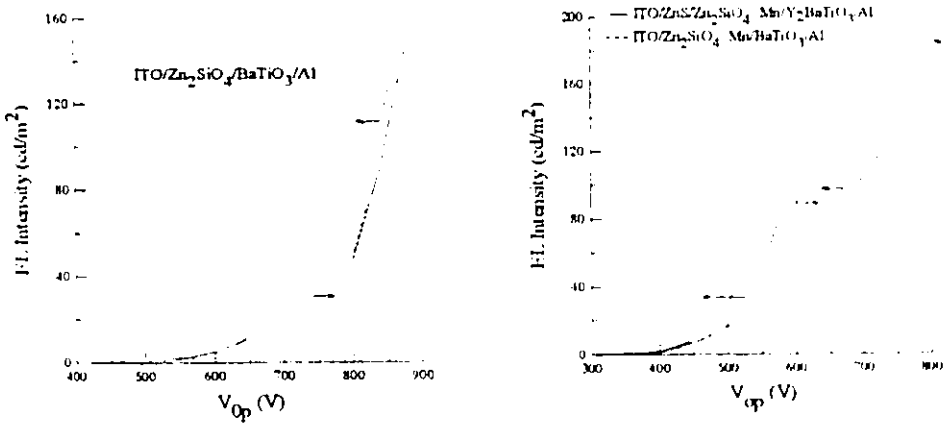

(a) (b)

Fig. 7.3-1 EL brightness vs driving voltage (zero to peak) for devices of structure A (a), B and C (b). Both rising and falling driving are shown.

In Fig. 7.3-1(b), with 2000A of ZnS above the device B on the same substrate, the threshold voltage decreases and a higher brightness is observed. The result is due to an increase in 'hot electrons' from the ZnS-Zn_2SiO_4 interface to excite Mn^{2+} centers in Zn_2SiO_4. The result is just as we expected. However, the device is easier to break down above 600 V_{op} due to the low dielectric strength of ZnS.

Another interesting phenomenon in Fig. 7.3-1 is the hysteresis effect which shows different brightness response curves for increase and decrease of applied voltage. All the devices show a memory effect except device C where at the same voltage, the rising curve has higher brightness than the falling curve.

The memory effect was also discovered in ZnS:Mn EL devices [Tannas, 1985] in which only under certain fabrication conditions and device structures the memory effect can take place, but in oxide phosphors, all the devices show hysteresis.

The hysteresis effect is difficult to explain in a detailed sense with the tunneling and impact excitation model we described earlier in Chapter 3. It may be due to band bending from space charge in the phosphor. The change in threshold voltage and initial stabilization effect may also be due to changes in interface states due to hot electron bombardment [Smith, 1981].

Fig. 7.3-2 is the aging of device A. No obvious luminescent intensity decrease was observed until the device worked for 280 hours. The intensity decrease is not due to the phosphor layer degradation but due to the humidity assisted plasma etching of ITO under the high field.

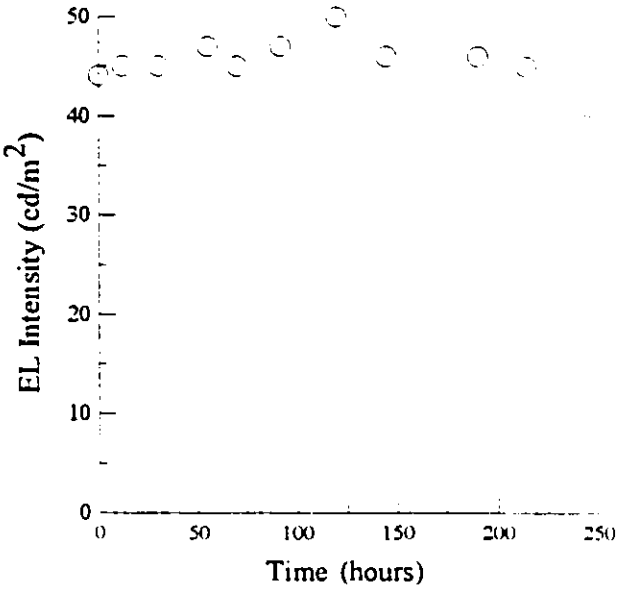

Fig. 7.3-2 Aging effect of ITO/Zn_2SiO_4:Mn/$BaTiO_3$/Al device in air atmosphere. The driving voltage is 400 V (zero to peak) with a frequency of 400 Hz and a narrow pulse width.

7.4 DRIVING FREQUENCY AND PULSE WIDTH

For phosphors with short decay time τ, the EL brightness has a linear relationship with frequency f. If the period of pulse applied ($1/f = b$) is less than τ, the brightness will become saturated even if you increase the frequency under a given voltage. Fig. 7.4-1 is the EL intensity dependence upon frequency and pulse width for device A. In (a), the brightness began to saturate when b was close to τ = 0.6 ms. In Fig. 7.4-1(b), it is noticed that increasing the driving pulse duty time causes the EL intensity to increase only somewhat.

In the tunneling model, the impact electrons are supposed to be injected from the phosphor-insulator interfaces. The moment a pulse greater than the threshold voltage V_{th} is applied to the device, electrons are injected into the phosphor and the avalanche begins to

take place. In a wide-band insulator, because the effective masses of electrons and holes are quite different, the space charge will build up very quickly, as the pulse width is increased, but the current is still limited by the space charge.

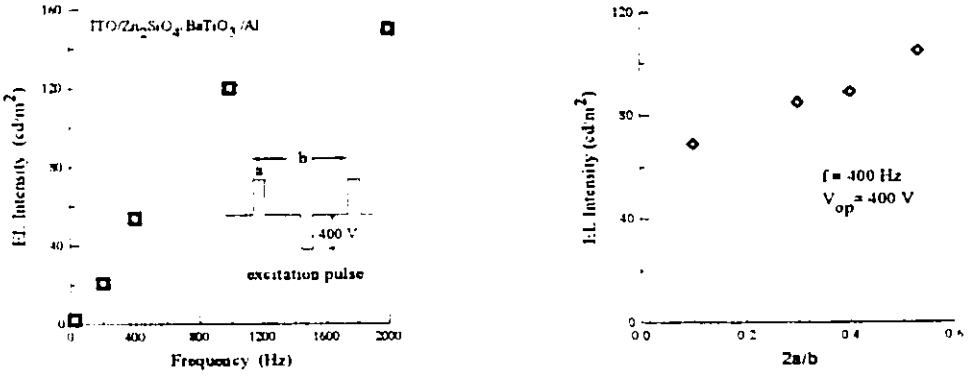

(a) (b)

Fig. 7.4-1 The EL intensity dependence on frequency (a) and on pulse width (b) where a is the pulse duty time and b is the period of the pulse.

7.5 DECAY TIME OF $Zn_2SiO_4:Mn^{2+}$ AND $Y_2SiO_5:Ce^{3+}$ THIN FILM PHOSPHORS

From the decay curves measured by using the set-up shown in Fig.4.6.3-1, not only can we measure the decay time of a phosphor but also understand the electron process in the devices. Figs. 7.5-1 to 7.5-3 show EL responses of different device structures with different voltages and pulse widths.

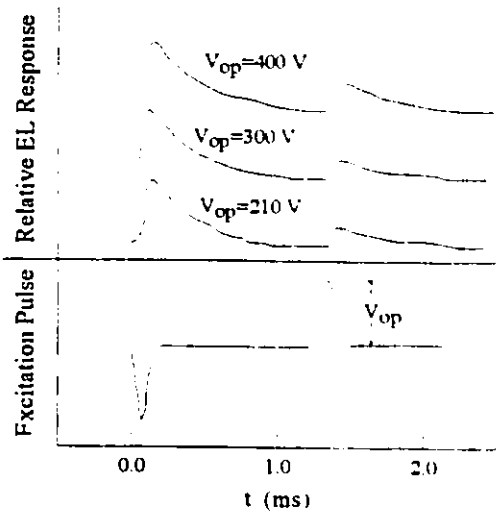

Fig. 7.5-1 EL response of ITO/Zn_2SiO_4:Mn/Y_2SiO_5/...../$BaTiO_3$/Al device.

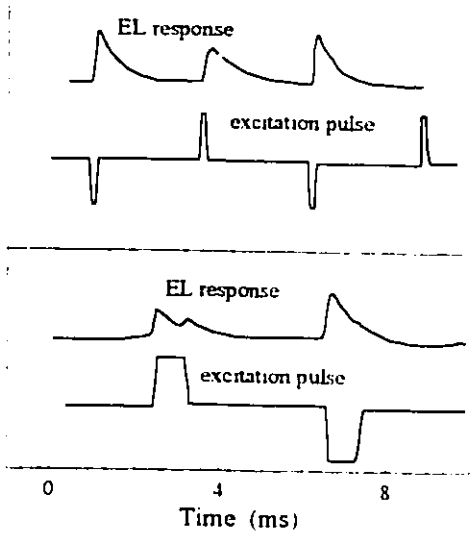

Fig. 7.5-2 EL response of ITO/Zn_2SiO_4:Mn/$BaTiO_3$/Al device. A trailing edge emission is observed when the positive pulse is applied on ITO electrode.

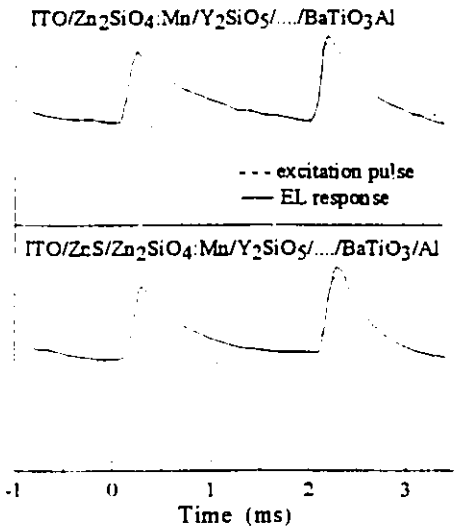

Fig. 7.5-3 EL response of ZnS enhanced and not enhanced ITO/Zn_2SiO_4:Mn/Y_2SiO_5/ ...../$BaTiO_3$ devices.

Figure 7.5-4 is the EL response of a Y_2SiO_5:Ce device. The sandwiched insulator/phosphor structure makes the excitation of negative pulses (on the ITO) possible due to the charge transfer from insulator-phosphor interfaces. In Fig 7.5-4(a), two phenomena are noticed: one is a weak leading edge excitation and the other a strong trailing edge excitation which was also noticed earlier in the EL response of the Zn_2SiO_4:Mn TFEL device shown in Fig. 7.5-2. This is never seen in the ZnS TFEL device. This effect was observed only in non-symmetrical oxide phosphor TFEL devices. The reason for it is still not clear. The other phenomenon is that when a negative pulse is applied to the ITO electrode, no EL is observed in non-symmetrical MSIM device structure as shown in Fig. 7.4-5(a). However, a multi-insulated structure will improve the EL emission as shown in Fig. 7.4-5(b).

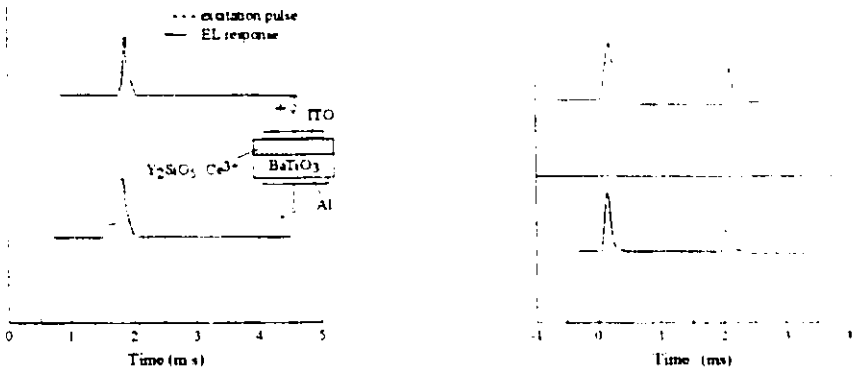

(a) (b)

Fig. 7.5-4 EL response of ITO/Y_2SiO_5:Ce^{3+} +Sm^{3+}/$BaTiO_3$/Al (a) and ITO/Y_2SiO_5:Ce^{3+}/ Zn_2SiO_4/ ..../Y_2SiO_5:Ce^{3+}/$BaTiO_3$/Al (b).

It is noticed that the non-symmetrical device structure MSIM of Figs. 7.5-2 and 7.5-3 have a common feature: when the pulse is applied on the Al instead of ITO, the luminescent efficiency decreased. The results can be expiained by a Schottky effect. A band diagram of a metal-oxide-semiconductor (MOS) structure is shown in Fig. 7.5-5 where the Zn_2SiO_4:Mn^{2+} thin film phosphor is supposed be slightly n-type and have a narrower band gap than the insulator layers. The Schottky barrier at the ITO-Zn_2SiO_4:Mn interface shows a diode effect. Only when ITO is positively biased, does the device become slightly conductive and the conductivity is space charge limited.

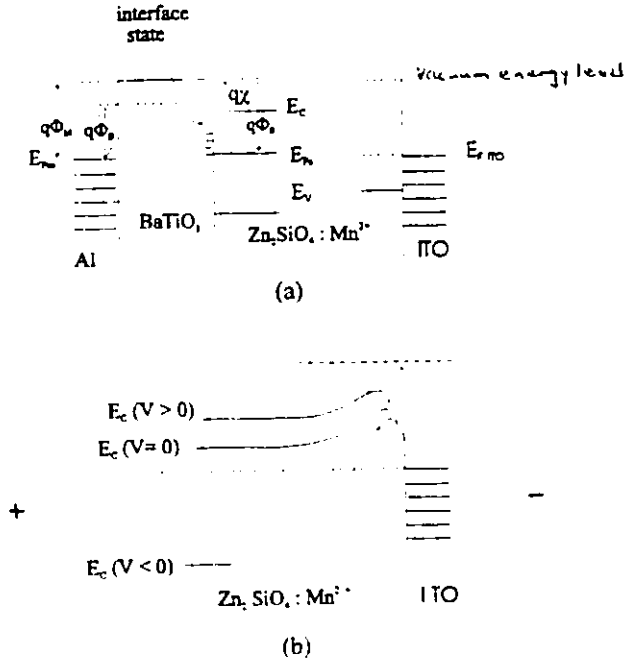

Fig. 7.5-5 Band diagrams of ideal metal-oxide-n-type Zn_2SiO_4-ITO structure (a) V=0, the bending of energy band is not considered; (b) the Schottky effect of oxide-metal contact. When a positive voltage is applied on the ITO side, electrons easily reach the electrode due to the lowering of the barrier height.

Why do we suppose the phosphor layer is n-type instead of neutral? As we know, the ideal insulator has a wide band gap greater than 3 eV so that it possesses very few charge carriers at practical temperatures. In practice, however, insulating films are generally amorphous and the usual model of a sharply defined energy band cannot be readily applied; rather, tails arise both at the top of the valence band and the bottom of the conduction band. These extend into the gap and overlap to form a continuous electron state distribution. When this happens, insulators assume semiconductor-like properties. Due to structural imperfec-

tions, there may actually be a relatively high density of charge carriers. They tend to be localized or trapped at these centers for a long time, and the insulator behavior stems from such carriers having very low mobilities [Ohring, 1992].

7.6 TRANSFERRED CHARGE

For the MSIM device structure in Fig. 3.4-1, below the threshold voltage V_{th} the device is purely capacitive and the resistance of the Zn_2SiO_4 thin film $R_s > 10^8\ \Omega$. The typical value of tanδ is smaller than 1.1×10^{-3} at a frequency of 10 K Hz. For ZnS, above V_{th}, R_s goes close to zero or even becomes negative and the phosphor film shows electrical breakdown necessary for efficient luminescence [Smith, 1981]. However, this is not true in oxide phosphors since the electron avalanche is limited. As we saw from the time domain response of electroluminescence, the breakdown is space charge limited and is usually limited to short intervals of about 1 μs on the leading edge of each pulse. When the breakdown takes place, the voltage on each layer of the devices will be redistributed and less voltage is applied on the phosphor layer.

Because of the non-linearity associated with the electrical characterization, as evidenced by the threshold behavior, the impedance description is unsuitable. The integrated charge can be measured using a Sawyer and Tower circuit described earlier in section 3.4.

Fig. 7.6-1 is the Q-V characteristic of $Zn_2SiO_4:Mn^{2+}$ and $Y_2SiO_5:Ce^{3+}$ thin film devices. The Q-V curves are also compared with $ZnS:Mn^{2+}$.

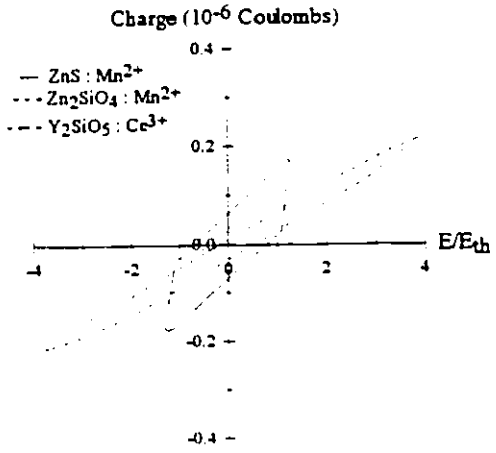

(a)

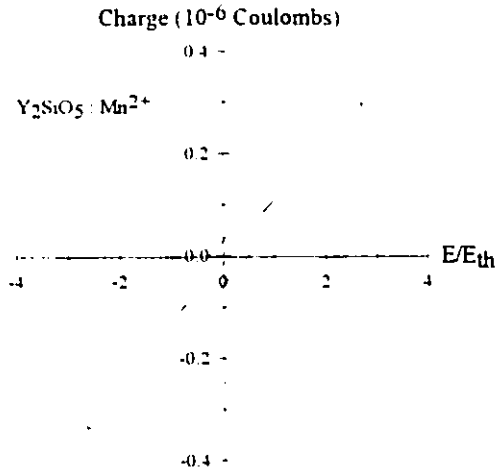

(b)

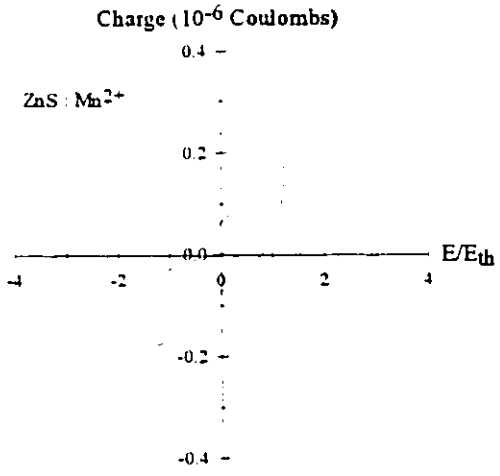

(c)

Fig. 7.6-1 Q-V characteristics of Zn_2SiO_4, Y_2SiO_5 and ZnS above threshold E_{th} (a) and the comparison between Y_2SiO_5 (b) and ZnS (c) both above and below the threshold.

Two common features are presented for oxide phosphors. The first is the lower dielectric loss even above threshold which is shown as the small area of the Q-V loop. The second is that there is no sharp increase of Q above the threshold as in ZnS. The charge mechanism may be explained as bulk-limited such as space-charge-limited or Poole-Frenkel emission, while in ZnS, the charge transfer mechanism was believed to be the tunneling from a Dirac well because of the device's characteristic insensitivity to temperature [Tannas, 1985].

The bulk-limited conduction mechanisms in insulators are shown in Fig. 7.6-2. Unfortunately, in our device, the electrical properties of the $BaTiO_3$ substrate are very sensitive to temperature, and we cannot measure the temperature dependence of the device.

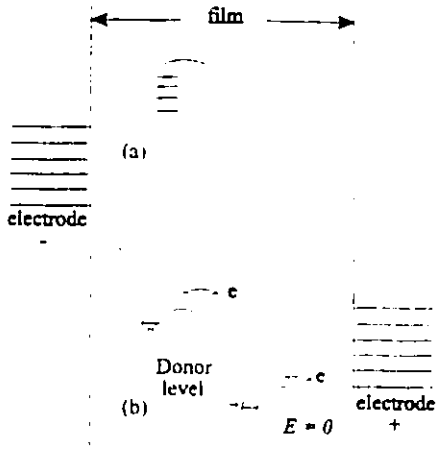

Fig. 7.6-2 Bulk-limited conduction mechanisms. (a) space-charge-limited; (b)Pool-Frankel.

7.7 EFFICIENCY OF Zn_2SiO_4:Mn TFEL DEVICE

The maximum achievable brightness of an ac TFEL device is determined by the maximum transferable charge and the maximum efficiency of electroluminescence η. The first is controlled by the charge at breakdown of the insulator while the latter is determined by the properties of the phosphor layer.

The efficiency η of EL can be expressed in turn as a photopic unit (lm/W), as an energy efficiency (%) or as a quantum efficiency (photons/electron×cm), where in quantum efficiency the distance means the thickness of the active film, i.e. distance traveled by the electron. The former is important from a technical point of view and the latter is suitable for explaining the physical process of the devices. In consideration of the physics and the structure of devices, EL efficiency η includes the following four independent parts [Müller, 1992]:

(1) η_{exc} is the probability of an electron hot enough to excite a center.

$$\eta_{exc} = \frac{\text{centers excited } (cm^{-3})}{\text{electrons transfered } (cm^{-2})} \tag{7.7-1}$$

(2) η_{lumin} is the probability of an excited center to decay radiatively;

(3) η_{out} is the probability of a generated photon to escape from the sample.

So we get the total efficiency η of the sample:

$$\eta = \eta_{exc}\ \eta_{lum}\ \eta_{out} = \frac{\text{photon flux}\left(\frac{\text{photons}}{cm^2 s}\right)}{\text{transferred charge}\left(\frac{\text{electrons}}{cm^2 s}\right)} \tag{7.7-2}$$

Another way to express efficiency is η defined by:

$$\eta = \frac{AL}{f \Sigma Q_t \, dV} \quad (\text{lumin /Watt}) \tag{7.7-3}$$

where A is the luminescent area of the device in ft^2, L is the brightness measured on the photometer in fL, and f is the frequency of the pulse, Q_t is the transferred charge, V is the voltage applied and $\Sigma Q_t dV$ is the loop area measured from the transferred charge shown in Fig. 7.7-1.

7.7.1 The Total Efficiency η

First, let us consider the number of photons emitted in the unit time (1 second) and then calculate the transferred charge or the number of electrons transferred in one second.

In practical measurement using the luminescent camera, the brightness B measured is the time average in consideration of efficacy, the human eye sensitivity to color from the photonic point of view [Kaufman, 1972]. Fig. 7.7.1-1 is the spectral luminescent efficacy and EL spectrum of the device ITO/ $Zn_2SiO_4:Mn^{2+}/BaTiO_3/Al$. From the definition, the luminescent efficacy is radiant flux (in Lumens) per Watt at a given wavelength [Kaufman, 1972].

Since the distribution spectrum of the device is off the center of human eye sensitivity, we can calculate the average spectral radiance (or luminous flux) per watt of the device from the following equation:

$$1\ (\text{Watt}) = \frac{\Sigma\ P(\lambda)\ S(\lambda)\ d\lambda}{\Sigma\ P(\lambda)\ d\lambda} \cdot 456\ (\text{Lumins})$$

$$= 456/4\pi\ = 37\ (\text{cd})$$

$$= 37\times10^4\ \text{cd/m}^2/\text{cm}^2 = 3.7\times10^5/3.426$$

$$= 1.08\times10^5\ (\text{fL/cm}^2) \qquad (7.7.1\text{-}1)$$

where $P(\lambda)$ and $S(\lambda)$ are luminescent efficacy and the EL spectrum of the device respectively and candela/cm^2 (cd/m^2) or foot lambent (fL) is the photometric unit for brightness.

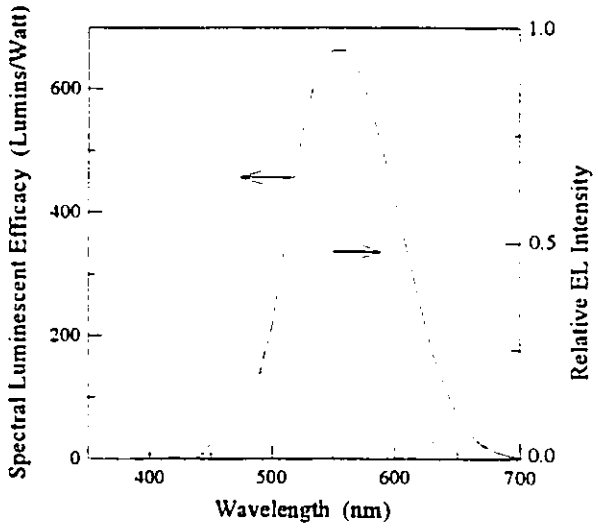

Fig. 7.7.1-1 The spectral luminescent efficacy and EL spectrum of the device ITO/Zn_2SiO_4:Mn^{2+}/$BaTiO_3$/Al.

For simplicity, we take the photons with a wavelength of 520 nm (or energy 2.365 eV) at the peak of the EL spectrum to calculate the number of photons, n, in one watt of optical power emitted from the device.

$$n = \frac{1}{2.365 \times 1.6 \times 10^{-19}} \text{ (photons /Watt)} = 2.64 \times 10^{18} \qquad (7.7.1\text{-}2)$$

For 400 Hz and 600 V (peak to zero) drive, the device has an average brightness of 54 cd/m^2 or 54/3.42=15.76 fL. We have:

$$\frac{15.76}{1.08 \times 10^{5}} \times 2.64 \times 10^{18} = 3.85 \times 10^{14} \text{ (photons)} \qquad (7.7.1\text{-}3)$$

Now, we are going to calculate the transferred charge. Given that the excitation $V_s = V_t = 600$ V (peak), frequency = 400 Hz, and d represents thickness, and

$C_s = 7.85 \times 10^{-10}$ F

$d_{sub} = 0.8$ mm, $d_{film} = 0.75$ m

$\varepsilon_{sub} = 5800$, $\varepsilon_{film} = 9.5\text{-}10.6$ m

The dielectric constants of the $BaTiO_3$ and Zn_2SiO_4 were measured at 400 Hz by using a MIM structure. However, under a high field (>1.6 MV/m), the dielectric constant will increase to 7000-8000 [Moulson, 1990], so we take $\varepsilon_{sub} = 7000$. The voltage ratio applied on the phosphor film would be:

$$r = \frac{V_{film}}{V_{sub}} = \frac{\varepsilon_{sub} d_{film}}{\varepsilon_{film} d_{sub}} = \frac{7}{8} \qquad (7.7.1\text{-}4)$$

Therefore, the voltage applied on the film is 600×7/15 = 280 V and the charge transferred will be:

$$Q_t = V_{film} C_s = 2.2 \times 10^{-7} \text{ coul} = 2.2 \times 10^{-7} / 1.6 \times 10^{-19}$$

$$= 1.37 \times 10^{12} \text{ electrons} \qquad (7.7.1\text{-}5)$$

Then the total efficiency of the device at 600 V (peak) driving voltage is:

$$\eta = \frac{\text{average } \textit{photons} \text{ emitted per second}}{2f\,(\text{electrons transferred per excitation})} = \frac{3.85\times10^{14}\ \text{photons}}{2\times400\times1.37\times10^{12}\ \text{electrons}}$$

$$= 0.35\ \text{photon/electron} \qquad (7.7.1\text{-}6)$$

or

$$\eta = \frac{\pi\,(8.2)^2\times10^{-6}\times15.76\ \text{lumens}}{400\times2.4\times10^{-5}\ \text{Watts}} = 0.172\ \ (\text{lm/W}) \qquad (7.7.1\text{-}7)$$

η under different driving voltages V_{op} is shown in Table 7.7.1-1.

Table 7.7.1-1 The total efficiency η of ITO/Zn_2SiO_4:Mn^{2+}/$BaTiO_3$/Al TFEL device at 400 Hz a.c. short pulse excitation:

V_{op} (V)	E_{film} (MV/cm)	B (fL)	P (Watt)	η (photon/electron)	(lm/w)
500	2.33	2	1×10^{-5}	0.053	0.10
600	2.80	15.76	2.4×10^{-5}	0.35	0.17
800	3.73	52	5×10^{-5}	0.87	0.55
1000	4.66	120	8.8×10^{-5}	0.98	0.78

From the above result we can see that the efficiency of the device increases with the field E_{film} applied on the phosphor thin film. However, the efficiency η of the device cannot be increased above 0.9 because device breakdown takes place above 1000 V.

Another interesting thing to be noted is that by depositing 2000Å of ZnS on the Zn_2SiO_4:Mn phosphor layer, the efficiency η of the device increased to 0.52 photon/electron at 600 V. The ZnS layer not only enhances the 'hot electrons' in the Zn_2SiO_4 layer and makes the electron threshold sharper after the V_{th}, but also decreases the breakdown voltage of the device due to the low breakdown voltage of ZnS.

7.7-2 OTHER EFFICIENCY PARAMETERS

In the TFEL device, the $BaTiO_3$ substrate is relatively rough as compared with a Si wafer. The waveguiding loss is greatly decreased. The exact quantity of η_{out} is hard to estimate because we did not get the information of 3-D surface morphology of the device.

The probability of an excited center to decay radiatively η_{lumin} can be calculated using the following equation [Mach, 1984]:

$$\eta_{lumin} = \frac{\tau(N)}{\tau_r} \qquad (7.7.2\text{-}1)$$

where τ (N) is decay time measured, which depends on the Mn^{2+} dopant quantity N. For our thin film of 2% mole Mn-doped Zn_2SiO_4 thin film, the decay time is 0.6 ms. τ_r is the radiative decay time for very low concentrations Mn^{2+} dopant and was measured as 10.5 ms by photoluminescence measurement [Barthou, 1994], so $\eta_{lumin} = 0.057$.

The probability of an electron hot enough to excite a center, η_{exc}, can be calculated using the equation [Mach, 1984]:

$$\eta_{exc} = l_a^{-1} = \sigma N \qquad (7.7.2\text{-}2)$$

where l_a is the impact length, σ is the impact cross-section and N is the concentration of Mn dopant. The impact cross-section σ depends slightly on the field applied and is estimated to be $\sigma_{Mn^{2+}} = 2\times10^{-16}$ cm^2 in ZnS where it is known [Williams,1981]. For an Mn concentration of 2% mole or $2.1\times10^{18}/cm^{-3}$, $\eta_{exc} = 4.2\times10^{2}/cm^{-1}$. The increase of Mn dopant will increase η_{exc}, but concentration quenching will dominate due to the energy transfer between the close Mn^{2+} ions.

7.8 SUMMARY

In the ZnO-Y_2O_3-SiO_2 system, Willemite Zn_2SiO_4:Mn is proved to be the only efficient EL phosphor. It has not only a bright, vivid green color matching the human eye sensitivity but is also insensitive to humidity. It is stable chemically, electrically under an ordinary air environment. Y_2SiO_5 is unsuitable for EL application due to its low density of hot electrons even under the field near the breakdown. Some of the material properties of Zn_2SiO_4 we measured are summarized in Table 7.8-1.

Table 7.8-1. Properties of sputtered α-Zn_2SiO_4:Mn (2% mole) thin film phosphor.

Forbidden gap, E_g	5.4-5.6 (eV)
Dielectric constant, ε_r	9.5~10.5 (400 Hz)
Dielectric strength, E_b	8-9×10^6 (V/cm)
Crystallization temperature	850-950°C (substrate dependent)
$I_{EL,max}$ (at 400 Hz)	90 (fL)
Optical transp. (0.8 μm film)	84% (280 - 600 nm)
Decay time EL	0.6~0.7 (ms)
Color coordinates	x= 0.1~0.2, y= 0.64~0.71
Dominant wavelength	510~520 nm
Excitation purity	~77%
Avalanche field, E_{th}	9.8×10^5 (V/cm)
Solubility	soluble in dilute HF, hot HCl

CHAPTER 8

CONCLUSIONS AND SUGGESTIONS FOR FUTURE WORK

8.1 SUMMARY

RE^{3+}-doped Y_2SiO_5, $Y_2Si_2O_7$, $Y_{4.67}(SiO_4)_3O$ and Mn^{2+}-doped Zn_2SiO_4 thin films were prepared by magnetron sputtering. The composition between the sputtering target material and the thin film deposited was studied by RBS. In order to find the best RE dopants and the dopant quantity, the cathodoluminescence of powder phosphors were studied. It was found that Eu (3-5% mole), Tb (3-5% mole) and Ce (2% mole) are the best dopants for the RGB color of yttrium silicate phosphors.

The influence of the target material and the sputtering parameters (substrate temperature, sputtering pressure, target-substrate distance and the deposition speed) upon the thin film composition, thickness distribution and crystal structure were studied.

Zn_2SiO_4 (green) and Y_2SiO_5:Ce (blue) TFEL devices with various structures on the $BaTiO_3$ substrate were prepared and their electroluminescent properties were studied by change the excitation a.c. voltage amplitude, frequency and pulse duty time. Typical Zn_2SiO_4:Mn (2% mol.) and Y_2SiO_5:Ce (3%) TFEL devices show brightnesses of 80 fL with a decay time of 0.6 ms, and 0.1 fL with a decay time of less than 10 μs respectively at the short a.c. pulse excitation of 400 Hz frequency and 900 V (peak value) amplitude. The EL results of sandwiched $Zn_2SiO_4/Y_2SiO_5/...$ or $Zn_S/Zn_2SiO_4/....$ proved that

Zn_2SiO_4 thin film is a much better host for EL applications than Y_2SiO_5 due to the longer mean free path of electrons traveling in Zn_2SiO_4.

Experiment results of the transferred charge and time resolved spectra were compared with that of ZnS:Mn. It is found that above the threshold voltage, the electron avalanche in oxide phosphors is limited by the space charge. The efficiency of Zn_2SiO_4:Mn TFEL devices were studied. It is noticed that the maximum efficiency of the device is 0.98 $\frac{\text{photons}}{\text{electrons}}$ or 0.78 $\frac{\text{lumins}}{\text{Watt}}$. The maximum efficiency of the device is determined by the breakdown of the device.

8.2 FUTURE WORK PROPOSED

Since yttrium silicates were proved to be inefficient for EL applications, the work should concentrate on EL properties of Zn_2SiO_4 thin film phosphor, many EL properties of which are still unknown. The future work is suggested in the two main areas: one to find new device structures or a low substrate temperature deposition method and the other to reveal further electrical and physical properties of Mn or other TM and RE activated Zn_2SiO_4.

For device structures other than using $BaTiO_3$ as substrates, we tried the structure ZnO:Al/Y_2O_3(or SiO_2, $BaTiO_3$)/Zn_2SiO_4:Mn/Y_2O_3(Or SiO_2, $BaTiO_3$)/Pt(or ZnO:Al)/ quartz with using either transparent electrode ZnO:Al (1000Å) or Pt (1000Å) as the back electrode. The purpose of using ZnO:Al and Pt as the back electrode is that they can resist a temperature as high as 900°C which is necessary for the crystallization of Zn_2SiO_4.

However, micro-cracks induced in the film at high annealing temperature and made the device short-circuit. For the device applications, it is necessary to find a method for low temperature processing of crystallized Zn_2SiO_4 thin film. One possible solution is to use ZnS and Si or SiO_2 as the starting material and another possible way is in-situ sputtering by using $Ar:O_2:H_2$ mixture gas. Other processes such as laser-assisted deposition or plasma-assisted CVD may decrease the deposition temperature.

For Zn_2SiO_4 thin films, the following electrical and luminescent properties need to be studied:

(a) Energy distribution of 'hot electrons' in the thin film. The experiment can be achieved by preparing a 'cold cathode' by coating a very thin gold layer (100-200Å) on the Zn_2SiO_4 thin films as the grating or energy filter [Carkner, 1992].

(b) Electron-phonon interactions by measuring the phonon spectra. Field-quenching mechanisms by measuring the CL spectra, CL intensities and the decay curves when a electrical field is applied on the sample.

(c) Concentration quenching of EL by changing the dopant quantity in Zn_2SiO_4. Impact cross-section of Mn^{2+} in Zn_2SiO_4 and its dependence on the fieldstrength.

(d) Influence of interface-state on the device properties.

(e) Energy band structures of Zn_2SiO_4 and the energy level of TM dopants in Zn_2SiO_4 by means of thermal-enhanced luminescent spectra, etc.

Appendix A: Photomultiplier Response (Model No. Oriel 77346)

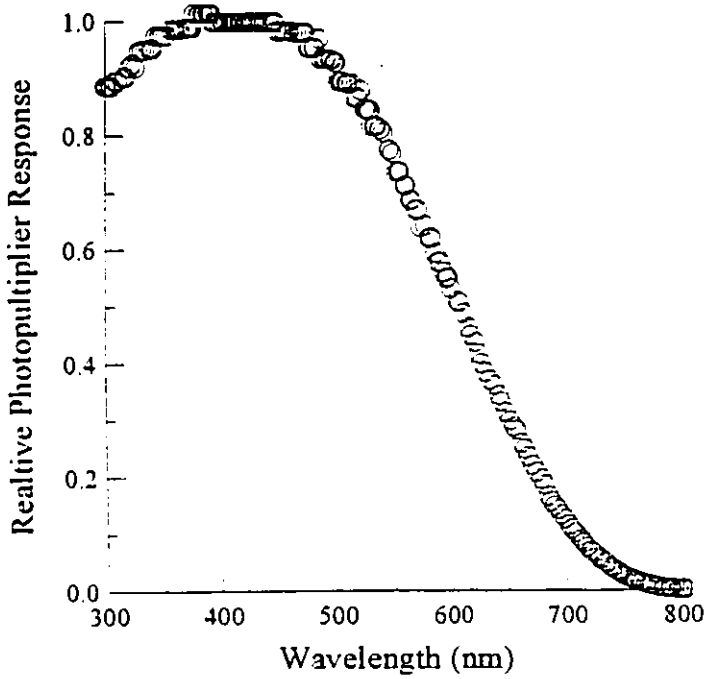

Appendix B CIE 1931 Tristimulus Values

X	Y	Z	λ (nm)
.0154	.0004	.0732	400
.0289	.0008	.13765	405
.0504	.0014	.24075	410
.0 8895	.0026	.4265	415
.1462	.00475	.7052	420
.20915	.0078	1.0156	425
.27165	.01205	1.33105	430
.3161	.0173	1.56635	435
.3383	.0233	1.7028	440
.34225	.0305	1.7596	445
.3334	.0389	1.76335	450
.3135	.049	1.72065	455
.2431	.0755	1.4784	465
.1966	.09325	1.285	470
.1455	.115	1.0503	475
.10005	.14095	.82905	480
.0638	.1735	.6391	485
.03635	.21395	.48475	490
.01845	.2655	.3686	495
.00855	.33295	.2828	500
.0071	.413	.2151	505
.01575	.50775	.162	510
.0363	.6065	.1182	515
.06935	.7007	.0845	520
.1144	.786	.0602	525
.16765	.85405	.04355	530
.22795	.908	.03125	535
.2927	.9476	.0216	540

X	Y	Z	λ (nm)
.3619	.9745	.0145	545
.4359	.99025	.00955	550
.51395	.995	.0063	555
.59525	.9894	.0042	560
.6783	.9735	.003	565
.76045	.947	.00225	570
.8392	.911	.0019	575
.91055	.86585	.0016	580
.9713	.8135	.0014	585
1.01765	.7556	.0012	590
1.04425	.694	.00095	595
1.05115	.63085	.0008	600
1.0324	.567	.00055	605
.992	.504	.0004	610
.9284999	.442	.00025	615
.8449	.3811	.00015	620
.7484	.323	.0001	625
.64665	.269	.00005	630
.54515	.22	0	635
.45135	.1776	0	640
.3657	.141	0	645
.28975	.1099	0	650
.2242	.084	0	655
.16995	.0631	0	660
.12615	.0465	0	665
.0924	.0339	0	670
.0671	.0245	0	675
.04825	.01755	0	680
.03475	.0126	0	685
.02435	.0088	0	690
.01705	.00615	0	695

Appendix C: QUICK BASIC program for calculating the chromaticity coordinats, excitation purity, and the dominant wavelength.

```
'A PROGRAM TO CALCULATE COLOR COORDINATE OF SPECTRA OPENED IN FILE
 #1
'FILE #2 IS THE OUTPUT CHROMATIC DATA OF CALCULATIONS
'FILE #3 INPUTED IS THE CIE CHROMATICITY COORDINATES (31's or 63's)
'FROM 400-700 nm WITH A INTERVAL OF 0.1 nm.
'FILE #4 IS THE CALIBRATION DATA OF SILICON DETECTOR
   GOTO 10
5  PRINT "THERE ARE SOME ERROR IN THE PROGRAM. TRY AGAIN!"
   GOTO 20
10  CLS


20 PRINT " "
   PRINT " "
   PRINT "   THIS PROGRAM CALCULATE COLOR COORDINATS OF
             LUMINESCENT"
   PRINT "   SPECTRUM------BE SURE TO MAKE THE WAVELENGTH OF YOUR
             SPECTRUM"
   PRINT "   IN THE RANGE 291 nm < LAMBDA, AND > 701 nm, IF IT IS NOT IN"
   PRINT "   THE RANGE, ADD LINE, '291, 0' AT THE BEGINNING AND A LINE '701,
              0' AT THE END OF YOUR SPECTRUM  RESPECTIVELY!!!"
   PRINT "              **********************          "
   PRINT " "
   PRINT " "
   PRINT " "
   INPUT " INPUT THE NAME AND PATH OF SPECTRUM MEASURED", din1$
   PRINT "----------------------------------------"
   INPUT " INPUT THE OUTPUT FILENAME \PATH\COLOR.XY "; dout$
   PRINT
   PRINT "  ************************************************"
   PRINT "  *  Please wait for computer processing data   *"
```

```
PRINT "  ************************************************"

'a3=wavelength, b3=x, d3=y, e3=z( cie chromaticity coordinates )
OPEN "d:\thesis\data\cie31xyz.dat" FOR INPUT AS #3
DIM b3(301), d3(301), e3(301), c(301)
FOR j = 1 TO 301
INPUT #3, b3(j), d3(j), e3(j), c(j)
NEXT j

'a4=wavelength, h4=responce of silicon detector
OPEN "d:\thesis\data\detect.dat" FOR INPUT AS #4
DIM a4, h4(301)
FOR j = 1 TO 301
INPUT #4, a4, h4(j)
NEXT j
'cieraw.dat is the normalized chromatic coordinates in polar axis with
'c as the origin there are three columns:
'r=distance from (x,y) to point c, th=theta, c1(j)=wavelength
OPEN "d:\thesis\data\cie31raw.dat" FOR INPUT AS #5
DIM th(301), R(301), c1(301)
FOR j = 1 TO 301
INPUT #5, R(j), th(j), c1(j)
NEXT j

OPEN din1$ FOR INPUT AS #1
OPEN dout$ FOR OUTPUT AS #2
DO UNTIL EOF(1)
        i = i + 1
        LINE INPUT #1, a$
LOOP
CLOSE #1
'FIND OUT THE ROWS i OF INPUT FILE #1

OPEN din1$ FOR INPUT AS #1
```

```
DIM a1(i), b1(i)
j = 0
DO UNTIL EOF(1)
        j = j + 1
        INPUT #1, a1(j), b1(j)
LOOP
'PUT INPUT SPECTRUM DATA MEASURED INTO TWO ARRAYS

GOSUB 200
'SORTING ARRAY a1(j), b1(j) IN A ASCENDING ORDER

'Inserting data into arrays and generating new data
'wavelength X(j) start from 400 nm to 700 nm with an interval of 0.1 nm
c = 0
x = 0
y = 0
z = 0
40 DIM h(301)
  FOR j = 1 TO 301
    c = 399 + j
    GOSUB 300
    'FIND OUT DATA X1, Y1. X1 IS JUST SMALLER THAN C
    GOSUB 400
    'FIND OUT DATA X2, y2 and X2 IS JUST GREATER THAN C
    F = (c - x1) / (x2 - x1)
    h(j) = (y1 + (y2 - y1) * F) / h4(j)
    IF h(j) < .1 GOTO 60
    x = x + h(j) * b3(j)
    y = y + h(j) * d3(j)
    z = z + h(j) * e3(j)
60 NEXT j
  t = x + y + z
  tx = x / t
  ty = y / t
```

```
tz = z / t

PRINT "The chromaticity coordinates of the spectrum calculated is:"
PRINT "x="; tx, "y="; ty
PRINT #2, "The chromaticity coordinates of the spectrum calculated is:"
PRINT #2, "x="; tx, "y="; ty

tx = tx - .3101
ty = ty - .3163
rl = SQR(tx * tx + ty * ty)
m = .4641
b = -.24801
IF tx = 0 GOTO 42
t = ABS(ty / tx)
theta = ATN(t)
theta = theta * 180 / 3.1415926#
GOTO 48
42 IF tx = 0 AND ty > 0 THEN
   theta = 90
  ELSEIF tx = 0 AND ty < 0 THEN
   theta = 270
  END IF
  GOTO 50
48 IF tx > 0 AND ty >= 0 THEN
   theta = 0 + theta
  ELSEIF tx < 0 AND ty > 0 THEN
   theta = 180 - theta
  ELSEIF tx < 0 AND ty <= 0 THEN
   theta = 180 + theta
  ELSEIF tx > 0 AND ty < 0 THEN
   theta = 360 - theta
  END IF
50 IF theta >= 293.7096 AND theta <= 363.1544 THEN
   m1 = ty / tx
```

```
    D0 = (b / (m1 - m)) * SQR(1 + m1 ^ 2)
  ELSE
    'SEARCHING FOR DOMINANT WAVELENGTH AND D0 FOR SPECTRUM COLOR
    GOSUB 450
  END IF
  EP = r1 / D0 * 100
  PRINT "Theta="; theta
  PRINT "DOMINANT WAVELENGTH ="; DW
  PRINT "THE EXCITATION PURITY (EP) ="; EP; "%"

  PRINT #2, "DOMINANT WAVELENGTH ="; DW
  PRINT #2, "THE EXCITATION PURITY (EP) ="; EP; "%"
  CLOSE #5
  CLOSE #4
  CLOSE #3
  CLOSE #2
  CLOSE #1

  PRINT "Do you want to retrieve another file? (Y/N)"
  IF G$ = "Y" OR G$ = "y" OR G$ = "yes" OR G$ = "YES" GOTO 10
600 END

200 'SUBROUTINE --- INSERTION SORTING A ARRAY IN A ASCEDING ORDER ---
  'THE ARRAYS a1(K), b1(K) HAVE i ENTRIES
  FOR j = 1 TO i - 1
  k = j
  x = a1(j + 1)
  y = b1(j + 1)
210 IF k = 0 THEN 220
  IF x >= a1(k) THEN 220
  a1(k + 1) = a1(k)
  b1(k + 1) = b1(k)
  k = k - 1
  GOTO 210
```

```
220 a1(k + 1) = x
    b1(k + 1) = y
    NEXT j
    RETURN

300 'SUBROUTINE TO FIND OUT A DATA IN ARRAY A(j) JUST LESS THAN C
    FOR k = i TO 1 STEP -1
    IF a1(k) < c THEN 310
    NEXT k
310 x1 = a1(k)
    y1 = b1(k)
    RETURN

400 'SUBROUTINE TO FIND OUT A DATA IN ARRAY JUST LARGER THAN C
    FOR k = 1 TO i
    IF a1(k) > c THEN 410
    NEXT k
410 x2 = a1(k)
    y2 = b1(k)
    RETURN


450 'SUBROUTINE TO SEARCH THE DOMINANT WAVELENGTH AND EP FROM
GIVEN CIE
    'DATA FILE
    FOR j = 1 TO 301
    IF ABS(theta - th(j)) < 1 GOTO 455
    NEXT j
455 DW = c(j)
    D0 = R(j)
    RETURN
```

Appendix D: Sputtering theory:

Sputtering is a process of depositing thin film materials by means of glow discharge where low pressure gas (Ar, He, O_2, N_2, H_2 or their mixture) is ionized under D.C. or R.F. field between the two parallel plates (a diode), cathode and anode[Vossen, 1991]. The substrates where thin films are deposited are attached on the anode while the target material for the material source is put on the cathode. Under a certain voltage (D.C. sputtering) or R.F. power, gas begin to discharge and a stable plasma is generated. The ionized gas ions will be accelerated towards the cathode. If these ions have enough energy, they will sputter out the target material in the forms of molecules, atoms and ions. These sputtered out particles have a certain energy and will be deposited on the substrates.

In our process, we use an R.F. magnetron sputtering system as shown in Fig. D-1. The R.F power source is necessary for insulator targets. The frequency used is 13.6 MHz, a industrial standard without interference of communications. In r.f sputtering, if the target is an insulator, when a negative pulse is applied to the target, gas ions will impinge on the target and cause sputtering. This bombardment will last for about 10^{-7} sec, after which time there will have built up a positive charge on the surface of insulator. This terminates the high energy ion bombardment and sputtering after 10^{-7} sec. Then a short positive pulse is applied to the target and electrons will be accelerated toward the insulator, and build up a negative surface charge (in about 10^{-9} sec) that will counterat the positive potential and neutralize the insulator. Therefore, the next negative pulse can sputter the insulator again. Fig. D-1 (b) shows the plasma potential for an asymmetric "diode". A magnetic field on the cathode will not only stabilize the plasma but will also lower the sputtering pressure and increase the sputtering field.

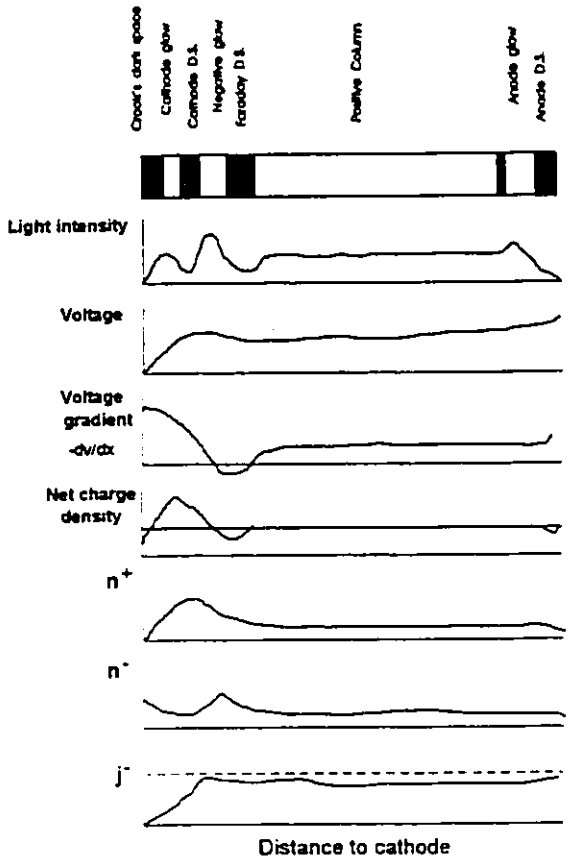

(a)

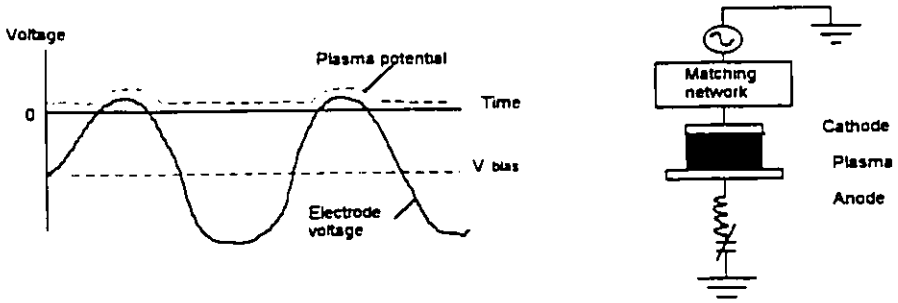

(b) (c)

Fig. D-1 The voltage, light and charge distributions between two planar plates (a), the plasma potential for asymmetric "diode" (larger area of anode) (b) and the diagram of sputtering system (c).

The magnetic structure shown in Fig. D-2 is called a magnetron. For simplification, consider a D.C. planar cathode. Sputtering begins only when the plasma is stable. Plasmas are moderately conductive and therefore are only weakly perturbed by the application of an electric field $\vec{E}$. However, the application of a magnetic field can have very significant effect. A moving charge q in the magnetic field is subject to a force $F_m = q\vec{E} \times \vec{B}$. For a charged particle moving perpendicular to a magnetic field, the force will cause the particle to move in an orbital path with radius $r = \sqrt{2mE_k} / qB$. E_k is the kinetic energy of the particle. For the circular planar magnetron cathode we used, the parallel component $B_{//}$ of the magnetic field plays an important role in achieving low pressure sputtering. Electrons are trapped above the target surface to form a closed loop or path along $\vec{E} \times \vec{B}$. The secondary electrons emitted from the cathode as a result of ion bombardment are approximately constrained to this annular region, resulting in increased ionization and a much denser plasma.

Magnetron sputtering system has the following advantages over conventional planar sputtering:

(1) Increases sputtering speed 3-10 times.

(2) Lowers the plasma sustaining pressure down to 6×10^{-4} torr, which is an advantage for deposition of high purity materials.

(3) Preferred orientation in thin films can be achieved at lower substrate temperature.

(4) Low electron impingement damage to semiconductor thin films.

The disadvantage of magnetron sputtering is the loss of uniformity of thin film thickness. However, this can be solved by moving target, rotating the substrate or both.

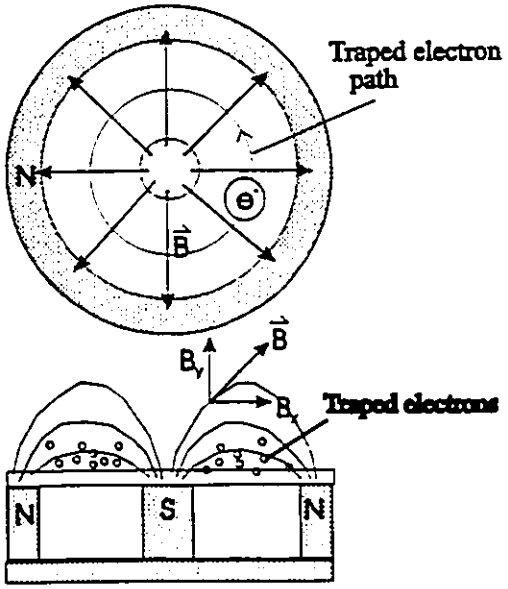

Fig. D-2 A circular planar magnetron cathode.

In our system, a target with a thickness of 2-10 mm is used, the maximum $B_{//}$ applied on the target surface will be less than 500 Gauss. This discharge mode is called "positive space charge (PSC) mode". In this mode, the drift speed of electrons, μ_e, will be greater than those of positive ions μ_i ($\mu_e/\mu_i > 1$). Therefore, positive space charge is accumulated between the target and the substrate. One of the other characteristic of PSC mode is that the deposition speed of thin films is proportional to the r.f. power applied.

If the working pressure of sputtering is 5×10^{-3} torr, $B_{//}$=300 Gauss, r.f. voltage is 340 V, the mean free path of an electron, with a mass-charge ratio e/m, at 1 Torr pressure is $\lambda_{mfp}\approx2\times10^{-3}$ m. The resonance frequency ω and the mean impingement time of electrons are:

$$\omega = B_{//}\times(e/m) = 8.79\times10^{10} \ (r/sec) \qquad (D\text{-}1)$$

$$\tau = \lambda_{mfp} / P[2(e/m)V]^{1/2} = 2.2\times10^{-9} \ (sec) \qquad (D\text{-}2)$$

Even under lower pressure, the trapped electrons move above the target in the trajectories of closed loops. These trapped electrons ionize gas atoms above the target surface and increase the positive ion density which sputter out the target materials. The ionic density enhancement is equal to the increase of pressure. The equivalent pressure P_e was suggested by Francis [Francis, 1960]. The relationship between P_e and the real pressure is:

$$Pe / P \approx [1+(\omega\tau)]^{1/2} \qquad \text{(D-3)}$$

For the US-GUN, if the average $B_{//}$ is 300 Gauss, a working pressure of 5×10^{-3} Torr is equivalent to a pressure of 1.7×10^{-1} Torr without the magnetic field. Therefore, plasma is easy to sustain in magnetron sputtering.

Different target materials have different sputtering yield. Some sputtering yields for oxide targets are shown in Table D-1 [Kamiyama , 1983].

An increase of deposition speed and an increase in cathode voltage result in more energetic particle bombardment. Therefore, a high compressive stress will be likely to be accumulated in the thin film due to rearrangement of condensing layers by recoil implantation and, to a lesser degree, by entrapment of the incident working gas.

Substrate temperature determines undercooling, atomic mobility and solid reaction during the thin film deposition. Crystallized thin films can be deposited either by in-situ high-substrate-temperature deposition or low-substrate-temperature deposition followed by post-annealing in air. We chose the latter because it easy to control thin film compositions.

The preferential sputtering effect in multi-component target materials is the major reason for composition deviation of thin films from that of the target. The deviation can be predicted according to *mass effects*, *bonding effects* [Betz, 1983] and the *sticking coefficient*.

Table D-1 Sputtering yield Y of some metals and their oxides (10 keV Kr^+ion):

Oxides	Y_{oxide}[total atoms/ion]	Y_{metal}[atoms/ion]
$Y_2Si_2O_7$**	1.6	
Zn_2SiO_4**	3.7	
ZnO**		
ITO**	50	
Al_2O_3	1.5	3.2
MgO	1.8	8.1
MoO_3	9.6	2.8
Nb_2O_5	3.4	1.8
SiO*	2.2	
SiO_2	3.6	2.1
SnO_2	15.3	6.5
Ta_2O_5	2.5	1.6
TiO_2	1.6	2.1
UO_2	3.8	2.4
V_2O_5	12.7	2.3
WO_3	9.2	2.6
ZrO_2	2.8	2.3

* Obtained from US' GUN II manual. ** Our experimental result.

Mass Effects: This will cause preferential sputtering of lighter component (Si) and therefore surface enrichment of heavier component (Y). In the KeV range, the following equation was derived in the ratio of the component sputtering yields in binary alloy due to the cascade[Kelly, 1978].

$$Y_A^{\infty}/Y_B^{\infty} = (M_B/M_A)^{2m}(U_B/U_A)^{1-2m}; \qquad \text{(D-4)}$$

with $0 \le m \le 0.2$ depending on the energy and M_j and U_j being the mass and surface binding

energy of the atoms of component j. The situation may become more complicated if surface charging is considered for our highly insulated Zn-Y-Si-O system.

The angular distribution of different mass predictes that heavier ions will be more likely distributed in the normal direction to the target.

Bonding Effects: Differences in the surface binding energy of the constituents will result in a preferential emission of the component with the lower binding energy (Si-O) and therefore cause enrichment of the component with the higher surface binding energy (Y-O). For a random binary alloy the surface binding energies U_A and U_B have been expressed by Kelly [Kelly, 1978] as functions of the nearest-neighbor bond strengths U_{AA}, U_{BB}, and U_{AB}. Thus, one obtains for U_A:

$$U_A = -C_A^S Z_S U_{AA} - C_B^S Z_S U_{AB} \qquad \text{(D-5)}$$

where Z_S is the surface coordination number. From the first-order approximation as functions of ΔH_A and ΔH_B, Kelly obtained the following result for linear cascade sputtering:

$$\frac{Y_A^S}{Y_B^S} = \frac{C_A - \gamma C_B (1 - C_B^S)\Delta H_B + (1 - C_A^S)\Delta H_A}{C_B - \gamma C_A (1 - C_A^S)\Delta H_A + (1 - C_A^S)\Delta H_B} \qquad \text{(D-6)}$$

predicting enrichment of the component with the higher surface binding energy or heat of atomization.

Sticking Coefficient: For sputtered atoms, a sticking probability of 0.5-0.9 was reported [Nelson, 1961]. It depends on the surface conditions, the temperature and the amount of adsorbed surface material.

Four kind of targets can be used, a alloy, mosaic metal, sintered ceramic and sintered powders. It is known that due to the preferred sputtering and different target surface morphology, the composition of thin films will deviate from that of targets when

depositing compounds[Vossen, 1992]. For deposition of oxide thin film phosphors, we find that powder is the best form for depositing thin films. The reasons are: (1) inexpensive and flexible to adjust the composition. (2) less influence by the composition change due to preferred sputtering. For the deposition of the transparent electrode, commercial ceramic indium tin oxide (ITO) target and Al doped ZnO:Al ceramic target, both from CERAC™, were used.

Depending on the target composition and firing temperature, sputter targets may contain a mixture of quaternary, ternary, and/or binary phases. Generally speaking, the film composition differs from that of target. Si deficiency is thought to be primarily due to the preferential re-sputtering of Si off the substrate by negative ions, primarily O^-, accelerated away from the target. The source of O^- is believed to be the Si-O compounds, although Y-O compounds may also play a role. However, non-uniform, mass-depending angular distributions of species sputtered from planar magnetron targets, in which heavier elements (Y, RE) are ejected at angles closer to normal, apparently also plays a role. Substrate temperature and the sputtering gas oxygen content also strongly affect the film composition. At low substrate temperature, better stoichiometry has been obtained in pure Ar atmosphere. If oxygen is present in the sputtering gas, the substrate should be heated.

BIBLIOGRAPHY

Ashcroft, N.W. and Mermin, N.D. : *Solid State Physics*, Holt, Rinehart and Winston, 1976, pp9.

Avouris, Ph. , et al: *Trapping and Luminescence Mechanisms in Manganese-doped Zinc Silicate Phosphors--A tunneling Model*, J. Electronic Mat., Vol. 10, No. 5, (1981)887.

Barthou, C. et al.: *Mn^{2+} Concentration Effect on the Optical Properties of Zn_2SiO_4:Mn Phosphors*, J. Electrochem. Soc., 141, (1992)524.

Behrisch, R.: *Sputtering by Particle Bombardment I- Physical Sputtering of Single-Element Solids*, Vol. 47, Springer-Verlag, 1981.

Betz, G. and Wehner, G. K. : *Topic in Applied Physics-Sputtering by Particle Bombardment II*, Edit. R. Behrisch, Springer-Verlag Vol.52.

Blasse, B. : *Chemistry and Physics of R-activated phosphors*, Handbook of Physics and Chemistry of Rare Earths, Edited by K.A. Gschneidner, Jr. and L. Eying, North-Holland Publishing Co., (1979), p.237.

Blasse, G. and Bril, A. : *A New Phosphor for Flying-Spot Cathode-Ray Tube for Color Television: Yellow-Emitting $Y_3Al_5O_{12}$-Ce^{3+}*, Appl. Phys. Lett.,15, (1967), 53.

Blevin, F. : *In proc. 3rd Int. Conf. Ionization Phenomena in Gases* (1960).

Born, P.J. , et al.: *A Study of Phosphors in the Yttrium Oxide-Silicon Dioxide Phase System*, J. Mater. Sci. Lett., 4, (1985)497.

Bragg, W.L. , W.H. Zachariasen: *The Crystalline Structures of Phenacite, Be_2SiO_4 and Willemite, Zn_2SiO_4*, Kristallogr, 1930, pp.518-528.

Buisson, G. and Michel, C. , Mat. Res. Bull. 3, (1968)193.

Bunting, E.N. , J. Am. Ceram. Soc., 13[1]5-10(1930].

Chin'Hang, M.A.S. , Soviet Physics-Cryst., 15 (1970)387.

Clerjaud, B. : *Current Issues in Semiconductor Physics*, Edited by A.MM. Stoneham, Adam Hilger, 198 pp117.

Clogston, A.M. , J. Phys. Chem. Solids, 7, 201(1958).

Dieke, G. H. : *Spectra and Energy Levels of Rare Earth Ions in Crystals*. Interscience Publishers, 1968.

Donnary, J.D. , *Crystal Data Determinative Tables*, 3rd Ed., Vol.2, 1973, ppH-35.

Francias, G.: *Ionization phenomena in Gases, Butterworthas Publication Ltd.*, 1960.

Godlewski, M. , et al: *Excitation Mechanism of Luminescence Excitation of Rare-Earths and Transition Metals in Solids*, J. Luminescence, 48&49 (1991)23.

Gomes de Mesquita, A.H. and Bril, A. : *Preparation and Cathodoluminescence of Ce^{3+} -activated Yttrium Silicates and Some Iso-structural compounds*, Mat. Res. Bull. 4, (1969)643.

Hidden, W.E. and Mackintosh, B.J. (1889): *A description of several yttria and thoria materials from Llano County.* Meet., GAC, MAC, MSA, AZOPOPO, Kingston, Ont., 27.

Hufner, S. : *Optical Spectra of Transparent Rare Earth Compounds*, Academic Press, 1978.

Ingerson, E. , et al.: Am. J. Sci., 246[1]21-40(1948)

ITo, J., et al: *Synthesis and Study of Yttrialite*, The American Mineralogist, 53, (1968)1941.

Kamiyama, et al: *Handbook of Thin films*, edited by 131 Thin Film Committee, Scientifc Society of Japan, Om Press, in Japanese, 1983.

Kaufman, John E. , *IES Lighting Handbook*, 5th edition, Illuminating Engin. Society, 1972.

Kazan, B. , Science, 203 (1980)927.

Kelly, R. ; Nucl. Instrum. Methods 149, (1978)553.

Khrupunkov, A.N. and Malyavskii, N.I. : *Use of Amine Version of Sol-Gel Synthesis for Production of Zinc Silicate Materials*, 1989.

Klaska, H.K. , et al., Acta. Crystallogr., B34, 3324(1978).

Liddell, K. and Thompson, D.P. : *X-ray Diffraction Data for Yttrium Silicates*, Br. Ceram. Trans. J., 85, (1986)17.

Meijerink, A. , et al.: *Photo-stimulated Luminescence and Thermally Stimulated Luminescence of Y_2SiO_5-Ce, Sm*, J. Mater. Sci. (1991)997.

Minami, T., et al, SID'92, Boston, (1992)17-22.

Minami, T. , et al: *Blue-emitting TFEL devices*, SID'93 Europe, EL-P12.

Moulson, .J. and Herbert, J.M. : *Electroceramics-Materials-Properties-Applications*, Chapman and Hall, 1990, pp249.

Müller, G.O. : *Basics of Electron-Impact-Excited Luminescence Devices*, Phys. Stat. Sol. (a) (1984)597.

Mach, R. and Müller, G.O. : *Physical Concepts of High-Field, Thin-Film Electroluminescence Devices*, Phys. Stat. Sol. (a)69, (1982)11.

Müller, G.O., *Solid State Luminescence-Theory, Materials and Devices*, edited by A.H. Kitai, Chapman & Hall, pp133

Müller, G.O. , *Solid State Luminescence - Theory, Materials and Device*, Edited by A.H. Kitai, Chapman & Hall, 1993, pp142.

Nelson, R.S. , Thompson, M.W. , Proc. R. Soc. London, 259, (1961)458.

Ohring, Milton : *The Materials Science of Thin Films*, Academic Press , 1992, pp223.

Ouyang, X. , Kitai, A. H. : *Yttrium Silicates Thin Film Color Phosphors by Magnetron Sputtering*, accepted Thin Solid Films, August, 1994.

Ozawa, L. : *Cathodoluminescence-Theory and Application*, Kodansha Ltd., 1990.

Pankove, J.I. , *Optical Processes in Semiconductors*, Dover Publication, Inc. 1971, pp40.

Pohl, U.W. and Gumlich, H.-E. : *Solid State Luminescence*, Edited by A.H. Kitai, ©1993 Chapman & Hall, pp71.

Robbins, D.J. : J. Electrochem. Soc.: Solid-State Science & Tech., (1984)142.

Shmulovich, Joseph and Kocian, Dean F. : *Thin-Film Phosphors for Miniature CRTs used in Helmet-Mounted Displays*, SID'89, p297.

Simonov, M.A. , Sandormirski, P.A. , et al.: *The Crystal Structure of Willemite* Zn_2SiO_4, Soviet Physics-Doklady, 22, (1977)622.

Skoog, Douglas A. : *Principles of Instrumental Analysis*, 3rd Edition, Saunders College Pub., 1985, pp139-140.

Smith, D.H. : *Modeling AC Thin-Film Electroluminescent Devices*. J. Luminescence, 23 (1981)209.

Somekh, R.E. : *The Sputter Deposition of Superconducting Ceramics*, Thin Solid Films, (1989)2571.

Suzuki, H. , et al.: *UV and Gamma-ray Excited Luminescence of Cerium-doped rare earth Oxyorthosilicates*, Nuclear Instr. & Meth. in Phys. Res. A320 (1992)263.

Takamori, Takeshi, et al: *Phase Transformations and Thermoluminescence of Plasma-Sprayed Zinc Silicates Phosphor*, J. Am. Ceram. Soc., (1983)C129.

Tannas, L.E. : *Flat-Panel Displays and CRTs*, Van Nostrand Reinhold Company, 1985, pp257-258.

Tiku, S.K. and Smith, G.C. : *Choice of Dielectrics for TFEL Displays*, IEEE Trans. Electron Devices, 31, (1984)105.

Toropov, N.A. and Bondar, I.A. , Izv. Akad. Nauk SSSR, Otd. Khim. Nauk (1961)544.

Travis, David :" *Effective Color Displays-Theory and Practice*", Edited by B.R. Gaines and A. Monk, Academic Press, 1981.

Van Uitert, L.G. : *Factors Controlling the Intensity of Emission of Eu3+ and Tb3+ in Scheelites*, J. Chem. Phys., 37 (1962)981.

Vossen, J. L. : *Thin Film Process II*, Academic Press, 1991.

Williams, J., Lum., **23**, 1 (1981).

Williamson, J. , et al., Phys. Chem. Glasses, 5[2]52-59 (1964).

Yacobi, B.G., and Holt, D.B.:*Cathodoluminescence Microscopy of Inorganic Solids*, Plenum Press, New York and London, 1990.

Yang, E.S.: *Thermal Release of Trapped Electrons and Phosphorescent Decay in Zinc Silicate Phosphors*, J. Appl. Phys. 52(7), (1981)4753.